~~CONFIDENTIAL~~

C70-1167

NASA CR-72711
GESP-9014

DEVELOPMENT OF LOW THERMAL EXPANSION TUNGSTEN-UO_2 CERMET FUEL

Security Classification change to Unclassified by authority of T.D. 73-51 9-28-72

by

M. O. Marlowe and A. I. Kaznoff

~~RESTRICTED DATA~~

This document contains restricted data as defined in the Atomic Energy Act of 1954. Its transmittal or the disclosure of its contents in any manner to an unauthorized person is prohibited.

~~GROUP 1~~

Excluded from automatic downgrading and declassification

GENERAL ELECTRIC COMPANY

prepared for

NATIONAL AERONAUTICS AND SPACE ADMINISTRATION

NASA Lewis Research Center
Contract NAS 3-10614
John W. R. Creagh, Project Manager

~~CONFIDENTIAL~~

LEGAL NOTICE

Requests for copies of this report should be referred to:

National Aeronautics and Space Administration
Scientific and Technical Information Facility
P. O. Box 33
College Park, Maryland 20740

NASA CR-72711
GESP-9014

TOPICAL REPORT

DEVELOPMENT OF LOW THERMAL EXPANSION TUNGSTEN-UO_2 CERMET FUEL

by

M. O. Marlowe and A. I. Kaznoff

GENERAL ELECTRIC COMPANY
Nuclear Thermionic Power Operation
P. O. Box 846
Pleasanton, California 94566

prepared for

NATIONAL AERONAUTICS AND SPACE ADMINISTRATION

March 31, 1970

CONTRACT NAS 3-10614

NASA Lewis Research Center
Cleveland, Ohio
John W. R. Creagh, Project Manager
Nuclear Systems Division

CONTENTS

	Page
SUMMARY	1
INTRODUCTION	3
MATERIALS	10
FABRICATION OF CERMET BODIES	21
A. Particle Blending	21
B. Hot Pressing	22
C. Heat Treating	25
TESTING APPARATUS AND PROCEDURE	27
A. Apparatus	27
B. Thermal Expansion Testing	27
C. Thermal Cycling Test Conditions	30
EXPERIMENTAL RESULTS	35
A. Structure of As-Fabricated Cermets	35
B. Summary of Experimental Tests and Specimen History	40
C. Thermal Expansion Behavior of Cermets	40
D. Cermet Dimensional Changes During Heat Treatment and Thermal Expansion Measurements	48
E. Thermal Cycling Behavior of Cermets	53
ANALYSIS AND DISCUSSION OF RESULTS	63
A. Thermal Expansion	63
B. Microstructural Changes	67
CONCLUSIONS	80
A. Fabrication of Cermets	80
B. Thermal Expansion	80
C. Thermal Cycling Behavior	81
APPENDIX A - THEORETICAL DENSITY OF CERMETS	82
APPENDIX B - ACCURACY OF PERMANENT DIMENSIONAL CHANGE MEASUREMENTS	86
REFERENCES	88

FIGURES

Figure		Page
1	Difference in Volumetric Thermal Expansion of Tungsten and UO_2	6
2	20 μm Particles As-Received	12
3	20 μm Particles As-Received	12
4	200 μm Particles As-Received	13
5	200 μm Particles As-Received	13
6	Cross-Section of 200 μm Particles As-Received	14
7	Cross-Section of 20 μm Particles As-Received	14
8	20 μm Particles After Vacuum Heat Treatment at 1800°C for 24 Hours	16
9	Fracture Surface of Tungsten Shell on 200 μm Particle After Vacuum Heat Treatment at 1800°C for 24 Hours	16
10	Cross-Section of Vacuum Heat Treated Particles	17
11	Fracture Surface of Vacuum Heat Treated Particles	17
12	20 μm Particles After 20 Thermal Cycles	18
13	Cross-Section of 20 μm Particles After 20 Thermal Cycles	18
14	Cross-Section of 200 μm Particles After 20 Thermal Cycles	19
15	Grain Boundary Bubbles (or Pores) in UO_2 in 200 μm Particles After 20 Thermal Cycles	19
16	Hot Pressing Die Loading Apparatus	23
17	Flow Diagram for Die Loading Procedure	24
18	Effect of Pressure on Density of Hot Pressed Cermets	26
19	Induction Heated Thermal Expansion and Thermal Cycle Testing Dilatometer	28

Figure		Page
20	Schematic Drawing of Thermal Expansion and Cycling Apparatus	29
21	Typical Thermal Expansion Test Results	31
22	Thermal Cycle Test Conditions	33
23	Longitudinal Cross-Section of As-Hot Pressed High Density Cermet	36
24	As-Hot Pressed High Density Cermet	37
25	As-Hot Pressed High Density Cermet	37
26	As-Hot Pressed Low Density Cermet	38
27	As-Hot Pressed Low Density Cermet	38
28	Fracture Surface of Low Density Hot Pressed Cermet	39
29	Fracture Surface of Low Density Hot Pressed Cermet	39
30	Thermal Expansion of As-Fabricated High Density Cermet	43
31	Thermal Expansion of Heat Treated High Density Cermets	45
32	Thermal Expansion of As-Fabricated Low Density Cermets	46
33	Thermal Expansion of Heat Treated Low Density Cermets	47
34	Effect of Heat Treatment for 24 Hours on Cermet Thermal Expansion at 1600°C	49
35	High Density Cermet After Thermal Expansion Testing	52
36	High Density Cermet After Thermal Expansion Results	52
37	High Density Cermet Heat Treated at 1700°C for 24 Hours	54
38	High Density Cermet Heat Treated at 1800°C for 24 Hours	54
39	High Density Cermet Heat Treated at 1900°C for 24 Hours	55

Figure		Page
40	High Density Cermet Heat Treated at 1700°C for 24 Hours	55
41	High Density Cermet Heat Treated at 1800°C for 24 Hours	56
42	Diametral Growth of Cermets on Thermal Cycling	57
43	Axial Growth of Cermets on Thermal Cycling	58
44	High Density Cermet After 50 Thermal Cycles	59
45	Fracture Surface of High Density Cermet After 50 Thermal Cycles	59
46	Fracture Surface of High Density Cermet After 50 Thermal Cycles	61
47	Fracture Surface of Low Density Cermet After 50 Thermal Cycles	61
48	Fracture Surface of Low Density Cermet After 50 Thermal Cycles	62
49	Low Density Cermet After 50 Thermal Cycles	62
50	Comparison of Calculated and Observed Cermet Thermal Expansion	64
51	Model for Calculation of Grain Boundary Bubble Swelling and Gas Concentration of Tungsten Matrix	68
52	Grain Boundary Gas Bubble Size Distribution	72

ABSTRACT

An attempt was made to develop a tungsten-uranium dioxide cermet of high fuel loading with thermal expansion approaching that of tungsten and with good dimensional stability on thermal cycling. These goals were sought through the use of tungsten-coated uranium dioxide particles with sufficient locally available void volume to accommodate the difference in thermal expansion between the uranium dioxide and the tungsten matrix and through limitation of plastic deformation in the particles during fabrication to avoid mechanical keying of the particles and the matrix.

The particles were vibratorily compacted prior to hot pressing. The thermal expansion of the cermets was determined and they were thermal cycle tested. The thermal expansion of the cermets was considerably closer to that of tungsten than was observed with previously reported specimens of similar composition. However, the thermal cycling of the cermets resulted in intolerable growth. This growth could be accounted for by the agglomeration of gases trapped in the uranium dioxide particles during deposition of the tungsten coating.

SUMMARY

This topical report was prepared under NASA Contract NAS 3-10614, and was directed toward the development of UO_2-W cermet fuel for nuclear thermionic emitters.

Tungsten-coated, porous UO_2 spheres nominally 20 and 200 μm in diameter were vibratorily compacted to approximately 80% packing density in graphite hot-pressing dies. The particles were compacted to 90 and 95% of theoretical density by hot pressing at 1700°C and 4000 and 6000 psi. The fuel loading was 53 volume percent UO_2 for fully dense cermets.

The linear thermal expansion of the cermets was found to be described by the relations:

(a) for the 95% dense cermets,

$$\frac{\%\Delta L}{L} = (3.424 \pm 0.291) \times 10^{-4} (T-25) + (1.865 \pm 0.139) \times 10^{-7} (T-25)^2;$$

(b) for the 90% dense cermets,

$$\frac{\%\Delta L}{L} = (4.227 \pm 0.301) \times 10^{-4} (T-25) + (1.313 \pm 0.282) \times 10^{-7} (T-25)^2;$$

where the tolerance limits are for the 90% confidence interval for the mean expansion of the as-fabricated cermets. The thermal expansion was considerably below previous cermets of a similar composition, indicating that mechanical decoupling of the fuel particle from the tungsten matrix was achieved. Heat treatment for 24 hours at 1700 to 2000°C did not detectably alter the thermal expansion based on the limited number of specimens tested.

The cermets were thermal cycled for 50 thermal cycles from 150 to 1600°C. The cermets grew monotonically and isotropically at rates in the range of 0.30 to 0.39 mils per inch per cycle.

The dimensional changes of the cermets could be accounted for by the agglomeration of gases trapped in the porous fuel particles during the thermochemical deposition of the tungsten coating.

INTRODUCTION

Thermionic devices for direct conversion of thermal energy produced by nuclear reaction to electrical energy require high surface temperatures for the thermionic emitter. Because of the low thermal conductivity of uranium dioxide (UO_2), this results in very high central temperatures for oxide fueled thermionic devices which require fission gas venting. Dilution of the oxide fuel with a refractory metal allows a considerable increase in the thermal conductivity of the fuel-body and the possibility of complete fission product retention. The high thermal conductivity of tungsten coupled with its compatibility with UO_2, its low vapor pressure, fabricability, and high temperature mechanical properties, make it a superior choice for the metal phase of the two-phase (cermet) fuel body.[1]

Five basic techniques have been used for fabrication of refractory metal-UO_2 cermet bodies.[2, 3, 4] These include the following.

(1) Sintering, with or without pressure, mixtures of blended powders of the oxide and refractory metal components.

(2) Sintering, with or without pressure, of oxide particles previously coated with powdered refractory metal with organic additives to the refractory metal to promote coating of the fuel particles.

(3) Sintering, with or without pressure, of oxide particles coated by thermochemical deposition of the refractory metal.

(4) Pressure sintering of mixtures of oxide powder and refractory metal wires or fibers.

(5) Unidirection solidification from the melt of refractory metal-UO_2 mixtures with the resultant formation of aligned metal fibers in the oxide matrix.

Unfortunately, there is a large difference in the thermal expansion behavior of UO_2 and the refractory metals, particularly tungsten (the linear thermal expansion of UO_2 varies from 1.8 to 2.4 times that of tungsten over the temperature range of 100 to 2400°C).[5, 6] The mechanical interaction due to the difference in expansion of the two phases leads to dimensional instability of the cermet body on thermal cycling,[1, 7, 8] which is a more or less inherent feature of nuclear test reactor operation as accompanying changes in power level, reactor scrams and shutdown and restart. As much as 12% increase in volume after 100 thermal cycles from 250 to 2150°C for 60 volume percent UO_2-W cermets fabricated by hot isostatic pressing of vapor-deposited, tungsten-coated UO_2 particles has been reported.[7] The number of power cycles to be experienced in a practical reactor system is not known precisely, but is certainly much smaller than those enountered in test reactors. In addition, the resultant expansion of the composite UO_2-W cermet bodies that have been made has been considerably in excess of that of tungsten, which is a likely candidate material for the cladding material for the cermet nuclear fuel.[1] Thus, tungsten-clad UO_2-W bodies have shown failure of the cladding after a very few thermal cycles to elevated temperatures.[1, 9, 10]

High density UO_2-W cermets with approximately 60 and 80 volume percent fuel loadings fabricated by vacuum hot pressing approximately 100 micrometer diameter thermochemically tungsten-coated UO_2 particles showed complex dimensional changes on thermal cycling.[1] Total linear dimensional changes were less than 2 percent after 100 cycles from 150 and 1070 to 1600°C, but growth occurred in some instances and shrinkage in others; and occasionally the dimensional changes were of opposite sign in the diametral and axial directions. The microstructure of the thermally cycled cermets showed severe breakup of the continuous tungsten matrix and penetration of nearly

every tungsten grain boundary with UO_2, though the UO_2 was sufficiently near the stoichiometric composition to essentially rule out oxidation of the tungsten and tungsten transport in the UO_2 as the mechanism of degradation of the structure.[1] Mechanical interaction of the tungsten matrix and the particles induced by the thermal expansion difference and sintering of the fuel particles were believed to be the source of the dimensional changes.

It is the consensus[1, 8] that the chief problem in the development of dimensionally and structurally stable tungsten-UO_2 cermets is the difference in the thermal expansion of the refractory metal and the oxide. Based on this conclusion, a rationale for a dimensionally stable tungsten-UO_2 cermet structure to overcome the thermal expansion induced difficulties previously encountered with coated fuel particle cermets[2, 3] was devised. That rationale was that the mechanical interaction of the fuel particles and the continuous tungsten matrix could be avoided if sufficient void volume was incorporated to accommodate the excess thermal expansion of the UO_2 over that of the tungsten. (Note that this presupposes either that the void volume is distributed around the fuel particle; i. e., in the so called "pea-in-a-pod" concept, or that the UO_2 is sufficiently plastic at the temperature of interaction of the refractory metal and the oxide that it can flow into its own voidage). Furthermore, the thermal expansion of the cermet will be equal to that of the tungsten, thus, eliminating the problems resulting from the mismatch in expansion of the cermet body and its tungsten cladding.

The void volume required for accommodation of the excess thermal expansion of the UO_2 over that of tungsten is given by the difference in the volumetric expansion of the two components which is shown as a function of temperature[5, 6] in Figure 1. Note, for example,

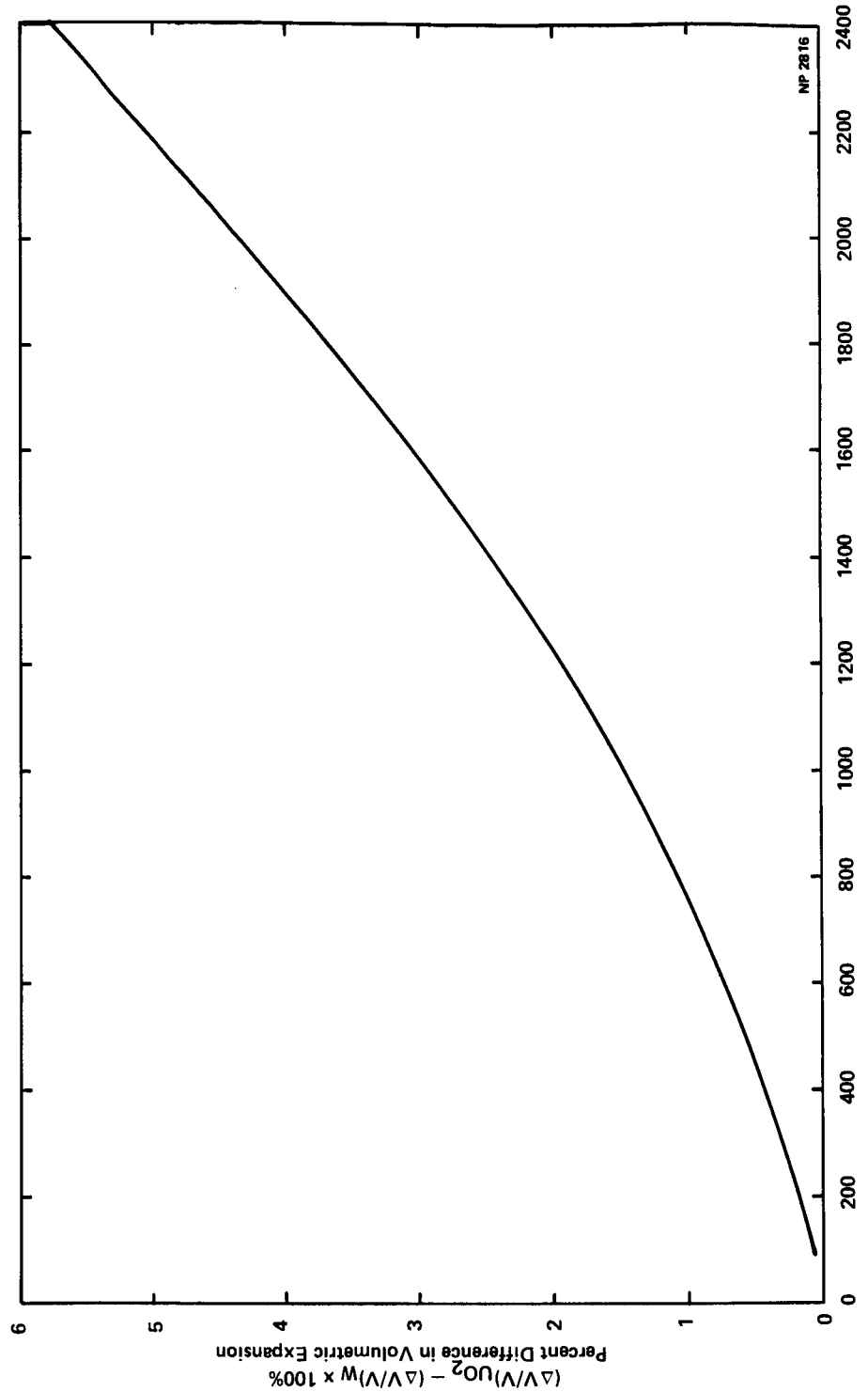

FIGURE 1. DIFFERENCE IN VOLUMETRIC THERMAL EXPANSION OF TUNGSTEN AND UO_2

that for a body designed to operate at a maximum temperature of 1700°C, 3.3 percent accommodation void volume inside each tungsten shell is required. Previous tungsten-UO_2 cermets made from coated particles[1, 8] have been made with as little as 2 percent porosity inside the tungsten shell, obviously insufficient to accommodate the thermal expansion mismatch, even if the UO_2 were plastic enough to flow into the voids. Thus, if the desired cermet structure is to be achieved, greater retention of porosity inside the tungsten shell is required.

The shape of the fuel particles can also influence the resultant stability of the cermet body on thermal treatment. If the fuel particles were perfect spheres, inside perfectly spherical shells of tungsten, no mechanical interaction would be expected if sufficient peripheral void volume were available to accommodate the excess thermal expansion of the UO_2. However, non-spherical particles are likely to produce mechanical interaction through reorientation of the fuel particles in their shells during thermal cycling. Thus, improvements in sphericity of the fuel particles should improve the performance of the cermet body. Both isostatic[8] and unidirectional[1, 2] hot-pressing of high fuel loading tungsten-UO_2 cermets produced by the coated particle technique with essentially monodisperse particles results in severe deviation of the fuel particles from sphericity, as a result of plastic deformation of the particles during fabrication. This plastic deformation is required because of the low packing density of the particles when loaded into the hot-pressing die or capsule and the conscious attempt to obtain high density bodies. For example, the maximum theoretical packing density of monodisperse (single-size) particles is only 74 percent,[12] with actual random packing of spherical particles more closely approaching a packing density of 60 to 63 percent.[13] Thus, elimination of porosity between the tungsten shells of such an assemblage requires a volume decrease of 37 to 40 percent, resulting in an equivalent amount of total volumetric plastic strain in the particles.

The obvious approach to achieve a closer approach to sphericity in the fuel particles after fabrication through a decrease in the required deformation of the particles is to increase the packing density prior to application of temperature and pressure. This can be achieved by resorting to other than monodisperse particles. For a two-component mixture of particles, the maximum packing density increases with the ratio of sizes of the particles. Essentially no increase is achieved for size ratios greater than 100/1 and for particles that individually pack randomly to a density of 60 percent, a size ratio of 10/1 accomplishes two-thirds of the maximum possible packing density increase.[12] In addition, when considering fabrication of coated particles for fabrication of cermets, the possible range of particle sizes that can be thermochemically coated is about 10/1. With such a mixture of particle sizes, a packing density of 83% is possible.[14]

If such a packing density is achieved prior to hot-pressing, elimination of the interparticle porosity will require a volumetric plastic deformation of the tungsten shells of only 17 percent. Thus, if the starting fuel particles contain in excess of that amount (17 percent) of porosity prior to hot pressing, the excess porosity should be retained within the tungsten shells, and will be available for accommodation of the excess thermal expansion of the UO_2 over that of tungsten. If the operation of the cermet body is to be at 1700°C, for example, 3.3 percent void volume for accommodation of the excess thermal expansion is required. The total of 20.3 percent (17% + 3.3%) void volume in the original fuel particles is needed to achieve this objective.

It is likely that, after hot pressing of the tungsten-coated porous UO_2 particles, some of the remaining void volume in the tungsten shells will be distributed throughout the UO_2 particles rather than located peripherally around the particles. Redistribution of this porosity to the fuel particle-tungsten shell gap by sintering of the fuel may be

possible by heat treating of the hot-pressed cermet body. Sintering should cause the temperature at which contact is made between the two components to increase from somewhat below to above the hot pressing temperature.

Based on the above considerations, a route to the desired tungsten-UO_2 cermet structure with dimensional and structural stability and with a thermal expansion approaching that of tungsten is as follows:

(A) Coat two sizes of (size ratio 10/1) high porosity (>20 percent) UO_2 particles.

(B) Pack a mixture of the two particles to high packing density (80 percent) in a hot pressing die or capsule.

(C) Hot press the body to a final density of 95 percent of theoretical, eliminating interparticle porosity in the metal matrix, but retaining 3 to 5 percent porosity in the fuel particles.

(D) Heat treat the hot-pressed cermet body to effect a redistribution of the UO_2 porosity to the tungsten shell-fuel particle gap.

It is the purpose of this report to describe an experimental program to fabricate tungsten-UO_2 cermets by the technique described above and to report the resulting thermal expansion achieved by such a cermet body and its behavior on thermal cycling.

For minimization of variables in comparison with previous experience[1] on tungsten-UO_2 cermets formed from monodisperse, spherical, coated particles, a unidirectional hot-pressing technique was chosen for the densification process.

It should be pointed out that for high initial packing density bodies, the unidirectional hot-pressing technique closely approximates isostatic hot pressing conditions, because of the decrease in ram travel and consequent decrease in wall friction and densification gradients.

MATERIALS

The Nuclear Materials and Equipment Corporation in Apollo, Pennsylvania, fabricated 20 and 200 μm diameter spherical UO_2 particles containing 30 ± 5% porosity, using a proprietary process. The particles were coated with tungsten by hydrogen reduction of WCl_6 in a fluid bed reactor. Sufficient tungsten coating was applied to the particles to give a composition of 53 volume percent UO_2 in the coated particles. The results of chemical analyses of the coated particles are listed in Table 1.

Scanning electron micrographs of the particles are shown in Figures 2 through 5. Note the considerable variation in size of the nominally 20 micrometer coated particles and considerable deviation from sphericity. The variation in size of the nominally 200 micrometer diameter particles is not as marked nor is the apparent deviation from sphericity.

The actual average diameters of the nominally 20 and 200 micrometer coated particles were 21.7 ± 8.2*micrometers and 250.0 ± 25.7* micrometers as determined microscopically. The densities of the uncoated UO_2 substrate particles were 73.5 and 74.6 percent of theoretical (10.96 gm/cm^3) for the 20 and 200 micrometer particles, respectively, by the vendor's analyses.

The extensive retained porosity in the coated 200 micrometer particles was uniformly distributed in the UO_2 as shown in Figure 6, with no noticeable penetration of the tungsten into the porosity. The porosity in the smaller (20 micrometer) particles is agglomerated toward the center of the particles as shown in Figure 7, often with only a central pore remaining. Note also the apparent nonuniformity of the coating thickness and some penetration of tungsten into the particle porosity in the smaller particles.

*Average Feret's diameter ± 1 standard deviation.

Table 1. CHEMICAL CHARACTERIZATION OF TUNGSTEN COATED UO_2 PARTICLES+

Element	200 μm Coated Particles (ppm)	20 μm Coated Particles (ppm)	Element	200 μm Coated Particles (ppm)	20 μm Coated Particles (ppm)
Ag	<0.1	<0.1	Li	<1	<1
Al	4	24	Mg	<1	6
B	1.2	1.0	Mn	<1	6
C	30 ± 5	7 ± 5	Mo	<3	<3
Ca	30	10	Na	<15	<15
Cd	<0.5	<0.5	Nb	<100	<10
Cl	55*	48*	Ni	40	36
Co	<2	<2	Pb	<1	6
Cr	48	<3	Si	6	<6
Cu	<1	<1	Sm	<1	<0.5
Dy	<1	<0.5	Sn	<1	<1
Eu	<0.1	<0.1	Ti	<10	5
F	15*	18*	U	34.12 wt%	34.01 wt%
Fe	<14	<14	V	<11	40
Gd	<0.5	<0.2	W	61.37 wt%	61.41 wt%
			Zr	<100	<5

+ The O/U ratio of the as-received particles was not determined because of sampling difficulties. The O/U ratio of as-hot pressed pellets made from these particles was 1.999 ± 0.009 as determined from the lattice parameter of the UO_2.

* Average of four analyses as follows:

Source of Analysis	Particle Size (μm)	Chlorine Content (ppm)	Fluorine Content (ppm)
NUMEC	200	51	<10
Apollo, Pennsylvania	20	50	<10
General Electric Company	200	41 ± 17	≤5
Pleasanton, California	20	36 ± 15	6 ± 5
General Electric Company	200	58	7
San Jose, California	20	67	16
AEC (New Brunswick Lab)	200	70	37
New Brunswick, N. J.	20	40	40

Figure 2. 20 μm Particles as Received

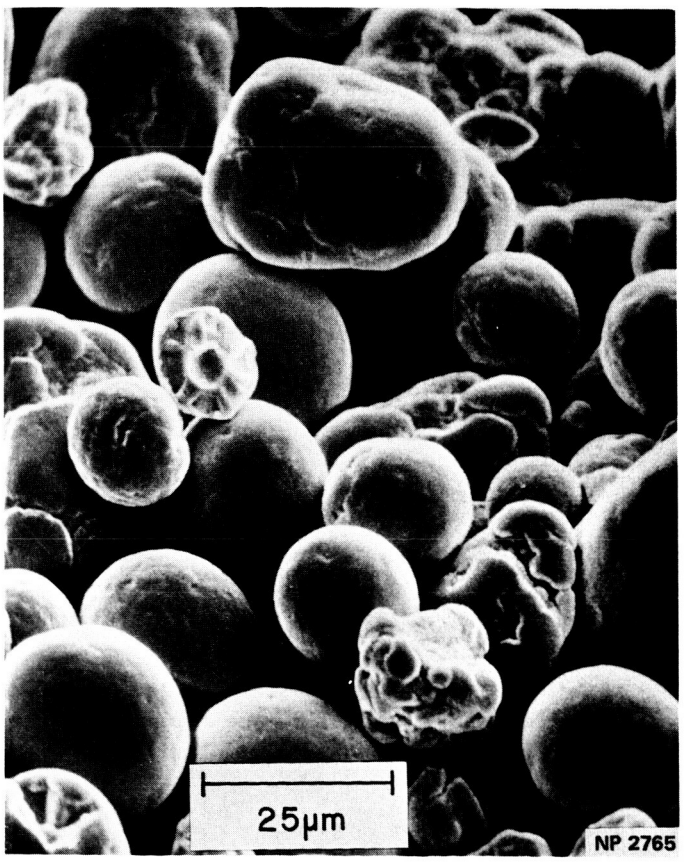

Figure 3. 20 μm Particles As Received

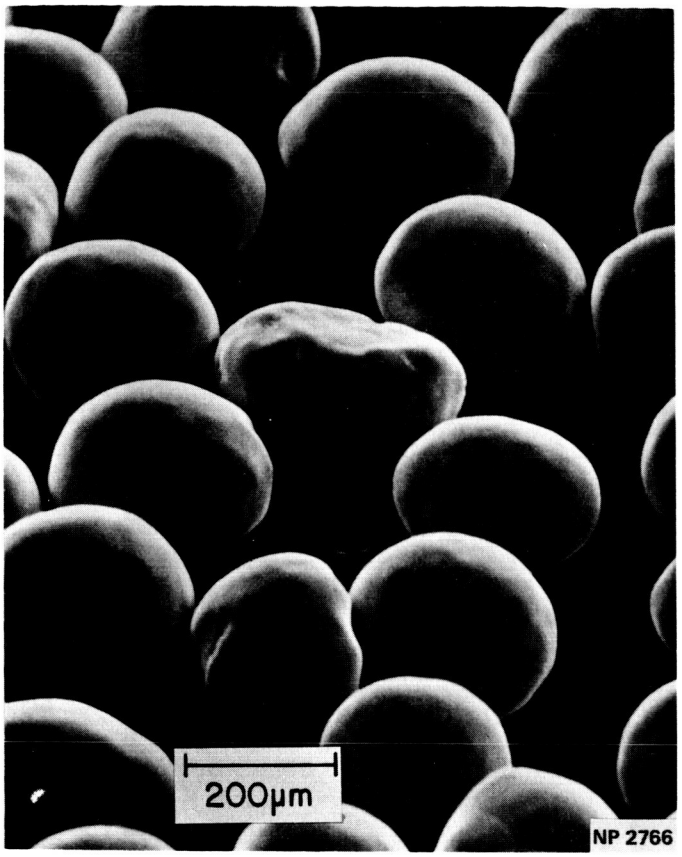

Figure 4. 200 μm Particles as Received

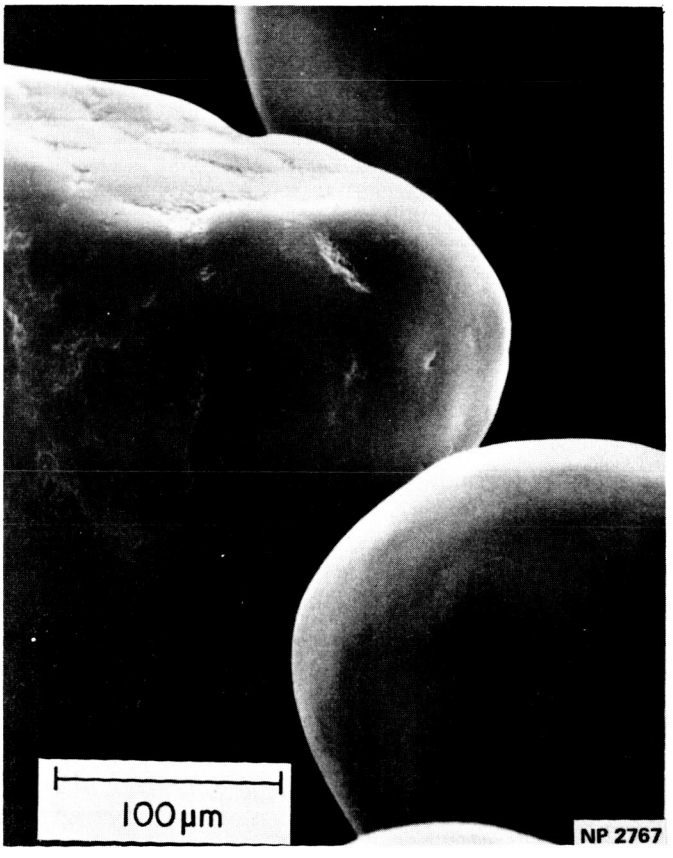

Figure 5. 200 μm Particles as Received

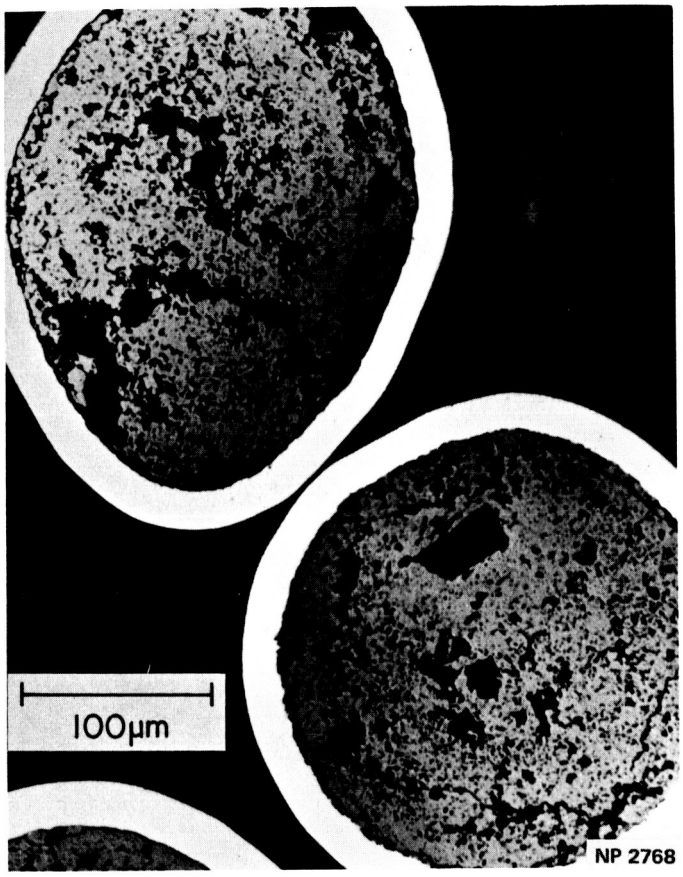

Figure 6. Cross-section of 200 μm Particles as Received

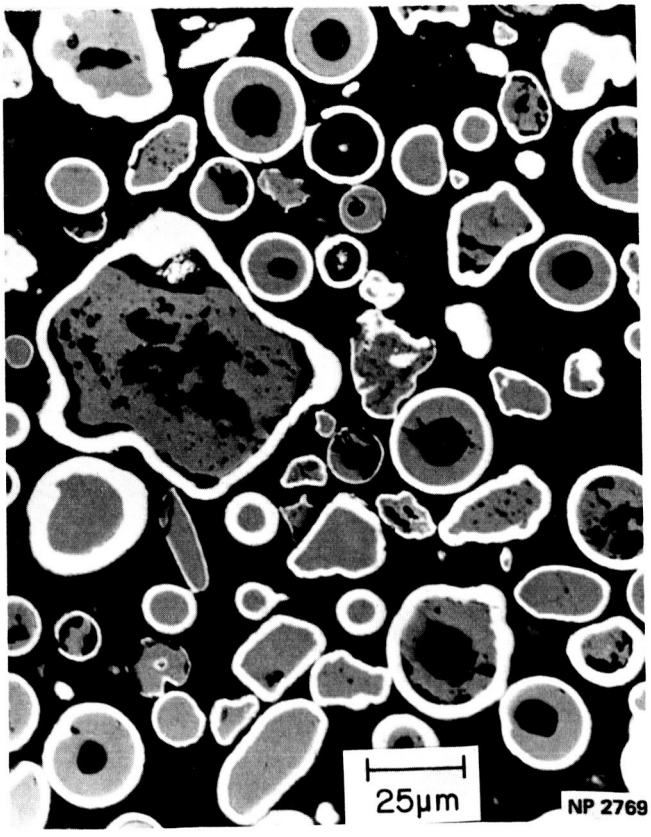

Figure 7. Cross-section of 20 μm Particles as Received

The effects of thermal treatment on the as-received particles were investigated. Isothermal heat treatment at 1800°C for 24 hours in vacuum led to thermal etching of the tungsten grain boundaries as shown in Figure 8. Some precipitation of gas bubbles, apparently due to halide impurities in the tungsten resulting from the coating process, is evident on the tungsten grain boundaries as shown in a scanning electron micrograph of the fracture surface (Figure 9) of a 200 micrometer particle shell. The UO_2 was densified often with the formation of a few dense grains in the case of the 200 micrometer particles as shown in Figures 10 and 11. The densification of the UO_2 in the larger particles led to release of the UO_2 on sectioning once the shell was cut at the midplane, indicating that the "pea-in-a-pod" concept of the UO_2 particles in the tungsten shell could, indeed, be achieved. Note, also, the sintering together of the tungsten shells in Figures 8 through 11. Heat treatment at 2000°C for 16 hours produced approximately the same microstructural changes in the UO_2 and tungsten.

The response of the particles to thermal cycling was explored by exposing them to 20 cycles from 150 to 1600°C (total time at 1600°C was 10 hours) in an argon atmosphere. The details of the thermal cycle will be discussed later. This treatment, Figure 12, resulted in exaggerated thermal etching of the tungsten grain boundaries compared to the 1800°C for 24 hours heat treatment, as well as sintering together of the particles. There also appears to be considerable breakup of the coatings on the small particles as shown in Figure 12 and in metallographically prepared cross sections of the particles (Figure 13). Densification of the UO_2 was again extensive, with the formation of several dense grains in the larger particles (Figure 14) with partial or total separation of the grain boundaries of the UO_2 (Figure 15). This may be the result of gases trapped in the porous UO_2 at the time of deposition of the tungsten coating.

Both the 20 micrometer and 200 micrometer coated particles were heated in a tungsten Knudsen cell and the gases emitted were

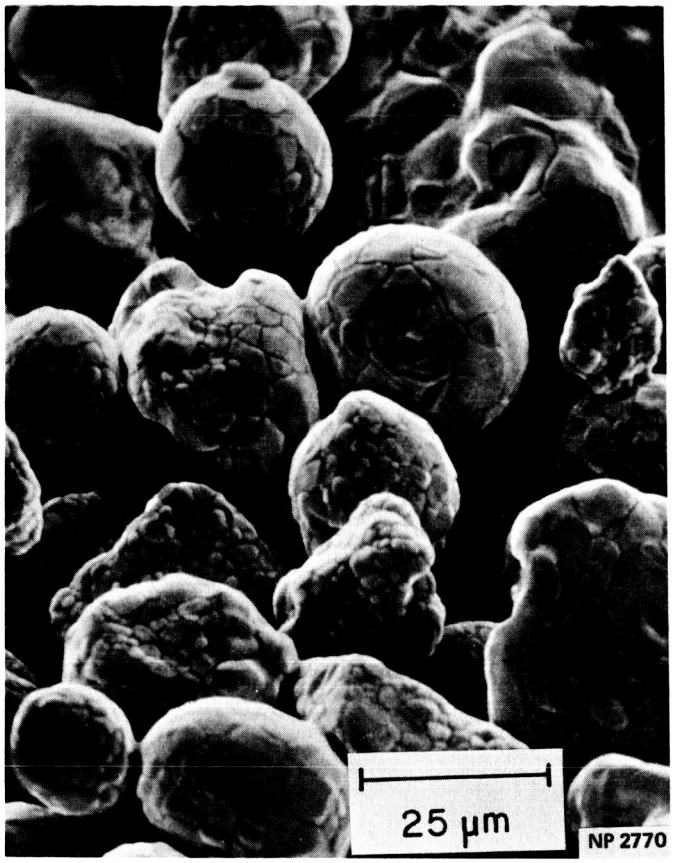

Figure 8. 20 μm Particles After Vacuum Heat Treatment at 1800°C for 24 Hours (Note 200 μm Particle at Upper Right)

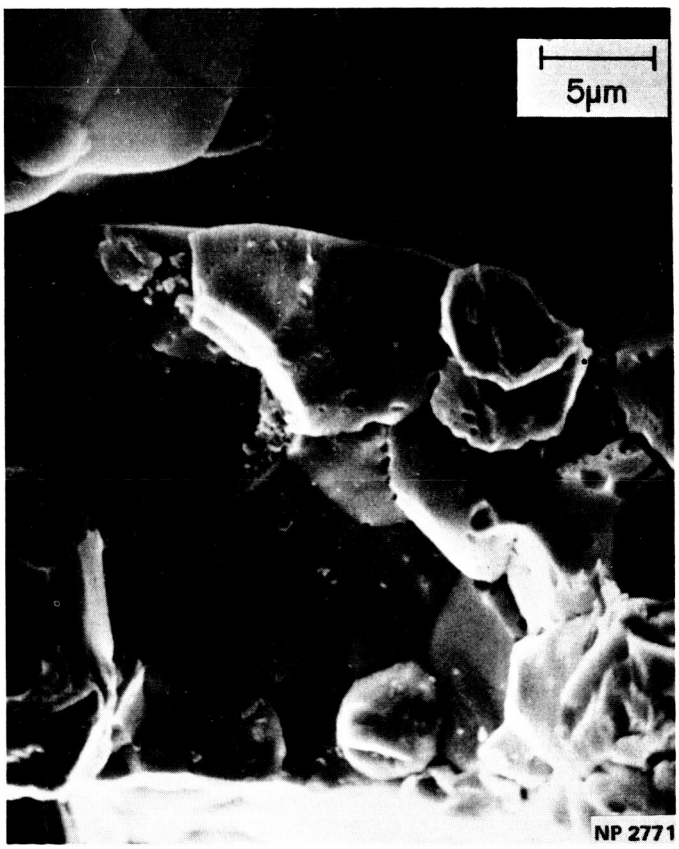

Figure 9. Fracture Surface of Tungsten Shell on 200 μm Particle After Vacuum Heat Treatment at 1800°C for 24 Hours (Note Bubbles on Tungsten Grain Boundaries)

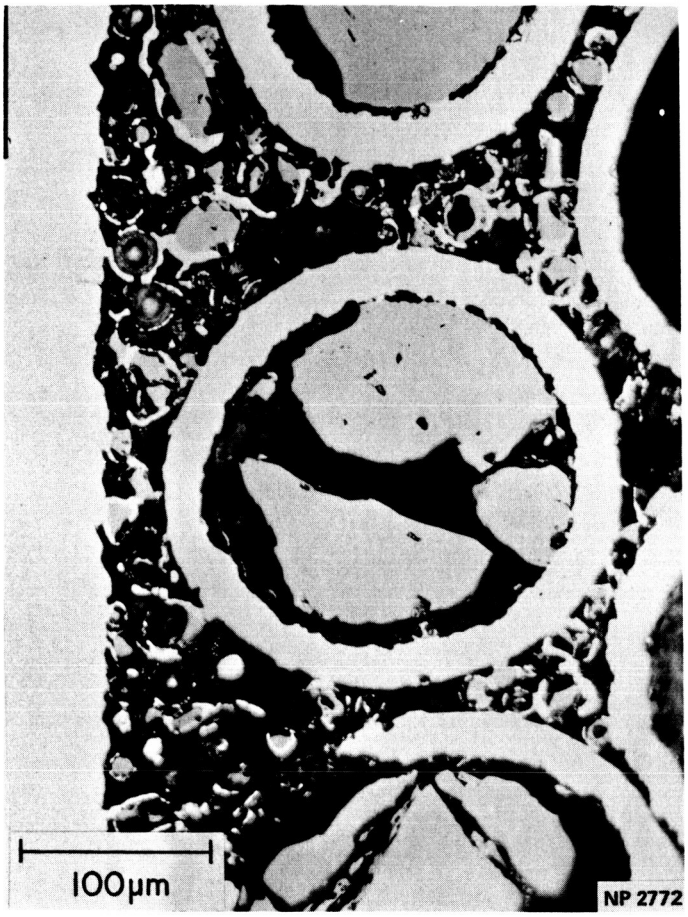

Figure 10. Cross-section of Vacuum Heat Treated Particles (24 Hours at 1800°C)—Note Densification of UO_2 and Large Grains in the 200 μm Particles

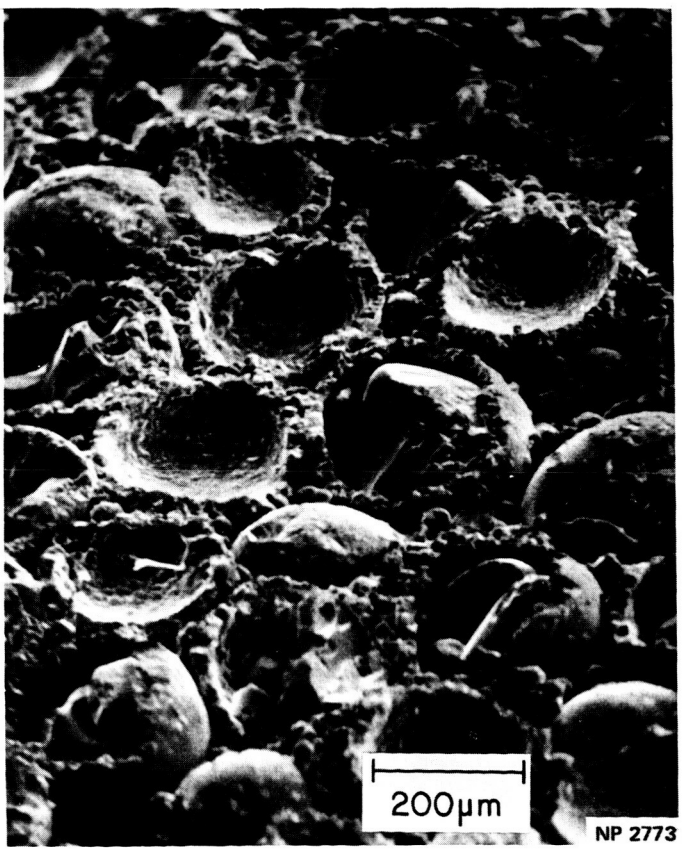

Figure 11. Fracture Surface of Vacuum Heat Treated Particles (24 Hours at 1800°C)—Note Dense UO_2 Grains in 200 μm Particles

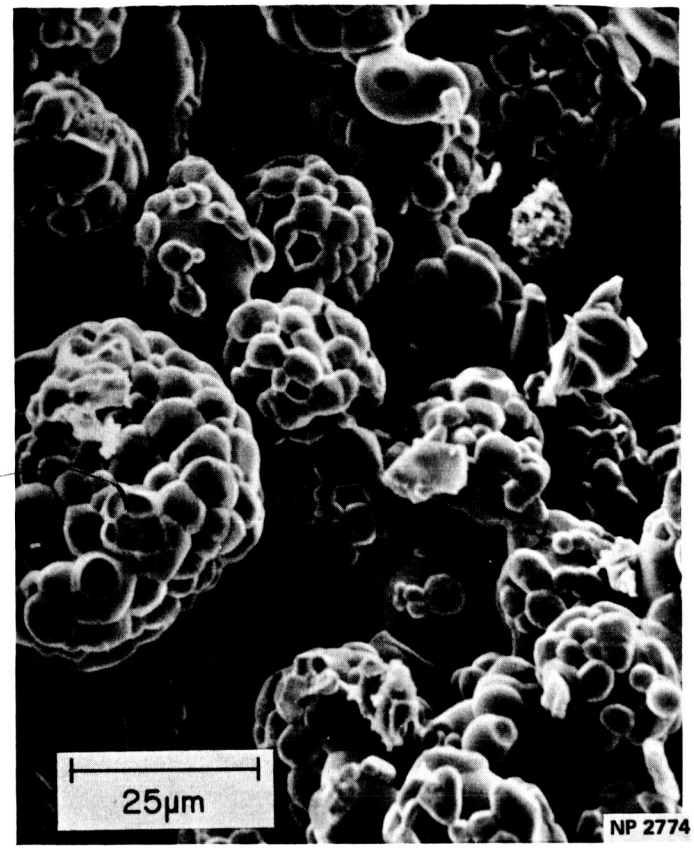

Figure 12. 20 μm Particles After 20 Thermal Cycles (150°C to 1600°C)

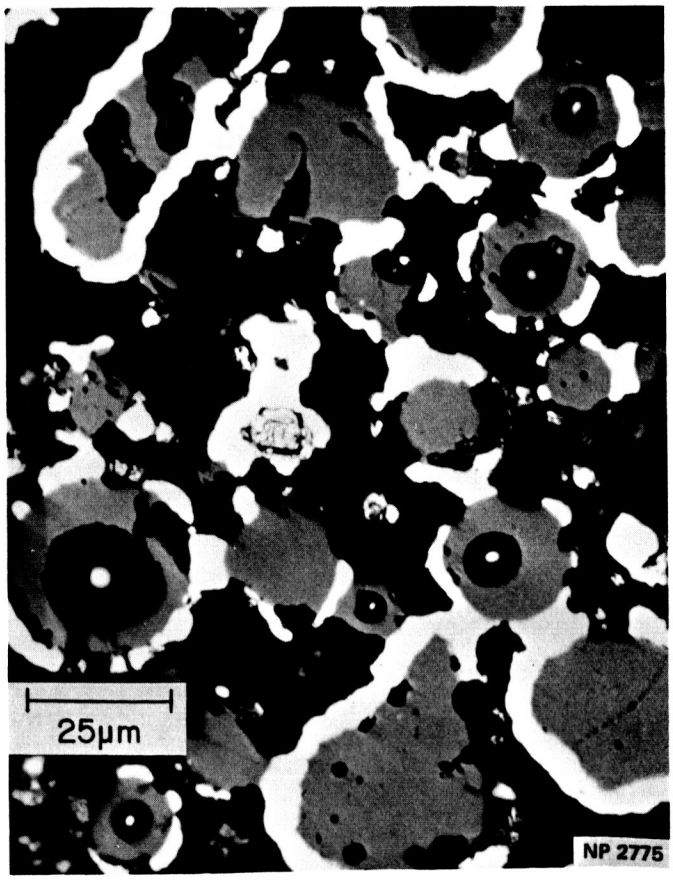

Figure 13. Cross-section of 20 μm Particles After 20 Thermal Cycles (150°C to 1600°C)

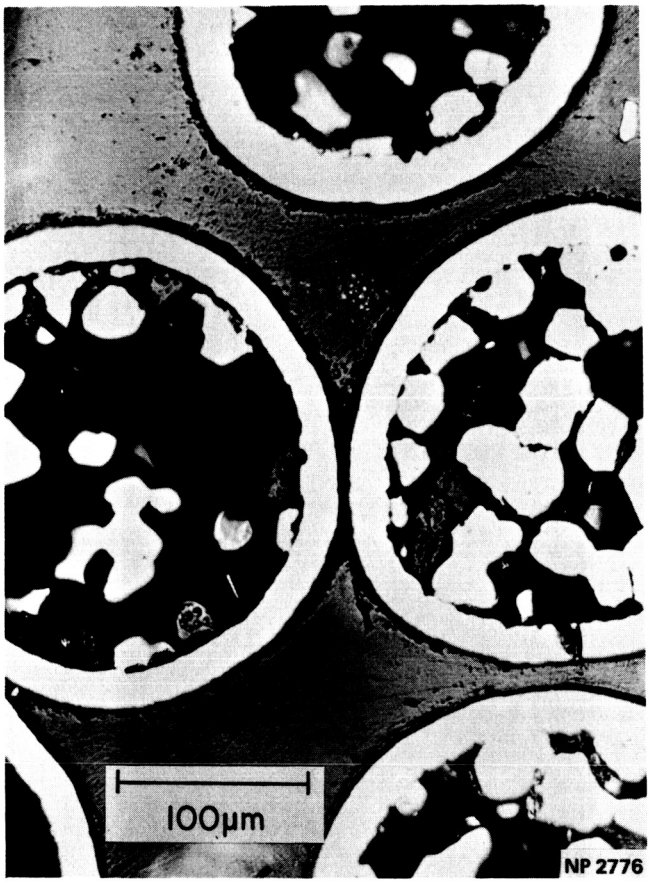

Figure 14. Cross-section of 200 μm Particles After 20 Thermal Cycles (150°C to 1600°C)—Note Large, Dense UO_2 Grains and Grain Boundary Pores

Figure 15. Grain Boundary Bubbles (or Pores) in UO_2 in 200 μm Particles After 20 Thermal Cycles (150°C to 1600°C)

analyzed by time-of-flight mass spectrometry. Analysis of the 200 micrometer particles indicated a briefly observed peak corresponding to release of atomic chlorine at 1450°C, lasting only a few minutes. Above 1500°C, the vapor species emitted by the specimens were identical to those emitted by UO_2. No F, HF, HCl, W or U fluorides or chlorides were observed at any temperature to 2038°C. Analysis of the 20 micrometer particles indicated emission of what was interpreted as a mixture of tungsten halides (mainly chlorides) from compositions in the range WCl_4 to WCl_6 above approximately 1200°C. The intensity of emission increased with temperature depleting with time under isothermal conditions.

It is possible that, because of the smaller surface-to-volume ratio of the large particles, the tungsten halides observed in the case of the small particles were below the detection limit for the mass spectrometer when analyzing the very small sample of large particles. The results do indicate that it is possible to remove some of the trapped halides from the coated particles by heat treatment above 1200°C. The efficacy of such a treatment for removal of the halides was not determined.

The chemical specifications reflect the state-of-the-art in fabrication at the initiation of the work. There was a conscious attempt to decrease fluoride content at or below 10 ppm. In retrospect, the ability to specify chloride content was not obtainable at that time. The problem was severely compounded by the precision and accuracy of analytical methods to establish the total and individual halide levels as indicated in Table 1.

FABRICATION OF CERMET BODIES

A. PARTICLE BLENDING

Attempts were made to achieve a high packing density and uniform distribution of the nominally 20 and 200 micrometer coated particles by rolling them in a graphite hot pressing die prior to application of temperature and pressure. Varying degrees of success were achieved but a uniform distribution of the two types of particles throughout a cermet pellet with dimensions of approximately 1/2-inch diameter and 1-inch long after densification was not obtained.

The particle blending technique of Ayer and Soppet[14] was used to obtain the desired high packing density and uniform distribution of particles throughout the cermet pellet. By this technique, the larger particles were loaded into a graphite hot pressing die and were vibrated to minimum volume. During this process a slight load was applied to the column of particles with a screen-ended thimble, the mesh size of the screen being too small to pass the large particles, but large enough to readily pass the small particles (80 mesh -- 117 micrometer opening). The screen-ended thimble was then locked into position with respect to the bottom plunger of the graphite die to restrain the large particles at their minimum packing volume. The small particles were then vibrated through the restraining screen and penetrated throughout the interstices of the larger particles.

Ayer and Soppet observed experimentally that for a system of single-sized spherical particles in a die in which the die cavity is greater than 10 times the diameter of the largest particle, the maximum packing density, P_d, where P_d is the percentage of available void volume occupied by the particles, is given by the relation:

$$P_d = [0.867 - 0.269 \exp (0.201\, d_1/d_2)]\, 100\%, \qquad (1)$$

where d_1 and d_2 are the diameters of the larger and smaller particles, respectively. For the case of the coated particles with a diameter ratio of approximately 10/1, this relation gives a maximum packing density of 83.1 percent. The relations of Ayer and Soppet also show that the composition of the particle mixture to achieve this maximum density is 23.6 percent small particles and 76.4 percent large particles by weight. Some deviation from the maximum packing density is to be expected for the coated particles because of deviations of the particles from sphericity and because of the distribution of particle sizes, albeit narrow.. Measured packing densities for such blends of the coated particles were in the range of 81 to 84 percent.

The apparatus for loading the dies is shown in Figure 16 and a schematic diagram and outline of the die loading procedure is given in Figure 17. The vibrator used was a simple engraving tool with the vibration amplitude adjusted to give a maximum flow rate of the small particles through the interstices of the larger particles. To avoid continuing damage to the dummy stainless steel die plunger (described in Figure 16), the normal engraving tool was replaced by a blunt shaft.

B. HOT PRESSING

The coated particles were loaded by the process described above into graphite (GRAPH-I-TITE "G", Carborundum Company, Sanborn, New York) double-acting hot pressing dies. The graphite plungers were machined from the same material. The die cavity was 0.50-inch in diameter and the total particle charge was 44 grams. Cermet specimens were densified by heating in vacuum (5×10^{-4} torr) at approximately 95°C per minute to 1700°C, then rapidly applying pressure to the desired level on the specimen, and holding under those conditions for 10 minutes. The pressure was then removed and the cermet cooled to room temperature at a cooling rate of

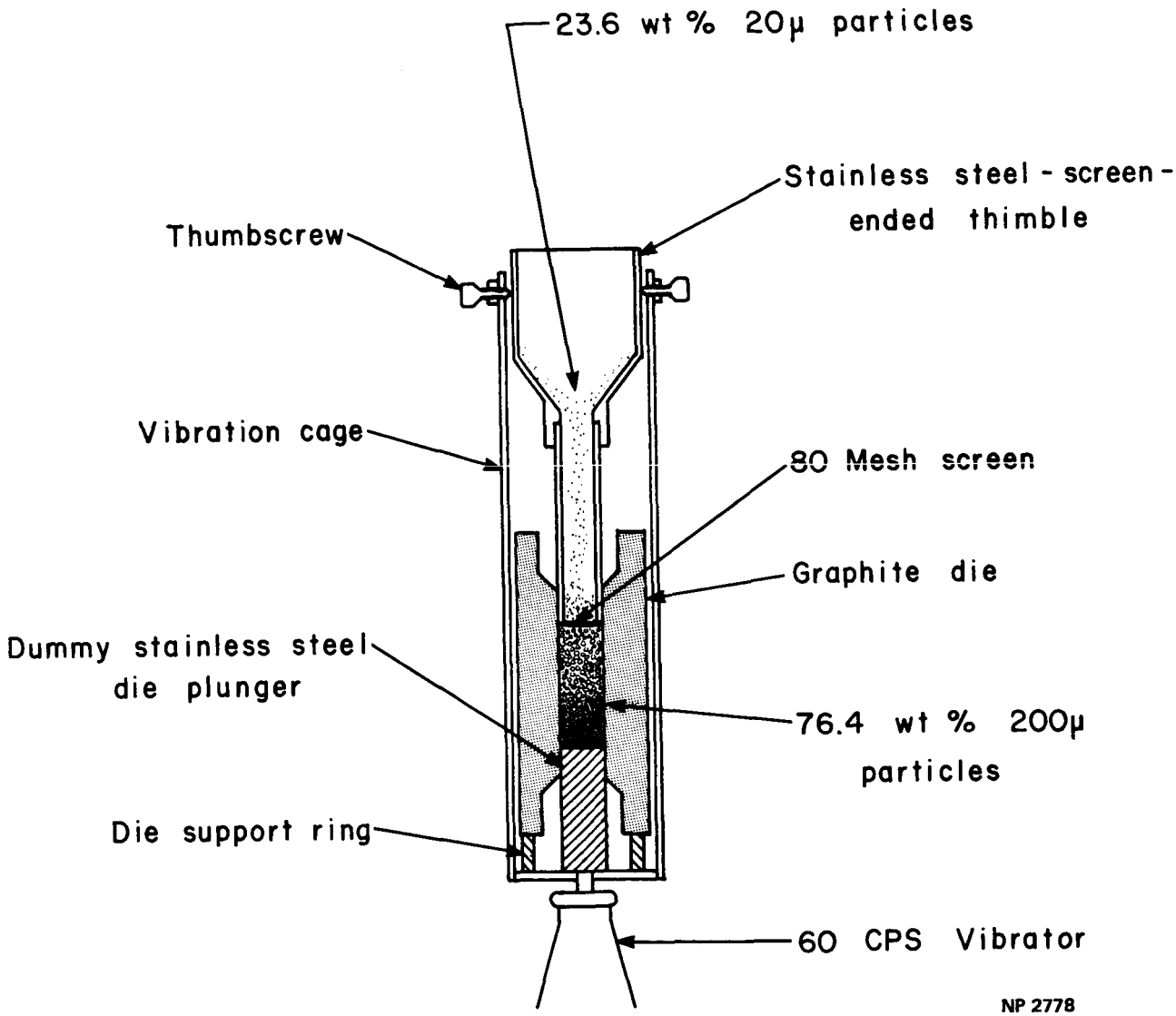

Figure 16. HOT PRESSING DIE LOADING APPARATUS

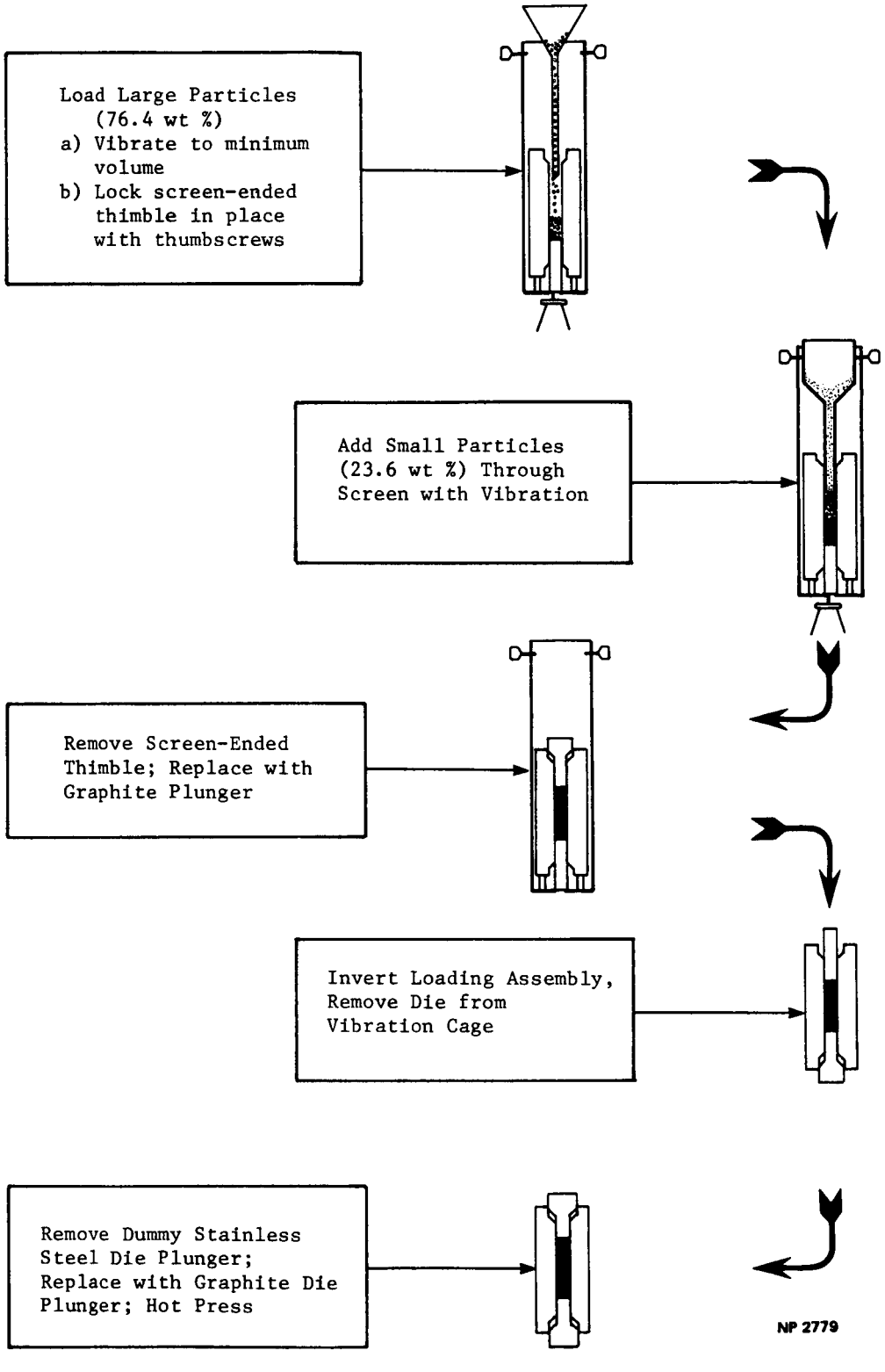

Figure 17. FLOW DIAGRAM FOR DIE LOADING PROCEDURE

approximately 40°C per minute. The effect of pressing pressure on resulting cermet density obtained by this hot pressing procedure is shown in Figure 18. (See Appendix A for the theoretical density of the cermets.)

The hot pressing procedure led to carbon contamination of the cermet pellets near the pellet surfaces. When observed in polarized light, polished sections of the cermet cross-sections show a sharply defined surface layer of optically active grains to a depth of 0.013 inch from the surface. Microhardness probes of the tungsten matrix surrounding the large particles as a function of radial position on a transverse cross-section of the cermets indicated an abrupt transition from hard (DPH 1875) to soft (DPH 375) at nearly the same depth from the surface. The uniformity of hardness across the remainder of the cermet diameter and the correspondence of the "hard" surface layer with the optically active layer in polarized light were taken as evidence that these indicators marked the limit of carbon penetration into the cermet pellets. This contaminated surface layer was removed by grinding before subsequent testing of the cermet bodies.

After grinding, any exposed UO_2 was removed from the sectioned surface cells by dissolution in hot concentrated nitric acid followed by thorough rinsing, ultrasonic cleaning and vacuum drying at 110°C.

C. HEAT TREATING

Heat treatment of the fabricated cermets or of the particles as previously described was conducted in vacuum (approximately 2×10^{-6} torr) in a tungsten resistance furnace or in the dilatometer apparatus tube described in flowing argon at 1 atmosphere. Heating and cooling rates were limited to approximately 35°C per minute and the heat treatment temperature was maintained to within about 25°C.

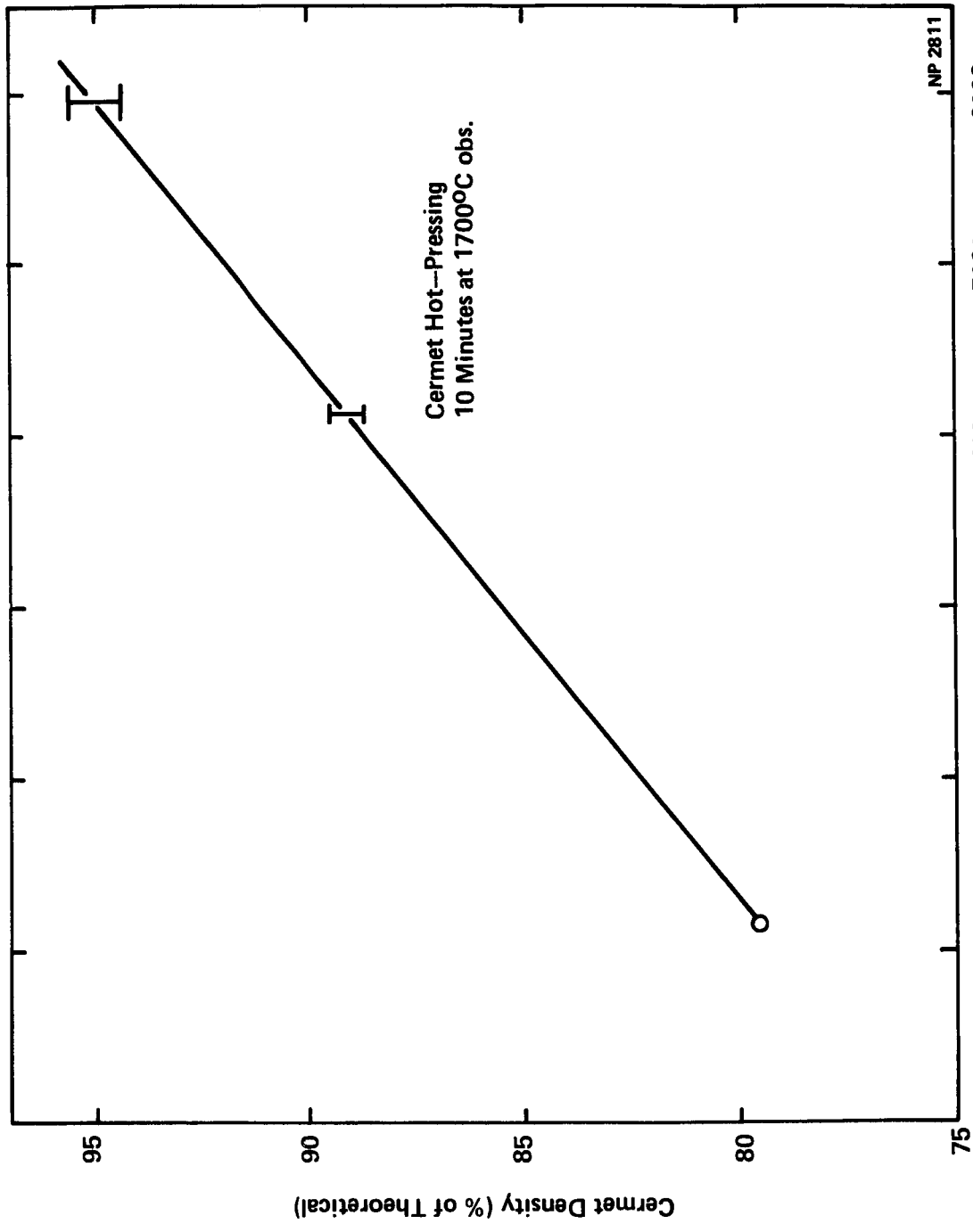

FIGURE 18. EFFECT OF PRESSURE ON DENSITY OF HOT–PRESSED CERMETS

TESTING APPARATUS AND PROCEDURE

A. APPARATUS

An inductively heated tungsten differential dilatometer was used for both thermal expansion measurements and thermal cycling of the cermet bodies. The dilatometer and associated equipment are shown schematically in Figures 19 and 20. The temperature was controlled either by a W/W-25 w/o Re control thermocouple contacting the susceptor (not shown) or by the automatic optical pyrometer as shown in Figure 20. Temperature was measured with a calibrated optical pyrometer through the blackbody holes in the tungsten susceptor and correction was made for the absorbency of the Vycor chamber. Below 700°C, the temperature was determined with the thermocouple based on extrapolation of the thermocouple millivolt output versus specimen temperature obtained at high temperature with the optical pyrometer.

Both thermal expansion measurements and thermal cycling were conducted in slightly greater than 1 atmosphere of flowing argon.

B. THERMAL EXPANSION TESTING

Thermal expansion measurements were made by comparing the change in length of the sample with that of a tungsten blank. The measurements were made at a series of temperatures after the blackbody cavity containing the specimen had been at the desired temperature for a sufficient length of time that there was no longer a detectable drift in the LVDT readings with time.

A temperature dependent calibration factor for the dilatometer apparatus was determined by running two tungsten blanks. Calibration of the apparatus was repeated at frequent intervals during the course of thermal expansion and thermal cycle testing.

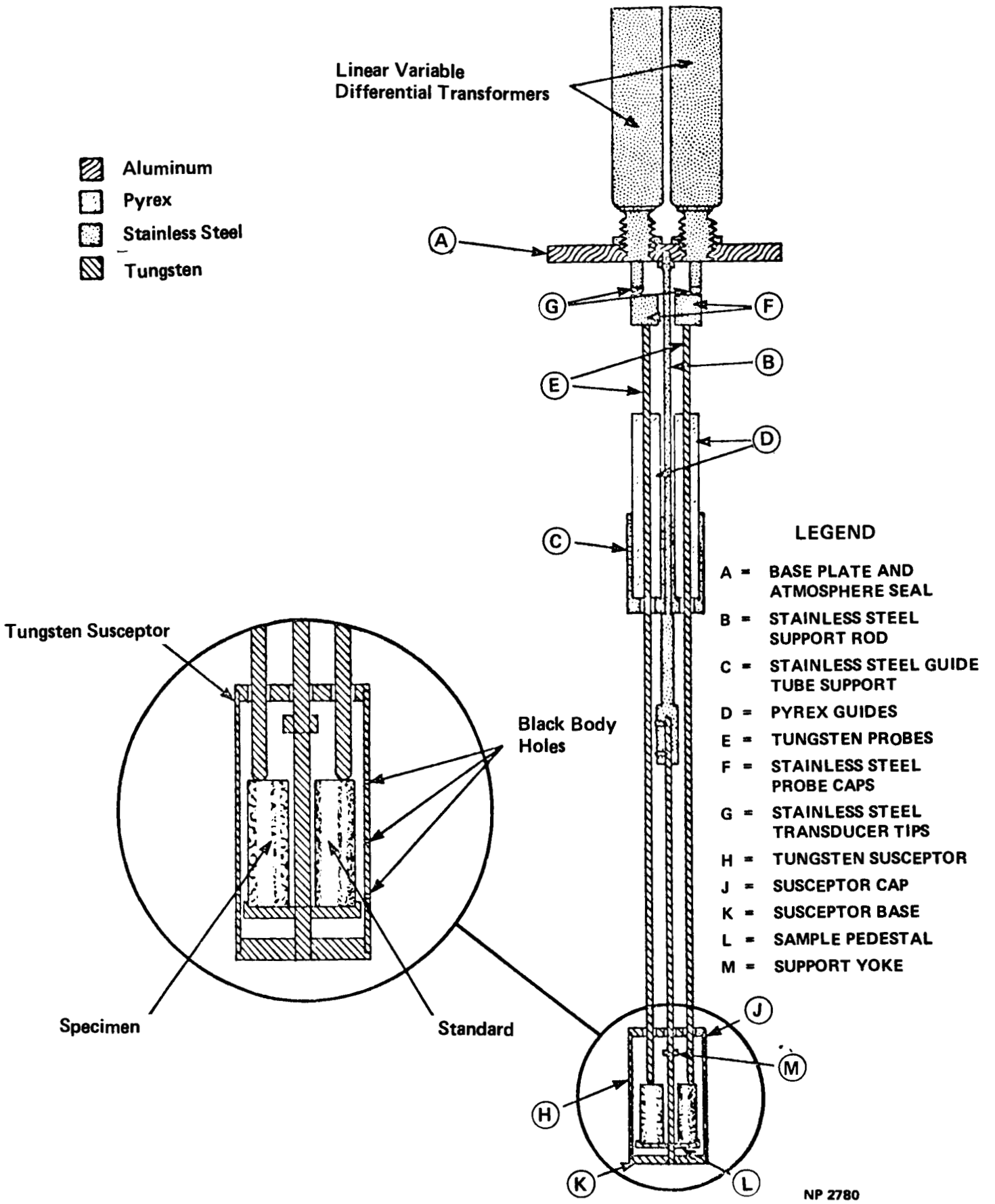

Figure 19. Induction Heated Thermal Expansion and Thermal Cycle Testing Dilatometer

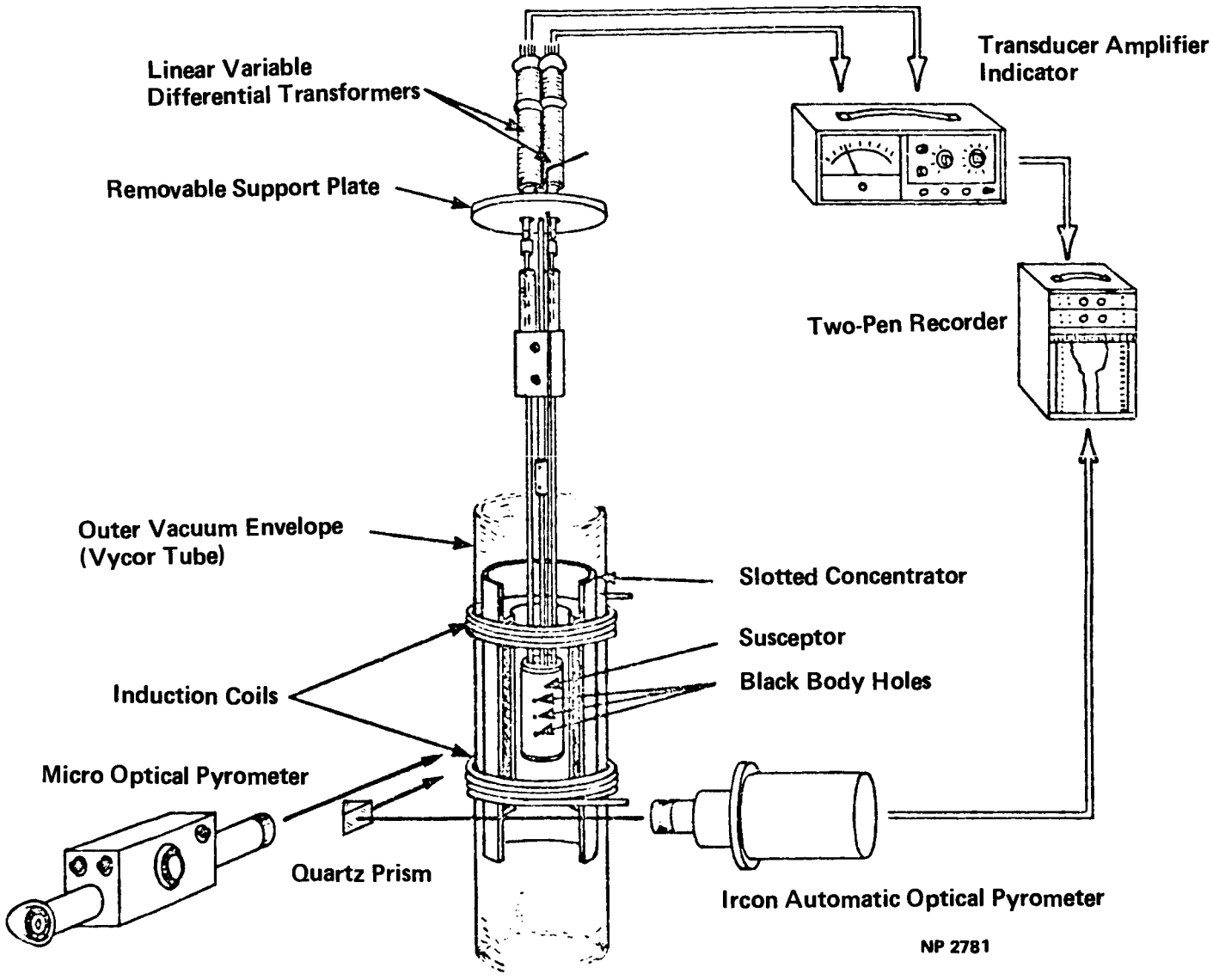

Figure 20. Schematic of Thermal Expansion and Cycling Apparatus

The thermal expansion of tungsten was assumed to be as given by Conway;[6]

$$\frac{\Delta L}{L_{25^\circ C}} \times 100 = 1.14 \times 10^{-3} + 3.68 \times 10^{-4} T + 8.24 \times 10^{-8} T^2, \qquad (2)$$

where ΔL is the change in length from 25°C to the temperature of interest T (in °C) and $L_{25^\circ C}$ is the length at 25°C.

Comparison of the results obtained with the tungsten dilatometer with those obtained on the cermet specimens by optical (telemicroscope) determination of the thermal expansion[15] indicates an accuracy greater than ± 0.02% $\Delta L/L$.

Typical thermal expansion results are shown in Figure 21, which shows the data points taken both on heating and cooling of the as-fabricated specimen #210. The curve drawn through the data was obtained by least-squares fit to a binomial expansion equation through the point representing zero expansion at 25°C; i.e.,

$$\frac{\%\Delta L}{L} = A(T-25^\circ C) + B(T-25^\circ C)^2, \qquad (3)$$

where A and B are the constants determined from the data and T is the temperature in °C.

C. THERMAL CYCLING TEST CONDITIONS

Thermal cycle testing was conducted in the same tungsten dilatometer as used for thermal expansion measurement; the specimen length was continuously monitored during thermal cycling by comparison with the tungsten blank using the LVDT's. The W/W - 25 w/o Re thermocouple was used in conjunction with a closed-loop programmer-controller to operate the induction heater power supply during thermal cycling.

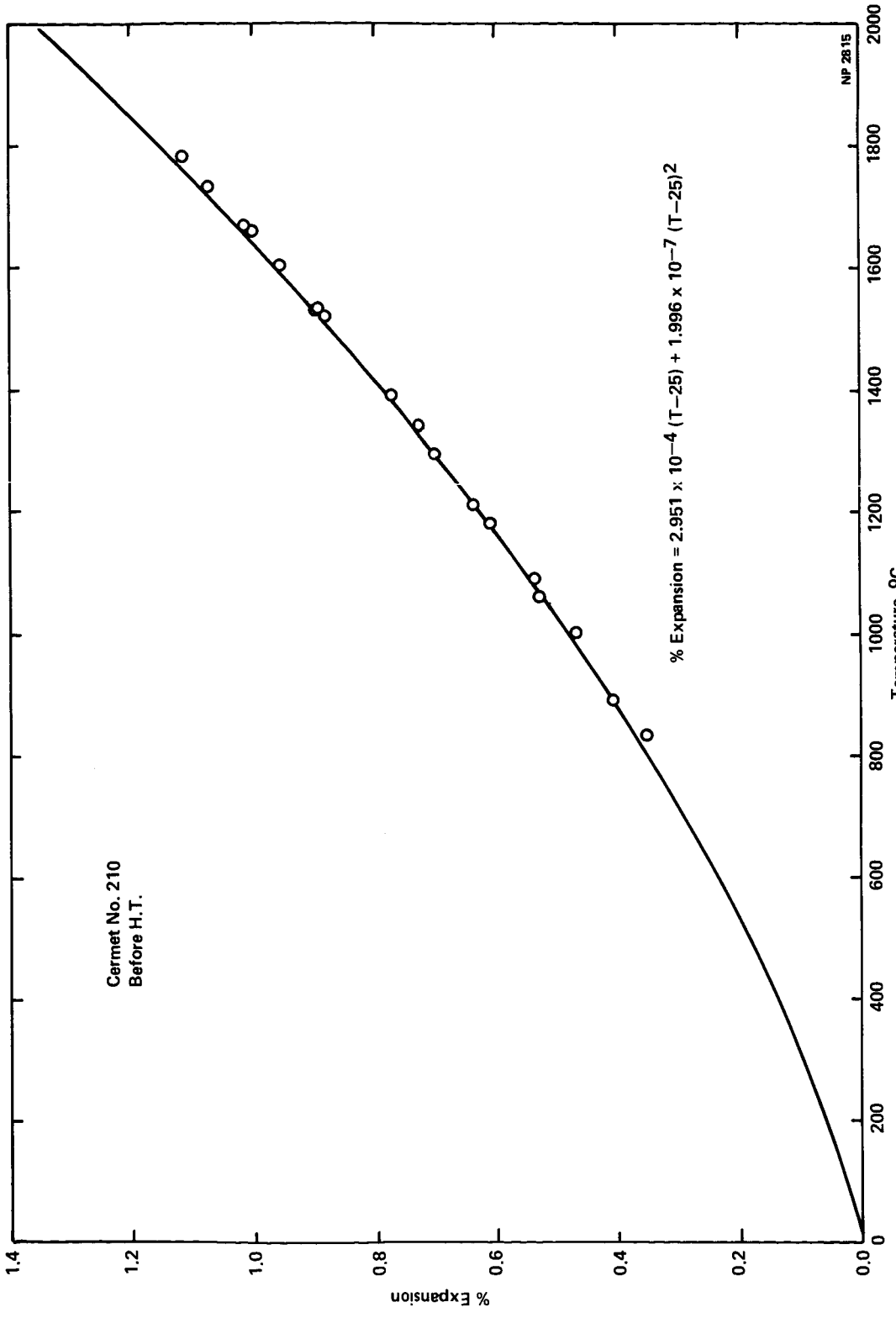

FIGURE 21. TYPICAL THERMAL EXPANSION TEST RESULTS

The thermal cycle used for testing the cermet dimensional and structural stability consisted of heating from 150 to 1600°C at a constant heating rate (34.5°C/minute) in 42 minutes, hold at 1600°C for 30 minutes, cooling as rapidly as possible to 150°C (approximately 13 minutes) and holding at 150°C to a total cycle time of 90 minutes. The thermal cycle testing time-temperature profile is shown in Figure 22 with a previously used testing cycle between 150 and 1600°C for comparison.

The choice of thermal cycle testing conditions is a necessary compromise between the desire to simulate anticipated irradiation experiment or reactor operational conditions with some undetermined additional severity factor, testing apparatus limitations and testing life limitations. The expected heating conditions for irradiation experiments allow approximately two hours for heatup from reactor ambient (600°C) to the operating temperature (approximately 8.5°C/minute). Thus, the heating rate incorporated in the testing cycle is approximately four times that anticipated for irradiation testing of cermet fuels and, in addition, it covers a 450°C broader temperature range. The hold-time at the maximum temperature is believed[8] to be important in limiting damage to tungsten-UO_2 cermet structures. Hold times of only 5 minutes were observed to result in more damage to the microstructure than hold times of 60 minutes. Thus, a compromise of 30 minutes at the maximum temperature was used for the thermal cycle testing conditions. It should be pointed out that reactor experiments or operation would undoubtedly lead to average hold times considerably in excess of 30 minutes (e.g., ~300 hours for average irradiation experiments) which implies that the testing cycle again imposes a certain degree of additional severity with regard to the hold time at temperature. Cooling rates to be expected in thermionic devices on reactor scram or withdrawal of an irradiation assembly may somewhat exceed the maximum possible cooling rates achievable with the

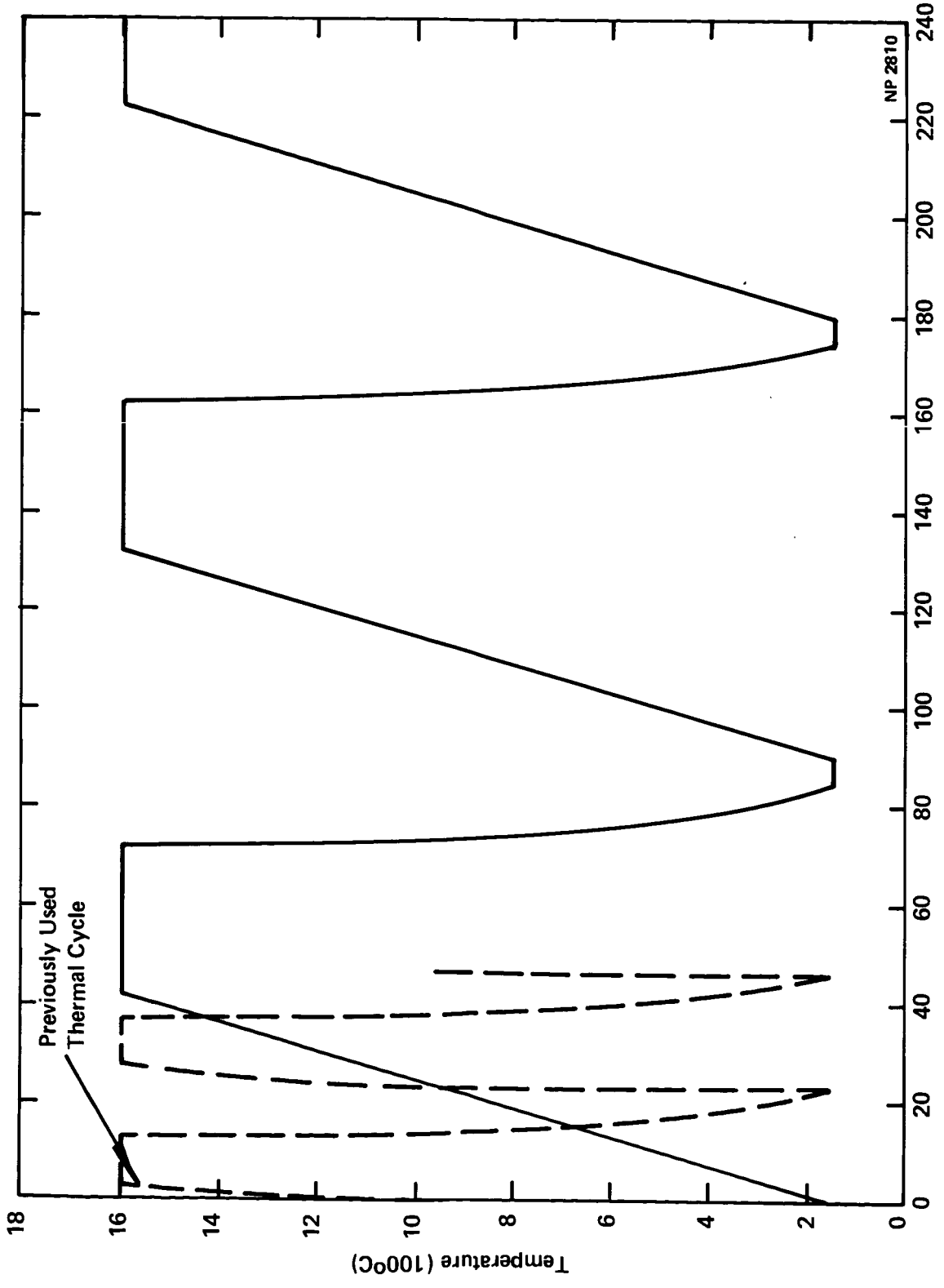

FIGURE 22. THERMAL CYCLE TEST CONDITIONS

thermal cycling device due to the additional energy transfer from electron cooling and the greater thermal inertia of the testing apparatus. The cooling rate achieved is at least as severe as any previously used for thermal cycle testing of cermets.

EXPERIMENTAL RESULTS

A. STRUCTURE OF AS-FABRICATED CERMETS

The uniformity of the distribution of small and large particles in the cermets is illustrated in the cross-sections of a high density (approximately 95 percent) as hot pressed specimen shown in Figure 23.

Two types of cermet structures were thermal expansion and thermal cycle tested; i. e., nominally 90 and 95 percent of theoretical density. The microstructures of these two types of cermets as fabricated are shown in Figures 24, 25, 26, and 27.

Essentially all of the interparticle porosity was eliminated in the 95 percent density specimens as shown in Figures 24 and 25. Some void was retained inside the tungsten shell of the large particles both in the form of a slight particle-matrix gap and more or less uniformly distributed porosity throughout the fuel. The few grain boundaries that do exist in the large UO_2 particles appear to be essentially continuous networks of porosity, or even a gap. Most of the small particles have been essentially completely densified, with an occasional large pore retained in the fuel. There is some breakup of the continuous tungsten matrix in the small particles.

Some interparticle porosity was not eliminated in the case of the low density (90 percent) specimens as shown in Figures 26 and 27. The large particles show considerable connected porosity retained in the UO_2 and a slight particle-matrix gap (Figures 26 through 29). The UO_2 appears as fairly large (>20 micrometer diameter) dense grains in the large particles. There are a few <1 micrometer diameter bubbles on the tungsten grain boundaries and, also, on the UO_2 grain boundaries (Figures 28 and 29). The small particles again appear to either contain a single pore or no porosity.

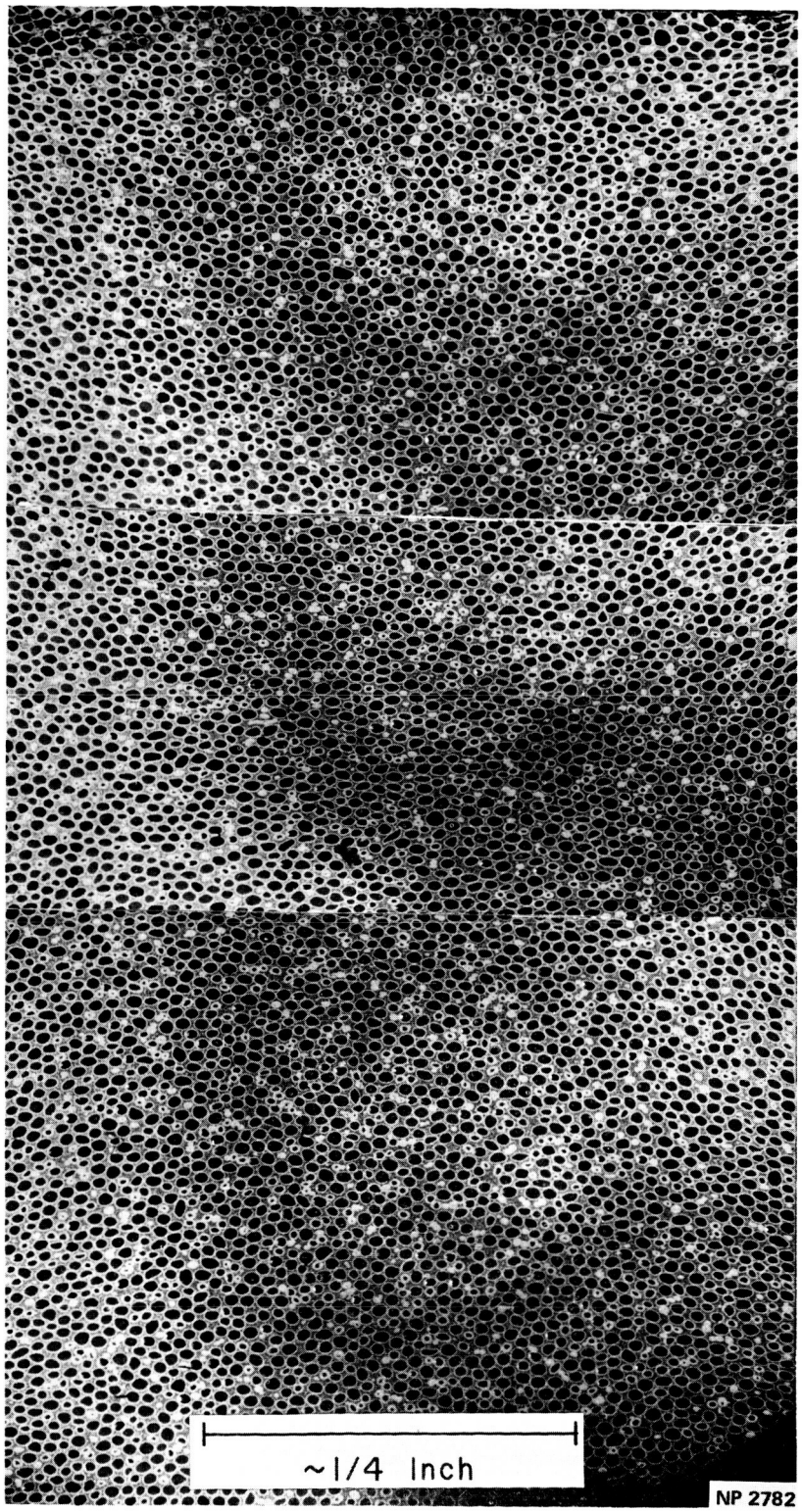

Figure 23. Longitudinal Cross-section of as Hot-Pressed High Density (95%) Cermet—Note Uniformity of Particle Distribution

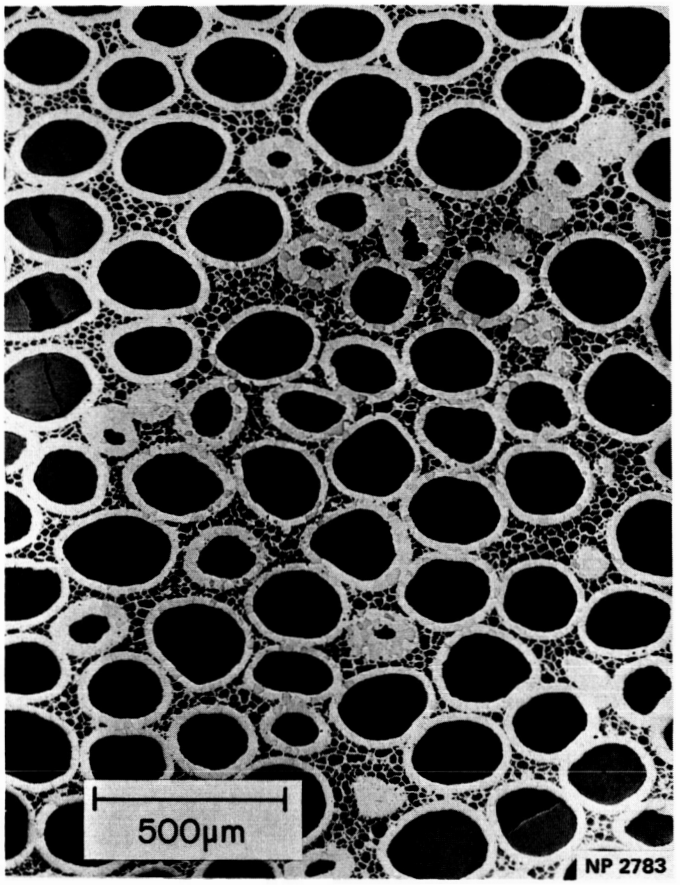

Figure 24. As Hot-Pressed High Density (95%) Cermet (No. 205)

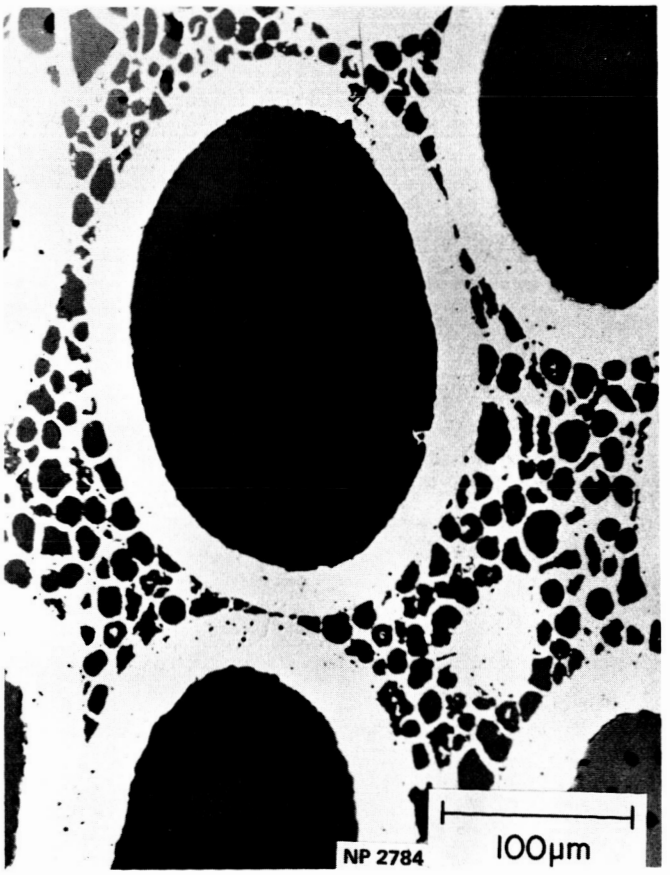

Figure 25. As Hot-Pressed High Density (95%) Cermet (No. 205)

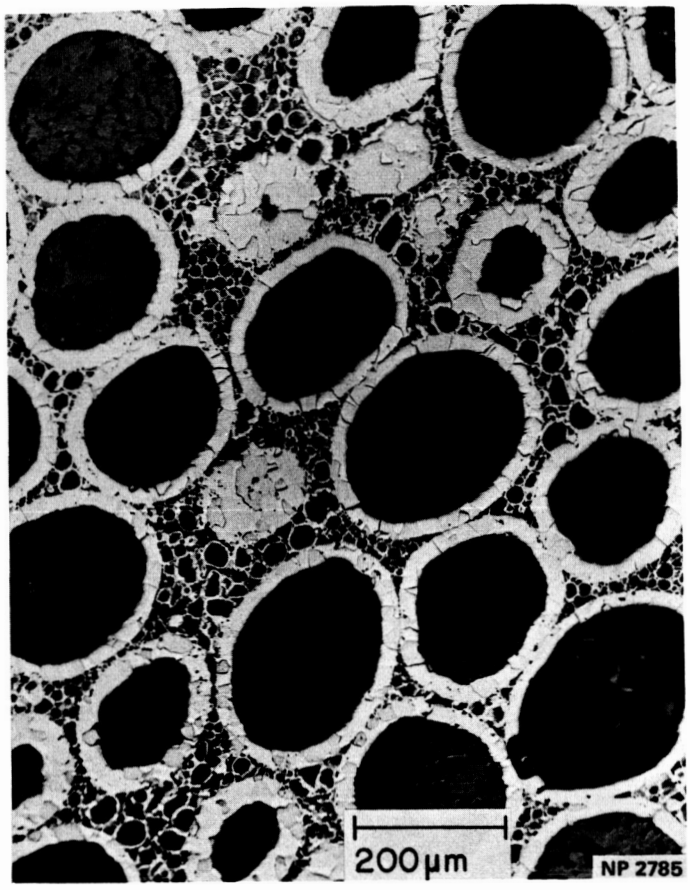

Figure 26. As Hot-Pressed Low (90%) Density Cermet (No. 216)

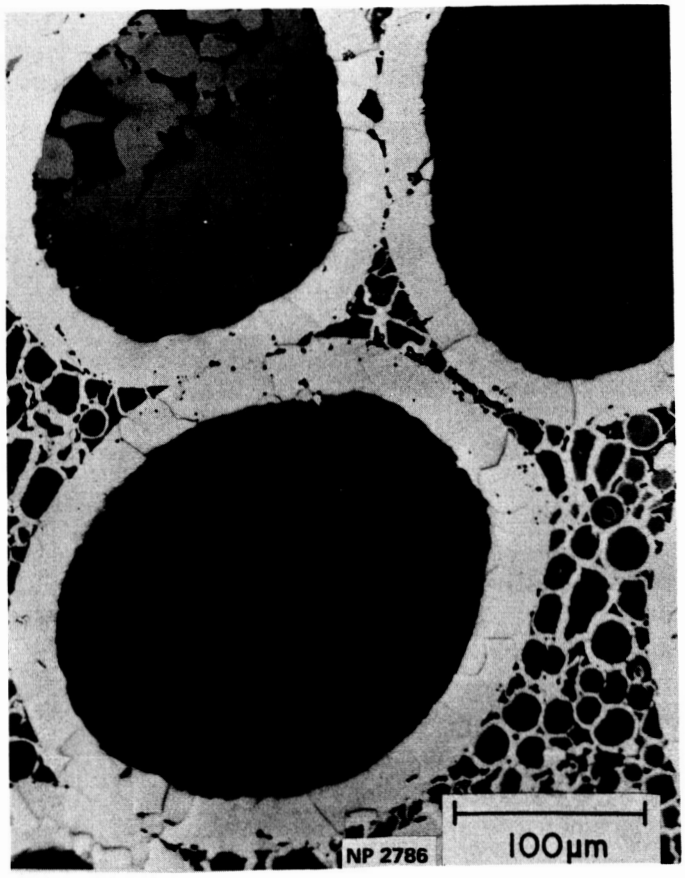

Figure 27. As Hot-Pressed Low (90%) Density Cermet (No. 216)

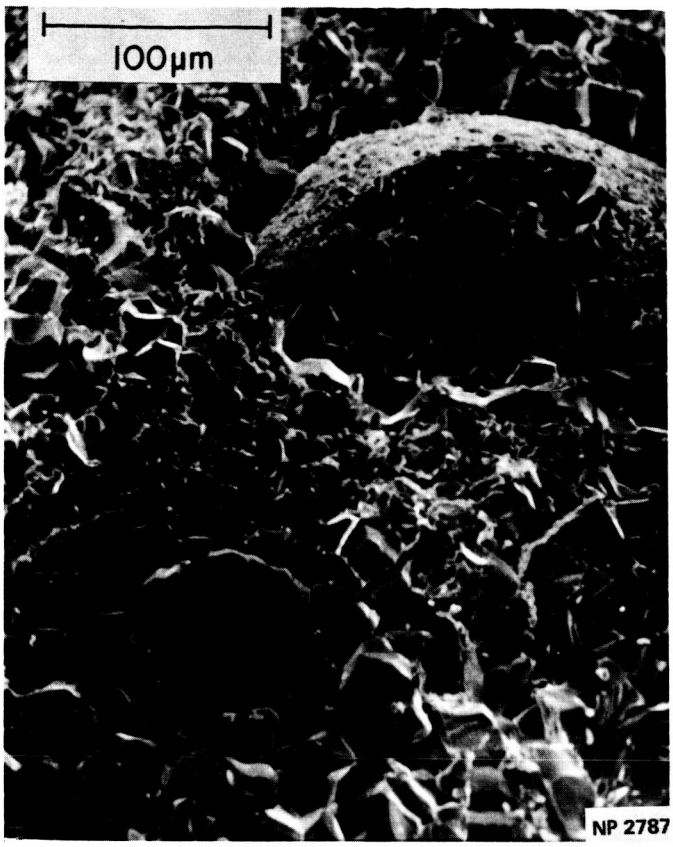

Figure 28. Fracture Surface of Low Density (90%) Hot-Pressed Cermet—Note Open Porosity and Grain Boundary Bubbles in Large UO_2 Particles

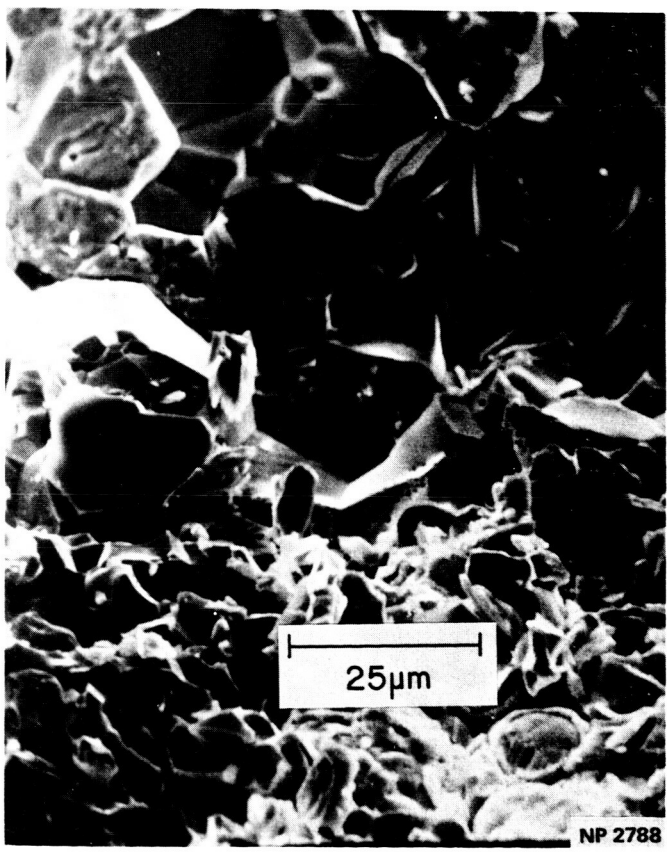

Figure 29. Fracture Surface of Low (90%) Density Hot-Pressed Cermet—Note Grain Boundary Bubbles in Tungsten

B. SUMMARY OF EXPERIMENTAL TESTS AND SPECIMEN HISTORY

The specimens fabricated and the experimental tests conducted are summarized in Table 2. The chronological history of a specimen is read from left to right in the table.

C. THERMAL EXPANSION BEHAVIOR OF CERMETS

The cermet thermal expansion behavior is summarized in Table 3 which gives the results of least-squares analysis of the expansion data for each specimen and lists the expansion evaluated from the least-squares analyses at 1600°C.

The thermal expansion of the as-fabricated 95 percent dense specimens is shown in Figure 30 where it is compared with the expansion of tungsten,[6] UO_2,[5] and previously studied conventional tungsten-60 volume percent UO_2 cermets. The expansion of the cermets in this group showing the largest expansion (#212) and the lowest expansion (#210) in the as-fabricated condition are shown as well as the mean expansion of the group which is given by the relationhip:

$$\frac{\%\Delta L}{L} = (3.424 \pm 0.291) \times 10^{-4}(T-25) + (1.865 \pm 0.139) \times 10^{-7}(T-25)^2, \qquad (4)$$

where the tolerance limits are for the 90 percent confidence interval for the mean (i. e., the mean value of the thermal expansion of the as-fabricated 95 percent dense cermets can be said to fall within the range of the tolerance limits with 90 percent confidence).

Note that a considerable decrease in the thermal expansion of the cermets compared to previous cermets of approximately the same composition was achieved.

The effect of heat treatment for 24 hours at 1800°C on the thermal expansion of the 95 percent dense cermets was studied on

Table 2. SUMMARY OF EXPERIMENTAL TESTS AND SPECIMEN HISTORY

Specimen Number	As-Pressed Density (% Theoretical)	As-Pressed Metallography	Thermal Expansion Test**	Metallography After Expansion	Reexpansion Test	NMPO++ Expansion Test	Metallography	Heat Treat	As Heat-Treated Metallography	Expansion Test After Heat Treat**	NMPO Expansion++ Test After Heat Treat	Metallography	Thermal Cycle (50 Cycles)	Number of Thermal Cycles at Which Metallography was Obtained	Scanning Electron Microscopy
205	94.29	X													
206	95.33*		X	X	X	X(2)	X								X
207	95.51*		X(2)	X	X(2)										X
208	95.39*							X(1700°C–24 hr)+	X	X					X
209	95.58*		X(4)					X(1800°C–24 hr)		X(2)	X(4)	X			X
210	95.18*		X(2)					X(1900°C–24 hr)		X(2)		X			X
211	95.38*							X(1800°C–24 hr)+		X(3)		X			X
212	95.55*		X(2)					X(1800°C–24 hr)+		X(4)					X
213	94.85*												X(15,10,25)	50	X
214	79.24	X													
215	88.60	X													X
216	88.58	X	X(2)					X(1800°C–24 hr)+		X(4)			X(10,25,15)	10,35,50	X
218	89.28	X	X					X(2000°C–24 hr)		X			X(15,15,20)	15,30,50	X

* Based on ground weight and dimensions of specimen (theoretical density = 14.9174 gm/cm^3).

** Numbers in parentheses refer to number of thermal expansion test runs made on specimen.

\+ Heat treated in dilatometer apparatus.

++ Telemicroscopic expansion tests run at GE/NMPO.[15]

Table 3. SUMMARY OF CERMET THERMAL EXPANSION RESULTS

Specimen Number	Linear Thermal Expansion* (%)	Expansion at 1600°C (%)
A. AS-FABRICATED CERMETS		
(1) 95% Dense		
206	$3.647 \times 10^{-4}(T-25) + 1.705 \times 10^{-7} (T-25)^2$	0.997
207	$3.302 \times 10^{-4}(T-25) + 1.983 \times 10^{-7} (T-25)^2$	1.011
209	$3.714 \times 10^{-4}(T-25) + 1.709 \times 10^{-7} (T-25)^2$	1.009
210	$2.951 \times 10^{-4}(T-25) + 1.996 \times 10^{-7} (T-25)^2$	0.960
212	$3.508 \times 10^{-4}(T-25) + 1.933 \times 10^{-7} (T-25)^2$	1.032
(2) 90% Dense		
216	$4.161 \times 10^{-4}(T-25) + 1.251 \times 10^{-7} (T-25)^2$	0.966
218	$4.292 \times 10^{-4}(T-25) + 1.374 \times 10^{-7} (T-25)^2$	1.017
B. HEAT-TREATED CERMETS (All Heat Treatments for 24-hour Duration)		
(1) 95% Dense		
208 (1700°C)	$3.050 \times 10^{-4}(T-25) + 2.354 \times 10^{-7} (T-25)^2$	1.064
209 (1800°C)	$4.280 \times 10^{-4}(T-25) + 0.989 \times 10^{-7} (T-25)^2$	0.919
21 210 (1900°C)	$3.317 \times 10^{-4}(T-25) + 2.029 \times 10^{-7} (T-25)^2$	1.026
211 (1800°C)	$4.090 \times 10^{-4}(T-25) + 1.549 \times 10^{-7} (T-25)^2$	1.028
212 (1800°C)	$4.138 \times 10^{-4}(T-25) + 1.595 \times 10^{-7} (T-25)^2$	1.048
(2) 90% Dense		
216 (1800°C)	$3.621 \times 10^{-4}(T-25) + 1.527 \times 10^{-7} (T-25)^2$	0.949
218 (2000°C)	$4.211 \times 10^{-4}(T-25) + 1.710 \times 10^{-7} (T-25)^2$	1.087

*T = Temperature (°C) obtained from least squares fit of experimental data.

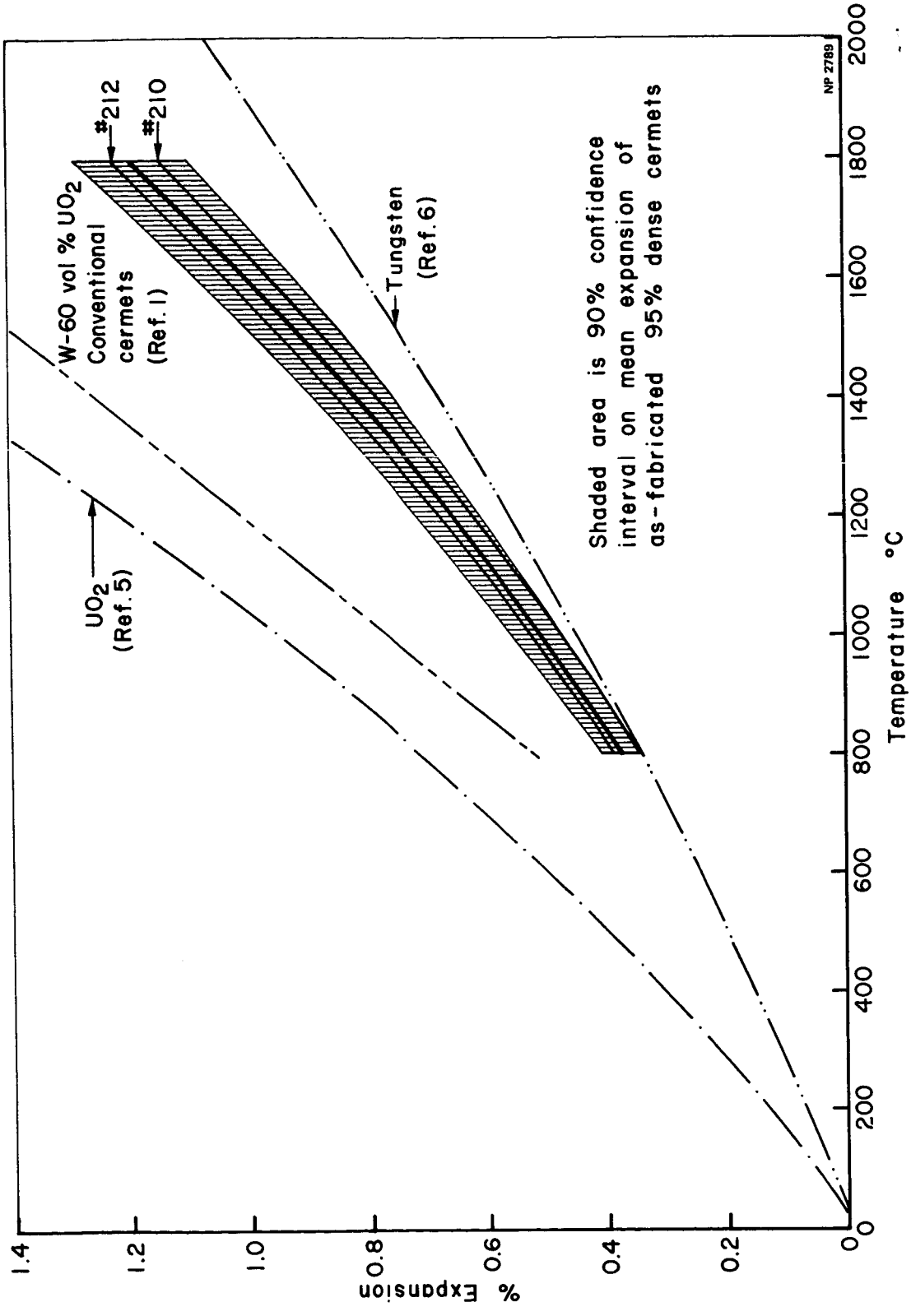

Figure 30. THERMAL EXPANSION OF AS-FABRICATED HIGH DENSITY CERMETS

three specimens (#209, #211, and #212). The mean expansion of these heat treated specimens is given by the following relationship:

$$\frac{\%\Delta L}{L} = (4.169 \pm 0.158) \times 10^{-4}(T-25) + (1.378 \pm 0.538) \times 10^{-7}(T-25)^2, \quad (5)$$

where the limits express the 90 percent confidence interval for the mean expansion as obtained from the least-squares fits of the experimental data. The mean value and the 90 percent confidence interval are shown in Figure 31 with the same confidence interval for the as-fabricated specimens for comparison.

The thermal expansion of 95 percent dense specimens (#208 and #210) heat treated at 1700°C and at 1900°C also fell completely within the 90 percent confidence interval for those specimens heat treated at 1800°C shown in Figure 31.

Decreasing the density of the cermets to 90 percent of theoretical had little effect on their thermal expansion in the as-fabricated condition. The mean expansion of the 90 percent dense as-fabricated cermets is given by the relationship:

$$\frac{\%\Delta L}{L} = (4.227 \pm 0.301) \times 10^{-4}(T-25) + (1.313 \pm 0.282) \times 10^{-7}(T-25)^2, \quad (6)$$

where the limits are as before. The thermal expansion band described by this relationship (equation 6) is shown superimposed on that of the 95 percent dense as-fabricated cermets in Figure 32. Note the close proximity of the means and the almost complete overlap of the uncertainty bands.

Heat treatment of the 90 percent dense cermets at 1800°C and 2000°C for 24 hours also failed to significantly alter the thermal expansion as shown in Figure 33.

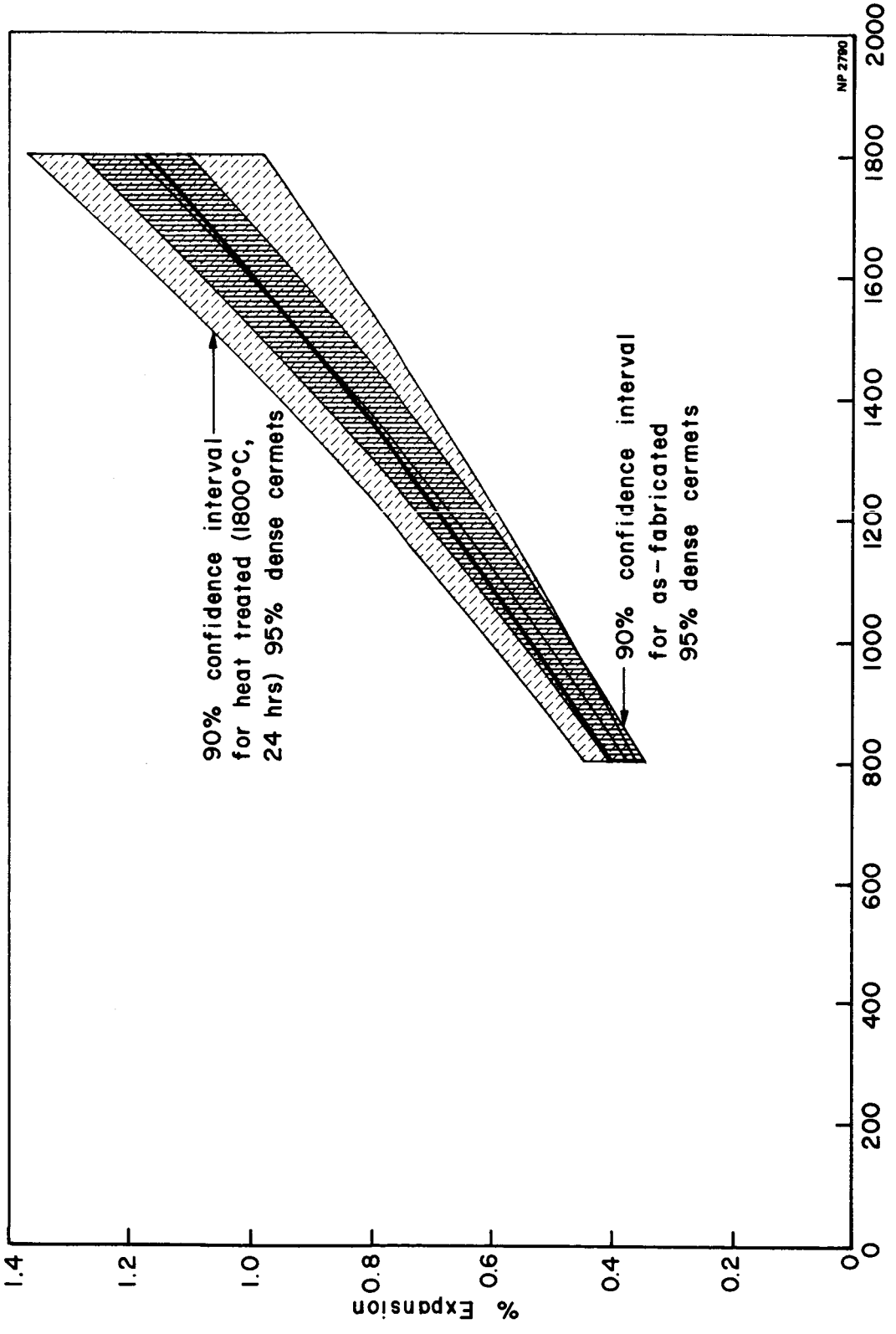

Figure 31. THERMAL EXPANSION OF HEAT TREATED HIGH DENSITY CERMETS

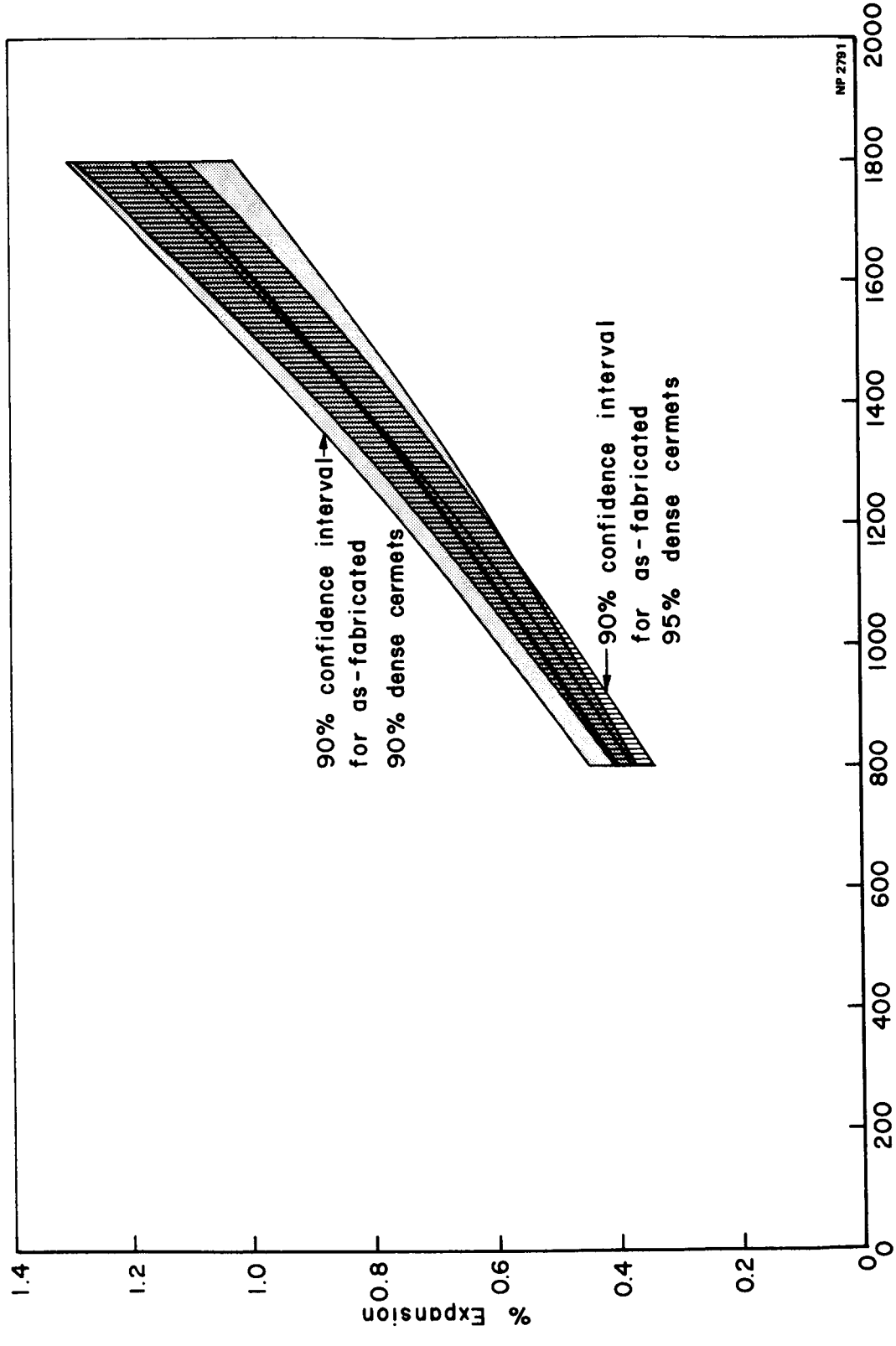

Figure 32. THERMAL EXPANSION OF AS-FABRICATED LOW DENSITY CERMETS

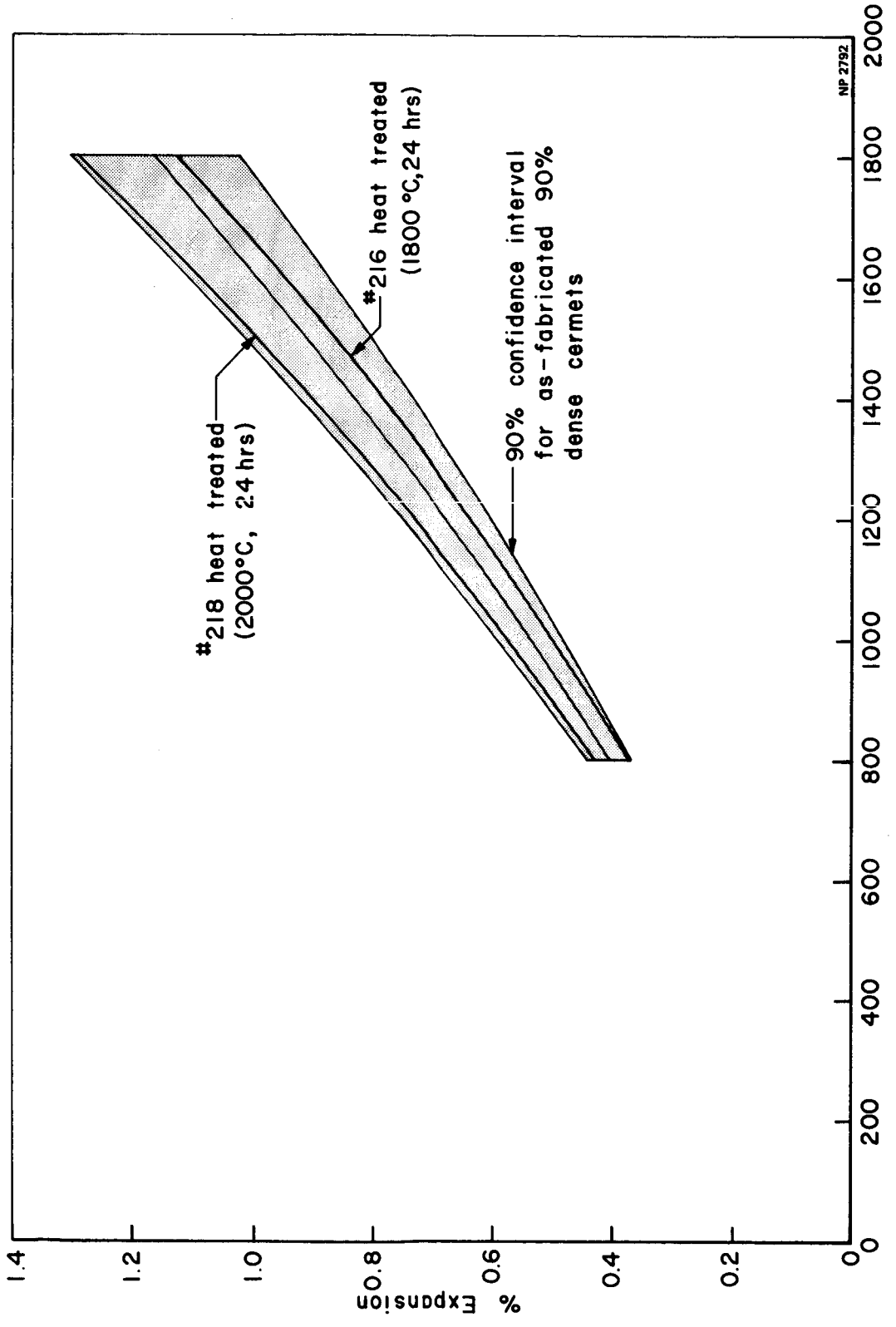

Figure 33. THERMAL EXPANSION OF HEAT TREATED LOW DENSITY CERMETS

The random nature of the effects of cermet density (90 to 95 percent) and heat treatment (24 hours at 1700 to 2000°C) on the thermal expansion of the cermets is further illustrated in Figure 34 which shows diagrammatically the effects of these variations on the cermet expansion at 1600°C as determined from the least squares fits of the experimental data. Note that no clear trend of either of these effects can be determined, let alone a quantitative assessment of their effects.

Thus, from the experimental results, it appears that the thermal expansion of the cermets is statistical in nature--i. e., it does not have a set value as might be expected for a well annealed, pure metal but rather, for a given set of specimens, a range of values will be obtained. This range of values is undoubtedly the result of variations in the starting material and the fabrication procedure. Improved control of processing parameters might lead to improved reproducibility of the thermal expansion of the cermets. Heat treatment for 24 hours at 1700 to 2000°C is not sufficient to eliminate this innate variability in the thermal expansion of the cermets and, in fact, it is expected that many specimens would be required to determine the direction and the magnitude of any changes in expansion due to the heat treatment. The limited number of specimens produced does not allow a full appraisal of the spectrum of variability.

D. CERMET DIMENSIONAL CHANGES DURING HEAT TREATMENT AND THERMAL EXPANSION MEASUREMENTS

The thermal expansion measurements (i. e., holding at various temperatures up to 1800°C) and heat treatments for 24 hours at 1700 to 2000°C produced some permanent dimensional changes in the cermets. These dimensional changes are summarized in Table 4. It should be pointed out that the permanent changes in dimensions were determined by measurement of the specimens with a frequently-calibrated micrometer.

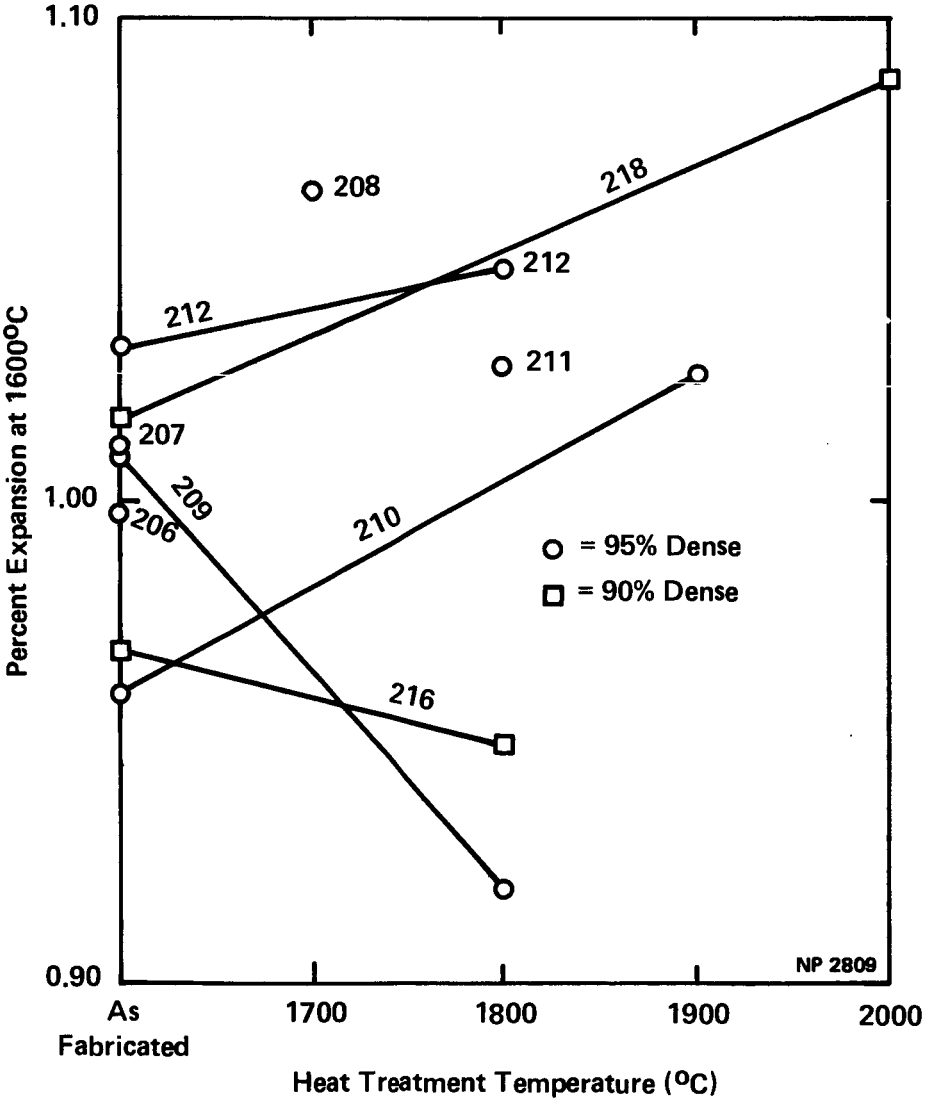

FIUGRE 34. EFFECT OF HEAT TREATMENT FOR 24 HOURS ON CERMET THERMAL EXPANSION AT 1600°C

Table 4. PERMANENT DIMENSIONAL CHANGES OF CERMETS AS A RESULT OF THERMAL EXPANSION

Specimen Number	Test Number	Treatment: Expansion Test As-Fabricated — Dimension Changes/Test: $\frac{\Delta L}{L}$ (mils/inch)	Expansion Test As-Fabricated — $\frac{\Delta D^{**}}{D}$ (mils/inch)	Heat Treatment: $\frac{\Delta L}{L}$ (mils/inch)	Heat Treatment: $\frac{\Delta D^{**}}{D}$ (mils/inch)	Expansion Test Post Heat-Treatment: $\frac{\Delta L}{L}$ (mils/inch)	Expansion Test Post Heat-Treatment: $\frac{\Delta D^{**}}{D}$ (mils/inch)
206	1	0.2	0.2				
	2	0.7					
	3	0.5*	0.25*				
	4	0.6	0.25				
		(0.65)+	(0.23)+				
207	1	0.35*	1.0				
	2	0.35					
	3	0.35*					
	4	0.35					
		(0.35)+	(1.0)+				
208	1			-1.1	-0.2	0.7	1.2
	2			(1700°C)		-0.2	
						(0.25)+	(1.2)+
209	1	1.25*	0.55*	2.6	2.0	0.1*	0.6*
	2	1.25*	0.55*	(1800°C)		0.1	0.6
	3	1.25*	0.55*			0.2*	0.55*
	4	1.25	0.55			0.2*	0.55*
						0.2*	0.55
		(1.25)+	(0.55)+			(0.16)+	(0.57)+
210	1	0.1*	0.0*	0.4	0.2	0.4*	0.35*
	2	0.1	0.0	(1900°C)		0.4	0.35
		(0.1)	(0.0)+			(0.4)	(0.35)+
211	1			0.9	-0.2	0.1*	0.35*
	2			(1800°C)		0.1	0.35
	3					0.6	2.2
						(0.27)+	(0.95)+
212	1	-0.1	0.0	1.3	0.0	-0.8	0.0
	2	0.1	0.5	(1800°C)		0.0	0.0
						0.35	0.0
		(0.0)+	(0.25)+			(-0.15)+	(0.0)+
216	1	0.45*	0.4*	1.2	0.0	0.0	0.0
	2	0.45	0.4	(1800°C)		0.35	0.0
						0.35	0.0
						0.35	0.0
		(0.45)+	(0.4)+			(0.26)+	(0.0)+
218	1	0.25	0.0	0.0	0.0	0.0	0.0
		(0.25)+	(0.0)+	(2000°C)		(0.0)+	(0.0)+

* No measurement made; value estimated by averaging over consecutive test(s) with asterisks to first unasterisked value.

** Measured at longitudinal midplane.

\+ Average dimensional change per thermal expansion run (mils/inch).

The estimated accuracy of such measurements are approximately $\pm$ 0.2 mils per inch for length changes and $\pm$ 0.4 mils per inch for diameter changes (see Appendix B). The dimensional changes during the thermal expansion runs were sometimes detectable as a slight hysteresis between the thermal expansion data on heating and cooling. (15)

The magnitude of the dimensional changes during a thermal expansion run (e. g. , a few tenths of a mil per inch per run) are not indicative of a dimensionally stable structure since these changes, if they persist, would amount to tens of mils per inch in the course of a hundred such thermal treatments. Note that dimensional changes per heat-up cycle are of the same order of magnitude as occurred after heat treatment as well as before for most of the cermets. The dimensional changes produced during a long-term heat treatment [i. e. , 24 hours at 1800°C (specimens #209, #211, and #212)] were not reproducible on the same type of cermet. It will be seen that these permanent dimensional changes per heat-up cycle are approximately the same as observed during thermal cycle testing.

The only indication of a microstructural change in the cermets after thermal expansion testing was a possible growth or coarsening of the grain boundary bubbles or pores in the UO_2 phase in the large particles, as shown in Figures 35 and 36, compared with Figures 24 and 25. The qualitative nature of this observation should be emphasized. Scanning electron micrographs of fracture surfaces of the thermal expansion tested specimens showed no readily observable change from the structure shown in Figure 29, for an as-fabricated low density specimen.

Heat treatment of the high density cermets for 24 hours in the range of 1700 to 1900°C lead to coarsening of the bubbles or pores in the UO_2 and opening up of the UO_2 grain boundaries and of portions of

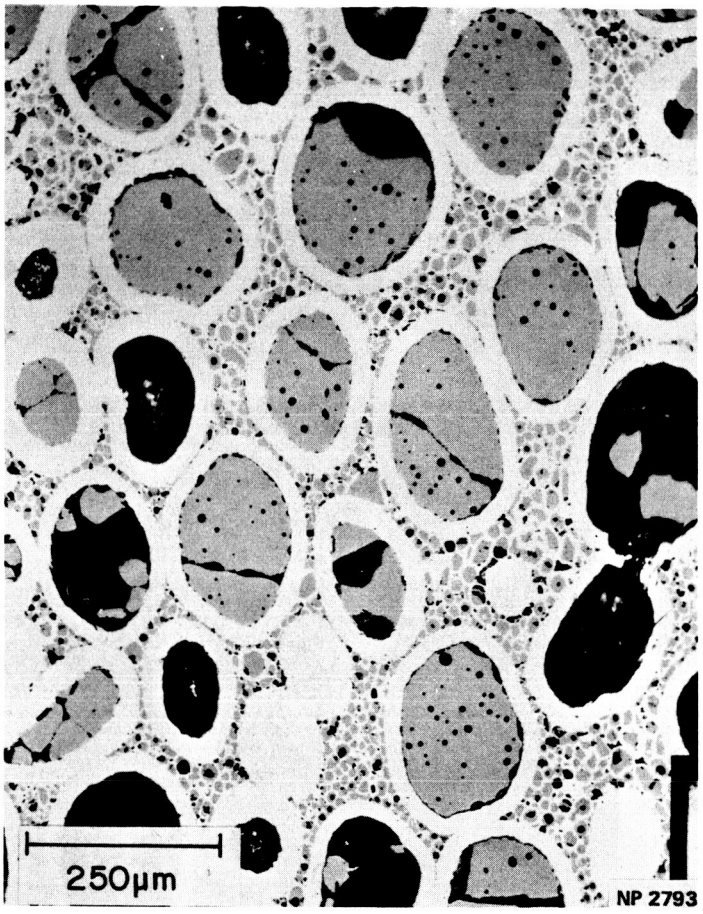

Figure 35. High (95%) Density Cermet After Thermal Expansion Testing

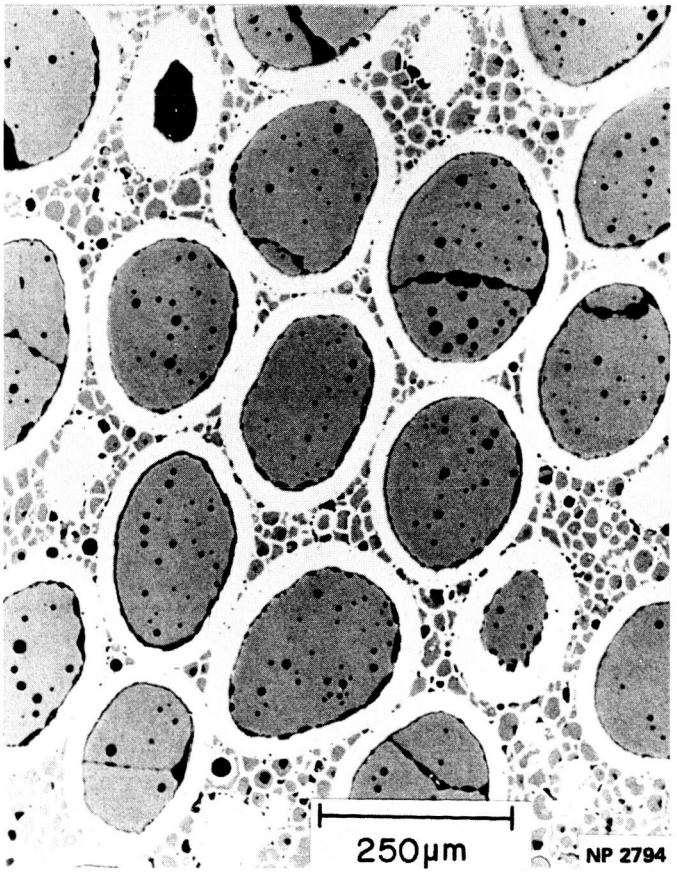

Figure 36. High (95%) Density Cermet After Thermal Expansion Testing

the particle-matrix gap in the case of the large particles as shown in Figures 37, 38, and 39 (see Figure 24 for as-fabricated structure). The heat treatments also produced considerable increase in the number and size of the bubbles in the tungsten grain boundaries as shown in Figures 40 and 41, when compared with the bubble structures before heat treatment, previously shown in Figure 29.

E. THERMAL CYCLING BEHAVIOR OF CERMETS

The cermet thermal cycling behavior--i. e., the observed diametral and axial dimensional changes--is summarized in Figures 42 and 43. The plotted points were obtained by measurement with a frequently calibrated micrometer and the accuracy of these measurements is as previously discussed (Appendix B). The continuous record for the length changes of the cermets always agreed within a few tenths of a mil per inch with the micrometer measurements and showed only monotonic growth of the cermets with cycling. The growth was essentially isotropic; based on the growth at 50 cycles, the growth rate was in the range of 0. 30 to 0. 39 mils per inch per cycle in both the axial and diametral directions for all three specimens tested.

The measured growth rates are nearly as large as any reported when averaged over 100 thermal cycles for tungsten-UO_2 [7] cermets and are approximately twice the largest growth rates obtained by hot pressing of high density monodisperse tungsten-coated particles. [1]

The detectable structural changes in the 95% dense cermet #215 after 50 thermal cycles were again associated with the surface or grain boundary pores or bubbles in the tungsten and the large UO_2 particles. In the tungsten, the grain boundary bubbles have begun to link up significantly, with some boundaries essentially completely separated as shown in Figures 44 and 45. The pores or bubbles on the UO_2 grain boundaries and especially at the tungsten-UO_2 interface

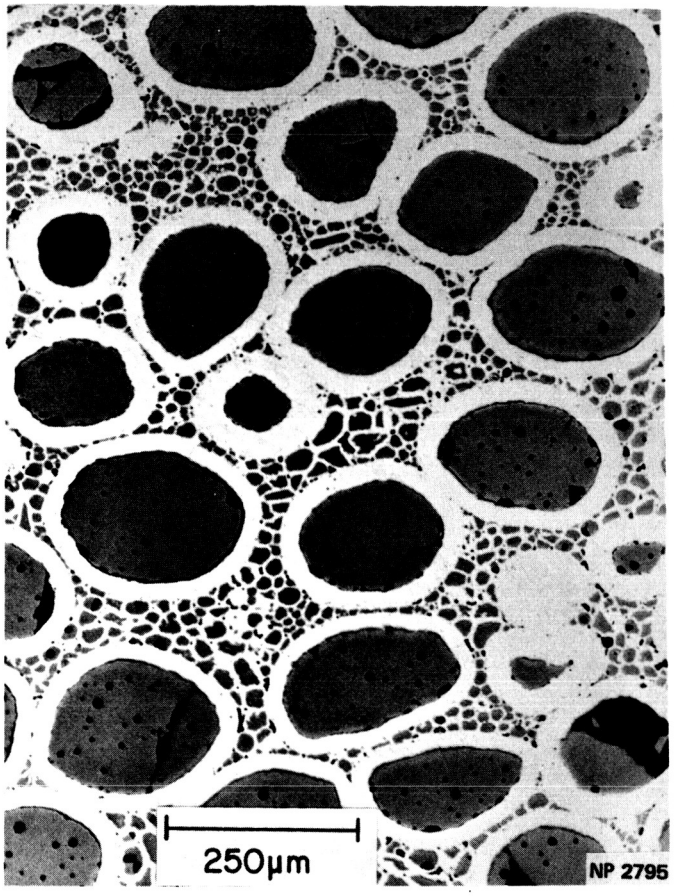

Figure 37. High (95%) Density Cermet Heat Treated at 1700°C for 24 Hours

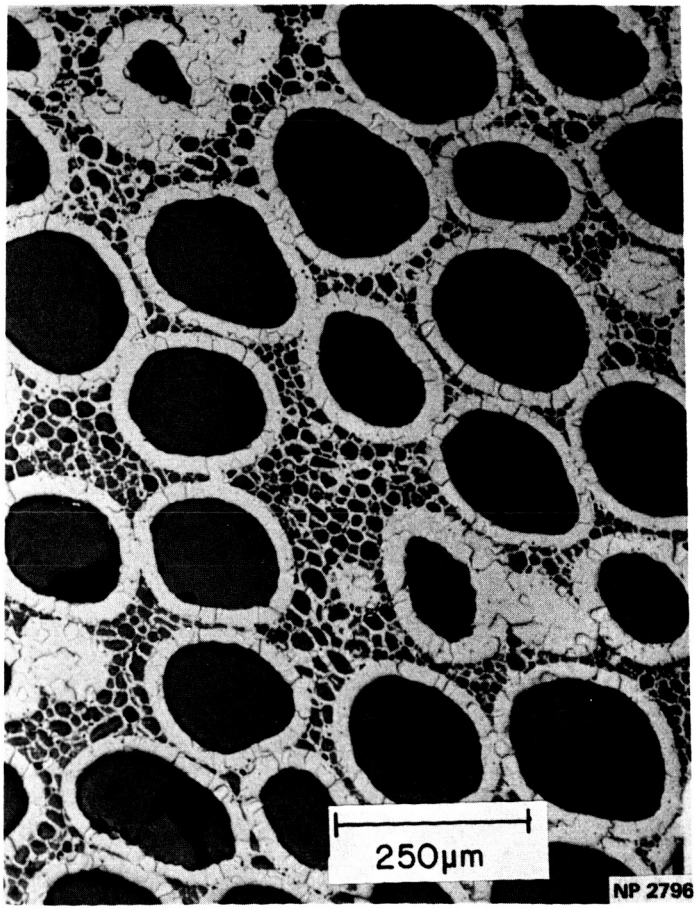

Figure 38. High (95%) Density Cermet Heat Treated at 1800°C for 24 Hours

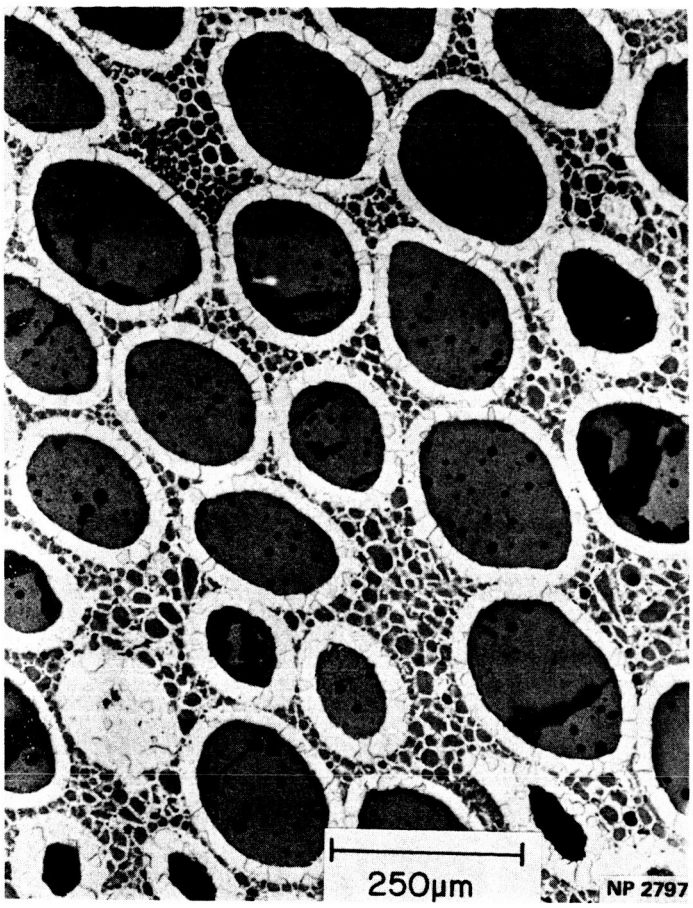

Figure 39. High (95%) Density Cermet Heat Treated at 1900°C for 24 Hours

Figure 40. High (95%) Density Cermet Heat Treated at 1700°C for 24 Hours

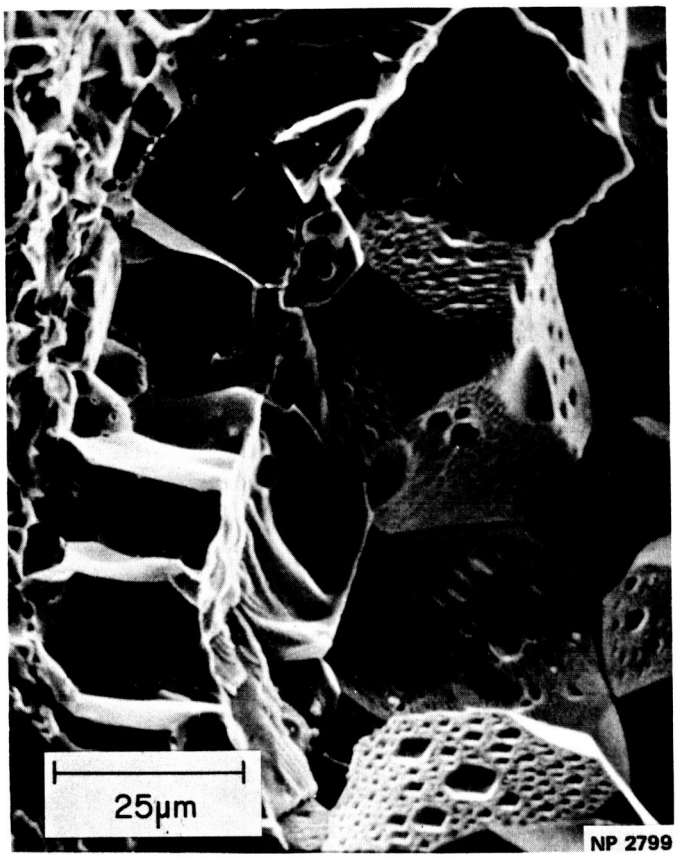

Figure 41. High (95%) Density Cermet Heat Treated at 1800°C for 24 Hours

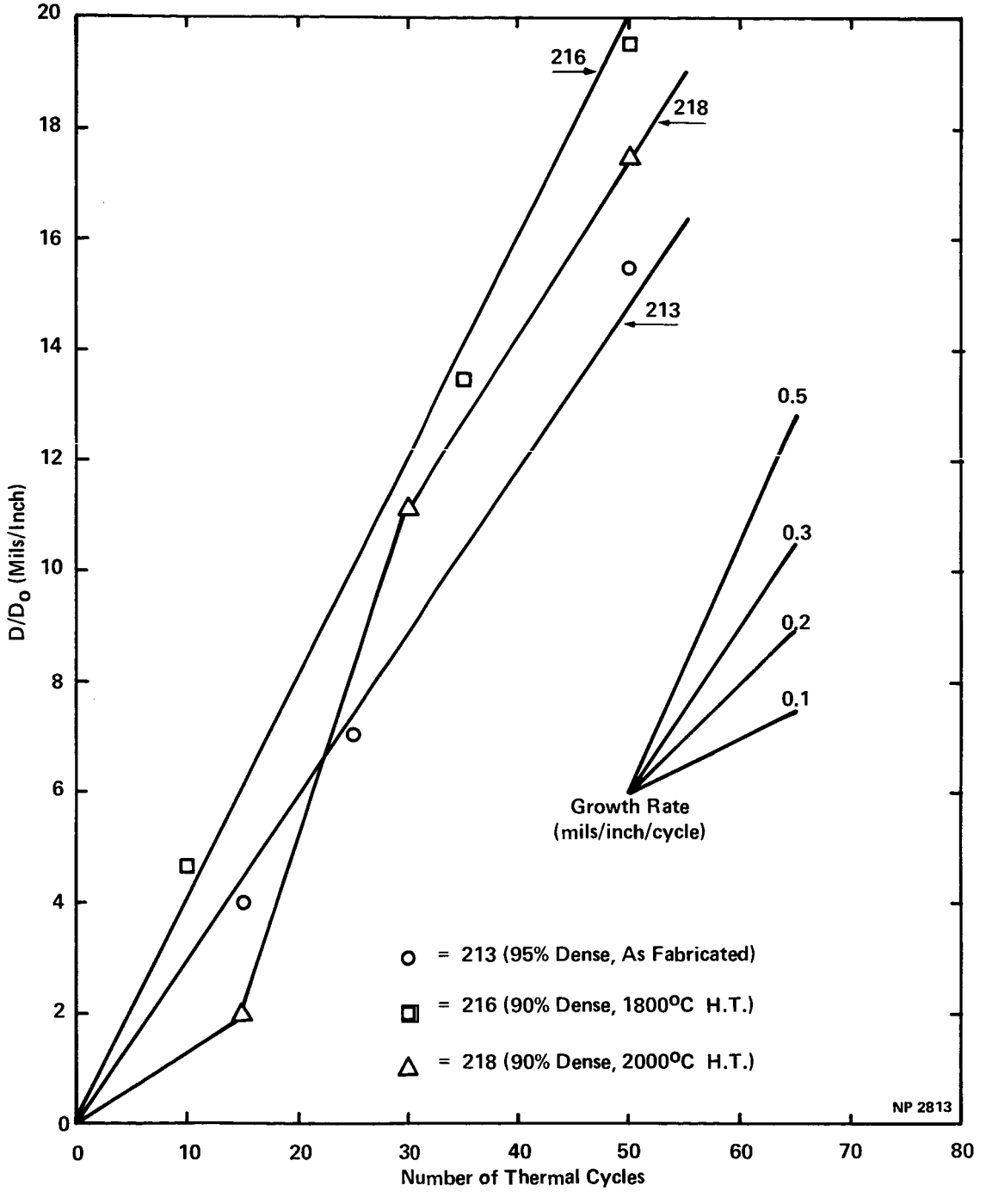

FIGURE 42. DIAMETRAL GROWTH OF CERMETS ON THERMAL CYCLING

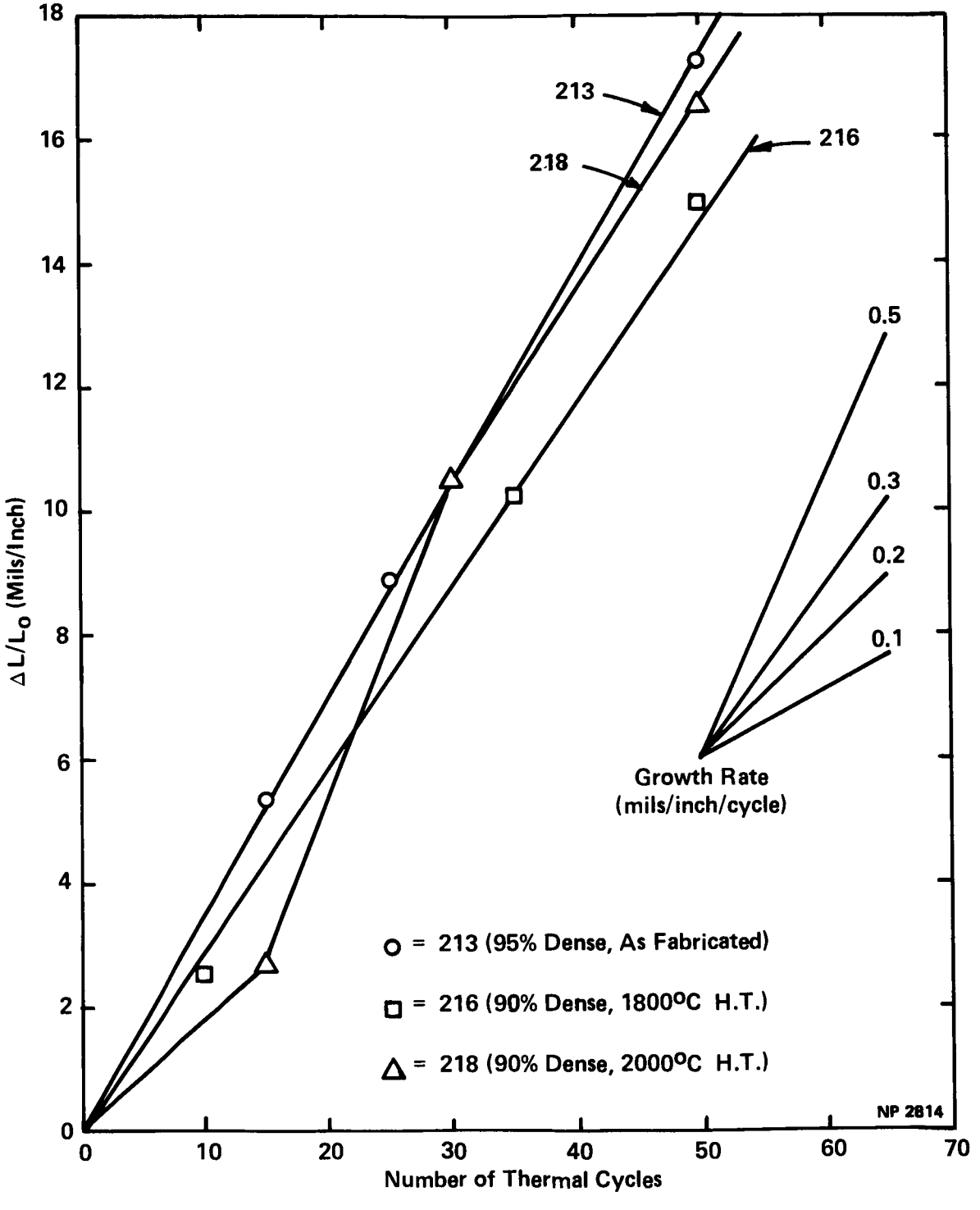

FIGURE 43. CERMET AXIAL DIMENSION CHANGE ON THERMAL CYCLING

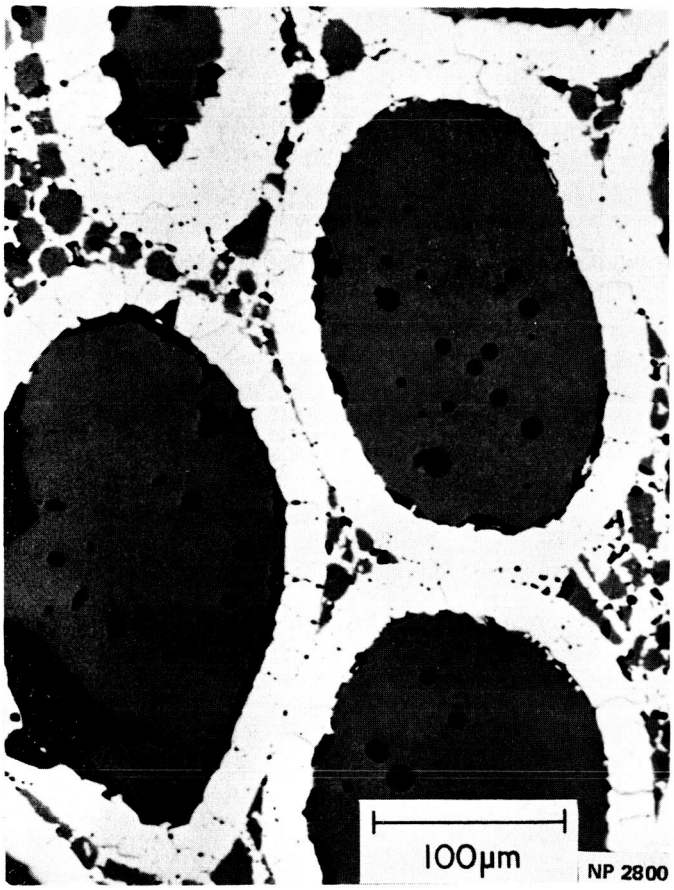

Figure 44. High (95%) Density Cermet After 50 Thermal Cycles (150°C to 1600°C)—Note Link-up of Bubbles on Tungsten Grain Boundaries

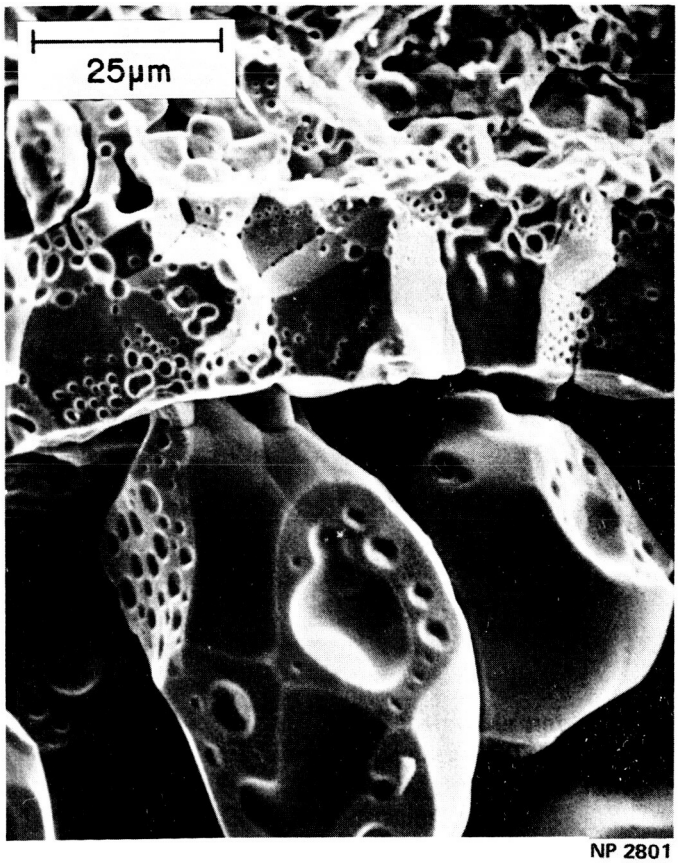

Figure 45. Fracture Surface of High Density (95%) Cermet After 50 Thermal Cycles (150°C to 1600°C)—Note Link-up of Tungsten Grain Boundary Bubbles and Large Grain Boundary Bubbles in UO_2

are in an advanced stage of linking up after 50 thermal cycles as shown in Figures 45 and 46. Note in Figure 44 that there was no apparent penetration of the tungsten grain boundaries by the UO_2 as previously observed in conventional cermet structures.

The structural changes in the low density (90 percent) cermets on thermal cycling were similar to those observed in the high density specimens, with little detectable difference in the microstructures of the specimens heat treated at 1800°C and at 2000°C prior to thermal cycling. The UO_2 in the large particles was separated into a few very dense grains, with almost complete separation at the grain boundaries as shown in Figures 47, 48, and 49. Link-up of the bubbles at the UO_2 surface was also very advanced. The structure of the tungsten was equivalent to that in the thermal-cycled high density specimens.

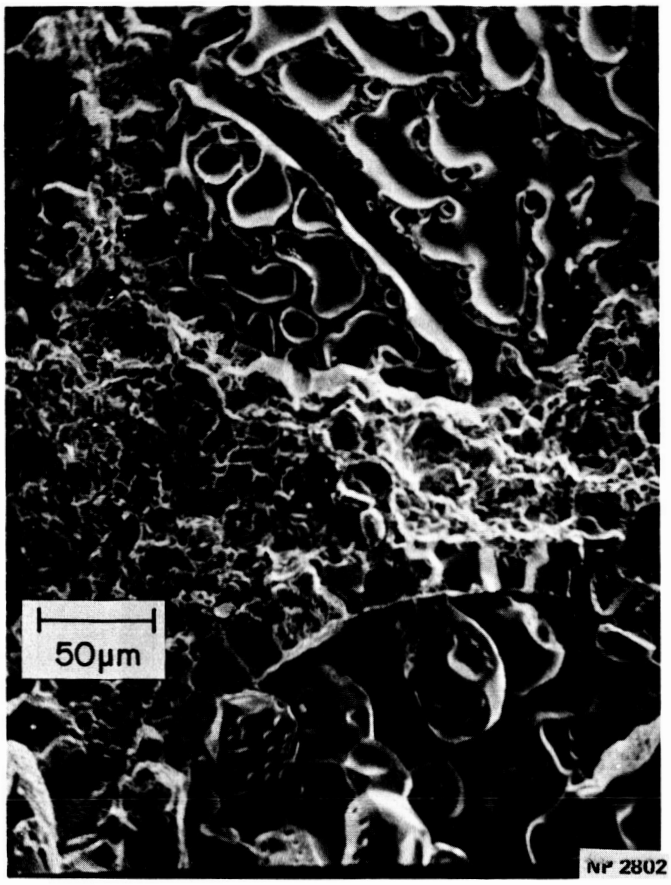

Figure 46. Fracture Surface of High (95%) Density Cermet After 50 Thermal Cycles (150°C to 1600°C)—Note Link-up of Surface and Grain Boundary Bubbles of UO_2 Particles

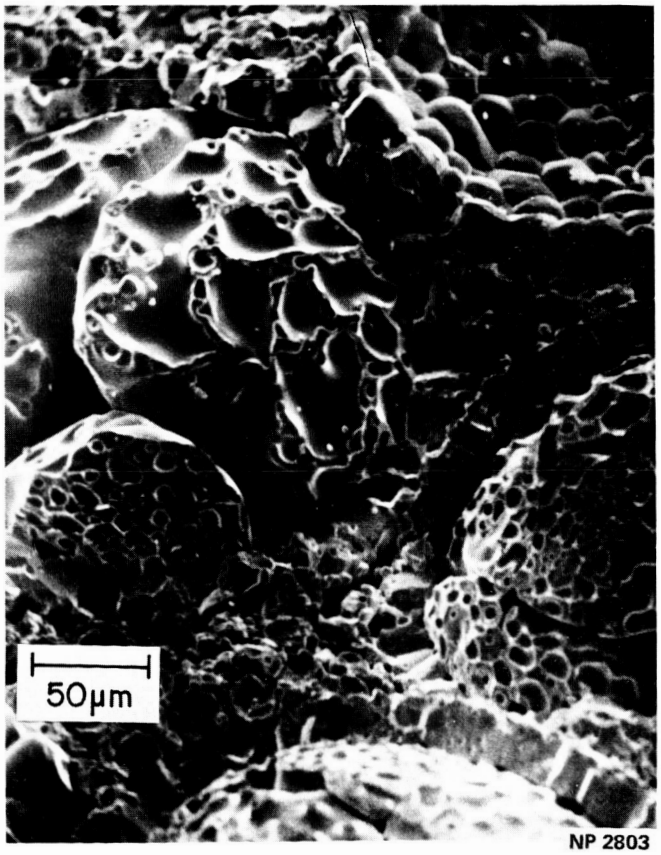

Figure 47. Fracture Surface of Low (90%) Density Cermet After 50 Thermal Cycles – Note Large UO_2 Grains and Link-up of Surface Bubbles

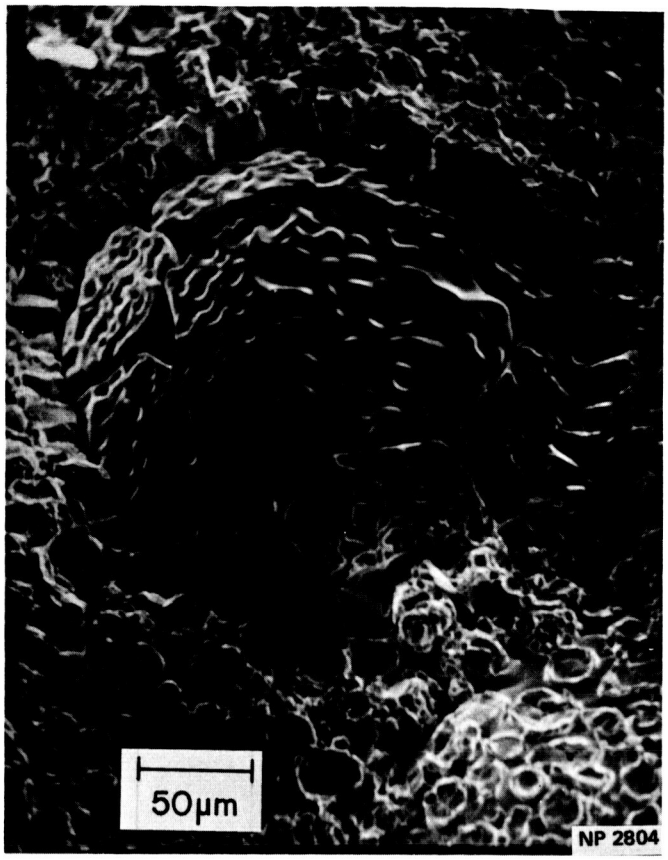

Figure 48. Fracture Surface of Low (90%) Density Cermet After 50 Thermal Cycles – Note Large UO_2 Grains and Link-up of Surface Bubbles

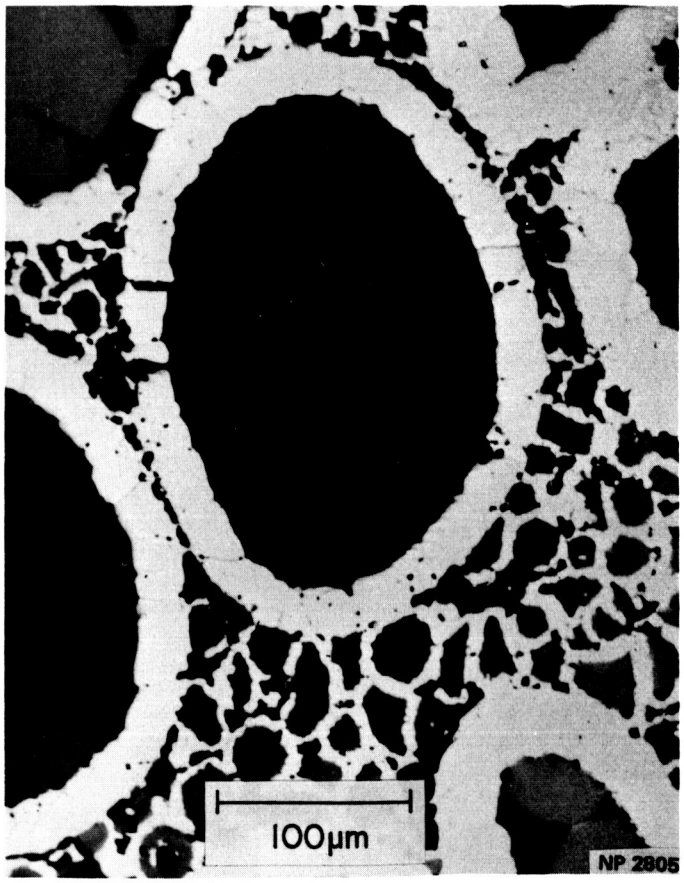

Figure 49. Low (90%) Density Cermet After 50 Thermal Cycles

ANALYSIS AND DISCUSSION OF RESULTS

A. THERMAL EXPANSION

One of the goals of this study was to achieve a thermal expansion of the cermet body approaching that of tungsten. The technique chosen to achieve that goal was the mechanical decoupling of the fuel particles from the tungsten matrix, with incorporation of sufficient void volume at the particle-matrix interface to accommodate the excess thermal expansion of the UO_2 over that of the tungsten; i. e., the "pea-in-a-pod" concept. The degree to which this goal was achieved and the limitations to further decrease in the thermal expansion will now be described.

The thermal expansion of the cermet body should be well described by the relationship given by Lundin[16] which is equivalent[17] to that of Kerner[18] for a composite body of dispersed particles in a continuous phase; i. e.,

$$\alpha = \frac{\dfrac{K_1 V_1 \alpha_1}{3K_1 + 4G_g} + \dfrac{K_2 V_2 \alpha_2}{3K_2 + 4G_g} + \cdots}{\dfrac{K_1 V_1}{3K_1 + 4G_g} + \dfrac{K_2 V_2}{3K_2 + 4G_g} + \cdots}, \qquad (7)$$

where K = bulk modulus, V = volume fraction, G_g = shear modulus of the continuous phase (tungsten matrix), and α = expansion coefficient. Note that this relationship assumes elastic interaction of the particles and the matrix. The expected expansion of the cermets was calculated by equation (7) for four cases, as shown in Figure 50. Three of the cases considered are given below.

(1) The fully dense cermet; i. e., with all of the porosity removed from both the tungsten and the UO_2.

(2) The 95 percent dense cermet; i. e., with all of the porosity removed from the tungsten matrix, but the porosity (ρ UO_2 = 91% -- see Appendix B) retained in the UO_2 with no fuel particle-matrix gap.

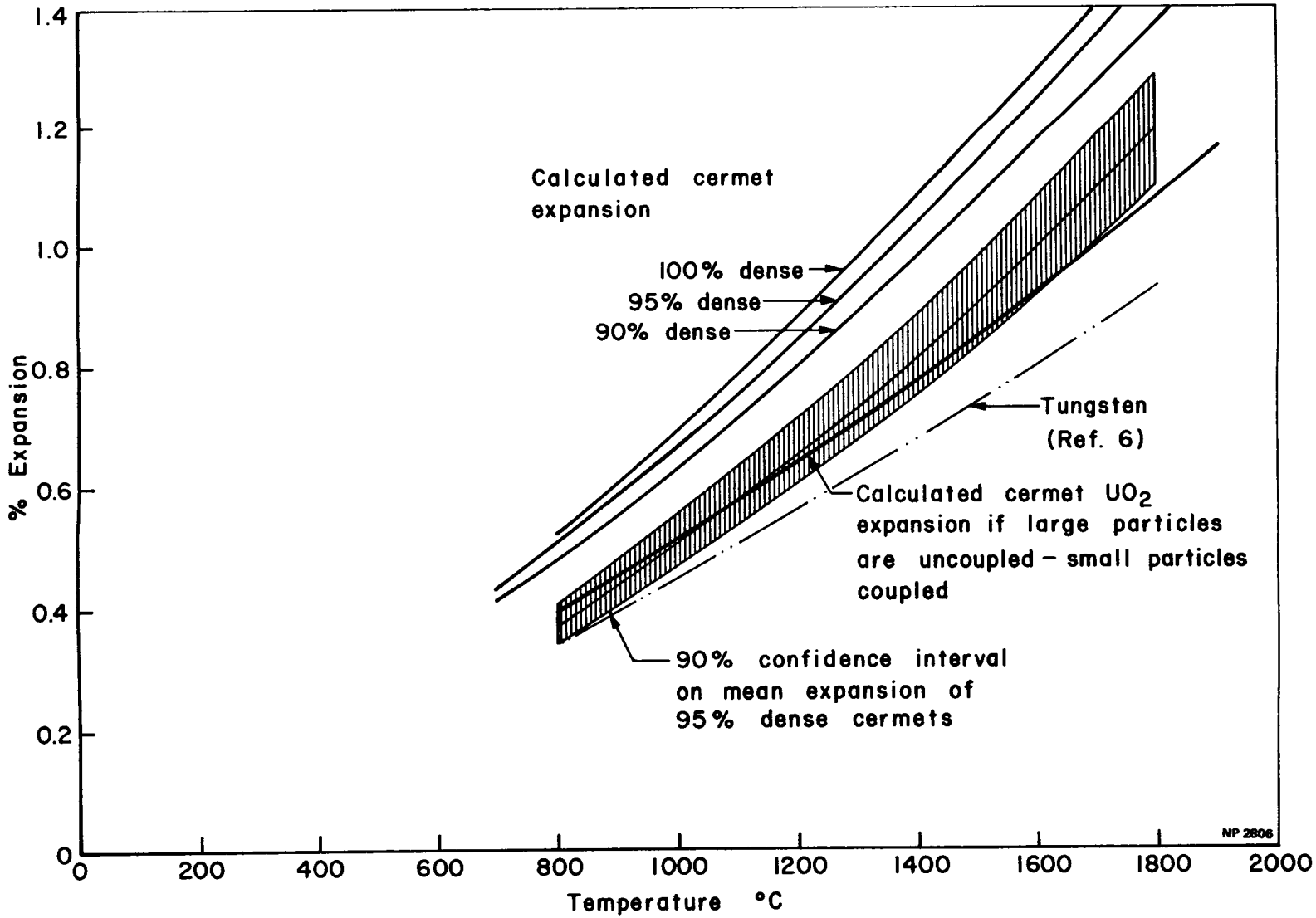

Figure 50. COMPARISON OF CALCULATED AND OBSERVED CERMET THERMAL EXPANSION

(3) The 90 percent dense cermet; i. e., with all of the porosity removed from the tungsten matrix, but the porosity (ρ UO_2 = 82. 6%) retained in the UO_2 with no fuel particle-matrix gap.

By comparison of these calculated expansions with that observed on the 95 and 90 percent dense cermets (Figures 32 and 50) it is apparent that some decoupling of the mechanical fuel particle-matrix system was achieved. The property values used in these calculations are listed in Table 5.

The microstructures of the cermets (e. g., Figures 25, 27, and 36 through 40) suggest that whereas a fuel particle-tungsten matrix gap was achieved at least to some extent for the large particles, there was no such gap achieved for the small particles. Thus, if complete decoupling of the large particles but no decoupling of the small particles was achieved, the expansion of the cermet would be given by equation (7) by assuming that the expansion of the large particles was as if they were all tungsten. To evaluate that case for the composition of the cermets in this study, the volume fraction UO_2 contained in just the small particles (0. 15) was used in equation (7) and is also shown in Figure 50. Note that the expansion calculated for a cermet with completely coupled small particles and completely decoupled large particles falls within the 90 percent confidence interval for the mean expansion of the cermets to approximately 1700°C.

The difference in slope of the calculated expansion and the mean measured expansion of the cermets can be interpreted as evidence of progressive closing of more and more of the fuel particle-tungsten matrix gaps as higher temperatures are achieved.

The thermal expansion results clearly indicate that some mechanical decoupling of the particle-matrix system was achieved. Further, the magnitude of the thermal expansion decrease achieved and the microstructures of the cermets are consistent with a model in which the large particles are essentially completely decoupled and

Table 5. PHYSICAL PROPERTY VALUES FOR EXPANSION CALCULATIONS

	UO_2	Tungsten
Thermal Expansion Coefficient (inch/inch/^oC)	$6.797 \times 10^{-6} + 5.792 \times 10^{-9} T$ (a)	$3.68 \times 10^{-6} + 1.648 \times 10^{-9} T$ (b)
Young's Modulus (psi)	$31.508 \times 10^6 (1 - 1.920P)$ (c) $_x$ $(1 - 1.3716 \times 10^{-4} T - 3.6514 \times 10^{-8} T^2)$ (d)	$58.0 \times 10^6 - 5.83 \times 10^{-3} T$ (e)
Shear Modulus (psi)	$11.902 \times 10^6 (1 - 1.660P)$ (c) $_x$ $(0.9968 - 1.3343 \times 10^{-4} T - 4.006 \times 10^{-8} T^2)$ (d)	(defined by Y and ν)
Poisson's Ratio (ν)	(defined by Y and G above)	0.35^o (f)
Bulk Modulus (psi)	$YG/3(3G - Y)$ (g)	$Y/3 (1 - 2\nu)$ (g)

(a) Reference 5
(b) Reference 6
(c) Reference 19
(d) Reference 20, obtained by fitting extrapolated curve.
(e) Reference 21, obtained by linear approximation of data to 1600^oC.
(f) Reference 22
(g) Reference 23

P = Volume Fraction Porosity
G = Shear Modulus
Y = Young Modulus
T = Temperature, ^oC

the small particles are not at all decoupled. Based on this interpretation of the results, even further decreases in the expansion of the cermet structure could be achieved by some means capable of achieving a particle-matrix gap for the small particles and by increasing the size of the gap in the case of the large particles.

B. MICROSTRUCTURAL CHANGES

The only obvious microstructural changes in the cermets due to heat treatment and thermal cycling was the development of grain boundary bubbles in the tungsten and in the UO_2. It is possible that these bubbles could be responsible for a significant portion of the growth of the cermets. The following is an analysis of the order of magnitude of the dimensional changes to be expected from these microstructural changes.

1. Tungsten

Consider the permanent dimensional changes that would result from the precipitation of grain boundary bubbles as observed in the tungsten matrix (Figures 29, 41, 45, 46, 47, 48 and 49) and the concentration of gas in the matrix that would be required to give such a distribution of bubbles.

Specimen 209 (Figure 41) in the heat treated condition (24 hours at 1800°C) was chosen for analysis to obtain the order of magnitude of the dimensional changes associated with the grain boundary bubbles in the tungsten and the required gas concentration to give such a bubble distribution. This simple model, as shown in Figure 51, was used as a basis for the calculations.

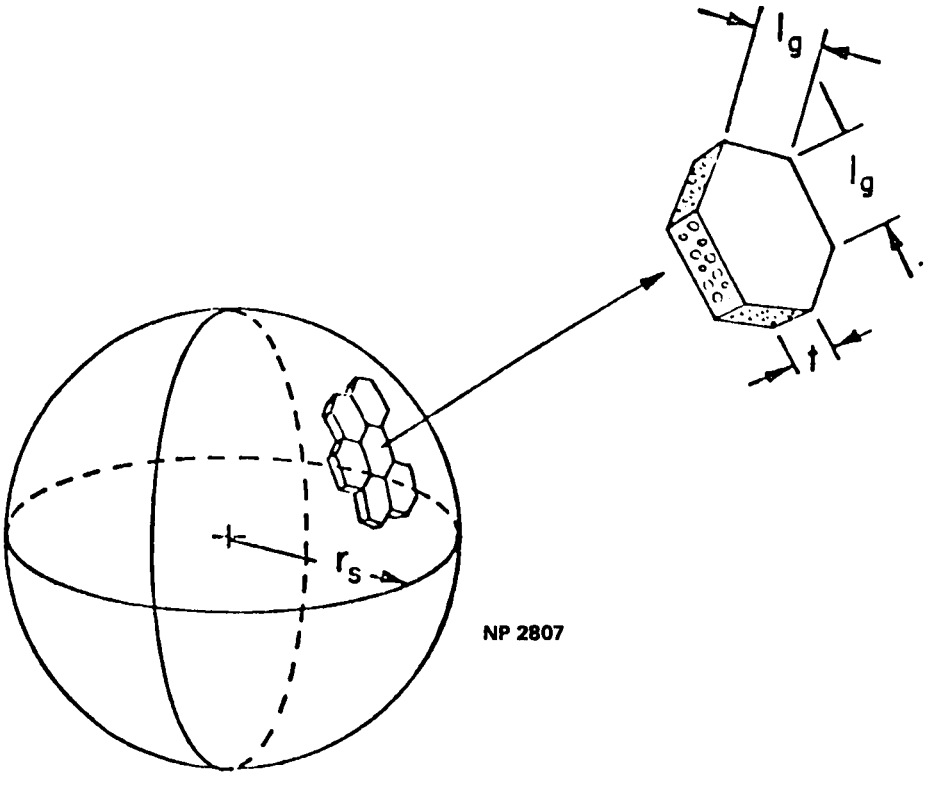

Figure 51. Model for Calculation of Grain Boundary Bubble Swelling and Gas Concentration in Tungsten Matrix

This model assumes that the tungsten shell on the large UO_2 particles is spherical, of radius r_s (r_s = 118 μmm)* that the tungsten shell is only one grain thick (thickness t = 22.0 μ)*, and that the tungsten grains are hexagonal in cross section, with edge lengths ℓ_g (ℓ_g = 15 μm, estimated from the scanning electron micrographs). For such a model, the total radial grain boundary area; i.e., the grain boundary area that could contribute to dimensional changes due to gas trapped during the deposition of the refractory metal shells is given by:

$$\text{Grain Boundary Area per Sphere} = 8\,\pi\, r_s^2\, t/(\sqrt{3}\,\ell_g) \qquad (8)$$

(Note that two grains share a common boundary)

From the photomicrographs, there is obviously a distribution of bubble sizes, and the total volumetric change due to the bubbles is:

$$\Delta V = \sum_{i=o}^{\infty}\left(\frac{\pi}{6}\, N_i d_i^3\right) = \frac{\pi}{6}\sum_{i=o}^{\infty}(N_i d_i^3), \qquad (9)$$

where the i's refer to a given size of bubble. For a distribution of bubble sizes, the volume mean diameter**, $\bar{d}_v$, is given by:

$$\bar{d}_v = \sqrt[3]{\frac{\Sigma N_i d_i^3}{\Sigma N_i}}, \qquad (10)$$

thus, $$\Delta V = \frac{\pi}{6}\,\bar{d}_v^{\,3}\,(\Sigma N_i). \qquad (11)$$

---

* Calculated assuming a uniform 16% reduction in volume due to pressing 250μm diameter particles from 80% to 95% density and 54 volume percent UO_2 in the final particle.

** The volume mean diameter is that value of diameter which then cubed and multiplied by the appropriate geometric constant (π/6) gives the mean volume of a bubble in the distribution.

The total number of bubbles, ΣN_i, is equal to the measurable bubble concentration per unit grain boundary area times the grain boundary area; i. e.,

$$\Sigma N_i = N_B \text{ bubbles/cm}^2 \times 8\pi r_s^2 \, t/(\sqrt{3}\,\ell_g), \tag{12}$$

and hence,

$$\Delta V = \frac{\pi \bar{d}_v^3 \, N_B \, 8\pi r_s^2 \, t}{6\sqrt{3}\,\ell_g}, \tag{13}$$

and

$$\frac{\Delta V}{V} = \frac{\pi N_B \, \bar{d}_v^3 \, t}{\sqrt{3}\,\ell_g \, r_s} . \tag{14}$$

The concentration of gas atoms required to give the observed bubble distribution can be estimated as follows. If the bubbles are spherical and no hydrostatic stresses exist, the pressure in a given bubble, P_i, is given by:

$$P_i = \frac{2\gamma}{r_i} , \tag{15}$$

where γ is the surface energy of the matrix metal.

If the gas is ideal, then the number of moles of gas in a given bubble, at the heat treatment temperature T (^{o}K) is:

$$n_i = \frac{2\pi\gamma \, d_i^2}{3RT} , \tag{16}$$

where R is the gas constant, (8.31×10^7 erg/^{o}K mole).

As above, the total number of moles of gas, n_T, is then given by:

$$n_T = \frac{2\pi\gamma \sum_{i=o}^{\infty} (N_i d_i^2)}{3RT} . \tag{17}$$

The surface area mean diameter*, $\bar{d}_s$, is defined by the relationship:

$$\bar{d}_s = \sqrt{\frac{\Sigma (N_i d_i)^2}{\Sigma N_i}} \text{ ; thus,} \tag{18}$$

$$n_T = \frac{2 \pi \gamma \bar{d}_s^2 (\Sigma N_i)}{3 R T} , \tag{19}$$

and since $\Sigma N_i = N_B$ bubbles/cm^2 of grain boundary area times the total grain boundary area, the total number of moles of gas in bubbles on a sphere is n_T, where

$$n_T = \frac{16 \pi^2 \gamma \bar{d}_s^2 N_B r_s^2 t}{3\sqrt{3} R T \ell_g} . \tag{20}$$

The concentration of gas [G] is readily obtained from:

$$[G] = \frac{n_T M}{4 \pi r_s^2 t \rho} \quad \left(\frac{\text{moles of gas}}{\text{moles of W}}\right) , \tag{21}$$

where M is the molecular weight of the matrix metal and ρ is its density.

The photomicrographs of Specimen 209 were analyzed to determine the distribution of bubble sizes; only bubbles on grain surfaces were analyzed, not those at corners or on edges. The results are shown on a log-probability plot in Figure 52.

The surface mean diameter, $\bar{d}_s$, and the volume mean diameter, $\bar{d}_v$, were computed from the observed geometric mean diameter on a

*The surface area mean diameter is that value of diameter which when squared and multiplied by the appropriate geometric constant (π) gives the mean surface area in the distribution.

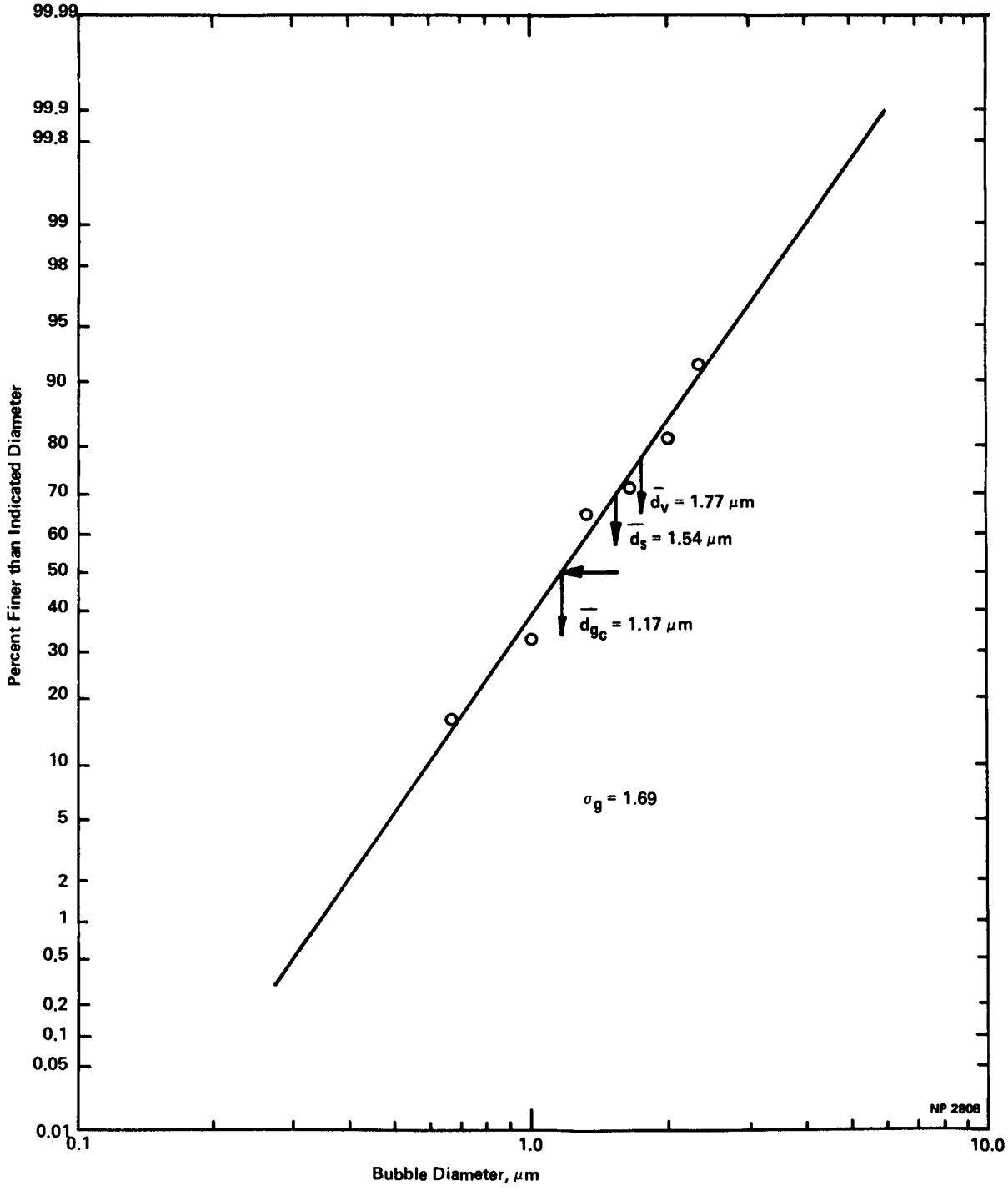

FIGURE 52. GRAIN BOUNDARY GAS BUBBLE SIZE DISTRIBUTION

counting basis $\bar{d}_{g_c}$ (50% size) and the geometric standard deviation, σ_g (84.13% size/50% size), by the relations as given by Orr.[24]

$$\log \bar{d}_s = \log \bar{d}_{g_c} + 2.3026 \log^2 \sigma_g \text{ , and} \tag{22}$$

$$\log \bar{d}_v = \log \bar{d}_{g_c} + 3.4539 \log^2 \sigma_g. \tag{23}$$

The following values were found to describe the bubble distribution:

$\bar{d}_{g_c} = 1.17\ \mu m,$
$\sigma_g = 1.69\ \mu m,$
$\bar{d}_s = 1.54\ \mu m,$ and
$\bar{d}_v = 1.77\ \mu m.$

The volumetric dimensional change corresponding to the estimated bubble concentration ($4.5 \times 10^6/cm^2$ of grain boundary area)as given by equation (14) is:

$$\frac{\Delta V}{V} = 0.54\%,$$

or the linear dimensional change is estimated to be:

$$\frac{\Delta L}{L} = \frac{\Delta r}{r} = \frac{1}{3} \frac{\Delta V}{V} = 0.18\% = 1.8 \text{ mils/inch.}$$

The number of moles of gas in the tungsten shell required to produce the observed bubble distribution assuming equilibrium at 1800°C, the heat treatment temperature for specimen 209, and 1000 erg/cm^2 as the surface energy of tungsten is (equation 20):

$$n_T = 3.9 \times 10^{-12} \text{ mole.}$$

The calculated concentration of gas in the tungsten matrix, as given by equation (21) is:

$$[G] = 9.7 \times 10^{-6} = 9.7 \text{ ppm (mole basis).}$$

If the gas giving rise to the bubbles is due to the halide impurities and the weight ratio of these elements is approximately 4Cl/1F, as indicated by the chemical analysis, the observed bubble distribution requires only ~0.6 ppm F and 2.6 ppm Cl on a weight basis if the halides are present as gases containing two atoms of halide per molecule--e.g., WF_2 and WCl_2 or F_2 and Cl_2. The required halide impurity content is directly proportional to the number of halide atoms per gas molecule--e.g., if WF_6 and WCl_6, the impurity level indicated is approximately 1.8 ppm F and 7.8 ppm Cl.

2. $\underline{UO_2}$

Consider the process of chemical vapor deposition of tungsten by thermochemical reduction of the hexachloride on porous (~70% dense) UO_2 particles. Possible deposition reactions include:

		Chlorine Content per Mole of Product Gas (Moles Cl/mole product gas)	
WCl_6 (g) + 3 H_2 (g)	= W(s) + 6HCl (g)	1	
(4 moles of gas)	= (6 moles of gas)		(24)
$2WCl_6$ (g) + $5H_2$ (g)	= W(s) + WCl_2(g) + 10HCl(g)	12/11 = 1.09	
(7 moles of gas)	(11 moles of gas)		(25)
$2WCl_6$ (g) + $4H_2$(g)	= W(s) + WCl_4 (g) + 8HCl(g)	12/9 = 1.33	
(6 moles of gas)	= (9 moles of gas)		(26)
$4WCl_6$ (g) + $7H_2$(g)	= W(s) + $2WCl_5$(g) + 14Cl(g)	24/16 = 1.50	
(11 moles of gas)	= (16 moles of gas)		(27)

Note that the deposition reaction in all cases results in more gaseous products than reactants (approximately by 1.5). Thus, as a conservative minimum, it can be assumed that there is no change in the gas content (moles) of the pores in fuel particles during the deposition process.

As the tungsten is deposited on the porous particles, it will rapidly develop an impervious layer at the particle surface effectively trapping any gas contained in the porous UO_2 particles. If the particles are spherical and the pores are open (connected to the surface as would be expected for fuel densities less than 95% of theoretical), the number of moles of gas trapped in a porous particle n_{T_p}--assuming ideal gas behavior--is:

$$n_{T_p} = \frac{4\pi r^3(1-\rho_f)P}{3RT} \quad ; \tag{28}$$

where P is the deposition pressure (~1 atmosphere), or 1×10^6 dyne/cm^2,

r is the particle radius,

R is the gas constant,

T is the absolute deposition temperature (~1200°K for the chloride process, and

ρ_f is the fraction of theoretical density of the fuel particles (e. g. , 0. 7).

If the porous particles are approximately 200 μm in diameter, equation (28) gives a total gas content in the particle pores of:

$$n_{T_p} = 1.28 \times 10^{-11} \text{ moles.}$$

Assuming the gas to be all product gas from the above listed reactions (equations 24 through 27), the chlorine content of the fuel particles due to the trapped gas would be in the range of 14. 2 to 21. 3 ppm by weight depending on the state of reduction of the tungsten chloride. Note that this is approximately half the observed chlorine impurity level.

The structure of the particles with respect to the distribution of the trapped gas should be considered at three stages in the history of the cermets: (a) initially, just after coating with tungsten; (b) in an intermediate stage after densification by hot pressing; and (c) after heat treatment to an end-point equilibrium condition when the gas is completely agglomerated.

(a) As Coated

In the coated condition, the pore or bubble structure will be unaffected by the presence of the gas; thus, from microstructural observations of porous UO_2, we expect that the pores will be approximately 1 μm in diameter and the amount of gas in each pore is given by the ideal gas law. The amount of gas in each 1 μm diameter pore for a deposition pressure of 1 atmosphere at 1200°K is 5.3×10^{-18} moles of gas per pore and the total estimated number of 1 μm diameter pores or bubbles per particle is 2.4×10^{6} (1.28×10^{-11} moles per particle per 5.3×10^{-18} moles per pore).

(b) Intermediate Stage

The as hot-pressed condition of the fuel particle microstructure can be approximated by assuming that the number of pores or bubbles does not change drastically during the short hot pressing time, and only their size changes due to the pressure and surface energy forces during the hot-pressing process. Neglecting for the moment the external pressure and considering only the surface energy restraint, the equilibrium pressure in the bubbles, P, is given by the relations:

$$P = \frac{2\gamma}{r_i} \quad \text{and} \quad = \frac{n_i RT}{V_i} \tag{29}$$

where γ is the surface energy of the fuel,
r_i is the radius of an individual bubble,
V_i is the volume of a bubble, and
n_i is the number of moles of gas contained in the bubble.

Combining terms in equation (29) gives the following relationship for the equilibrium bubble size (assuming no change in the number of pores):

$$r_i = \left(\frac{3n_i RT}{8\pi\gamma}\right)^{1/2}, \tag{30}$$

which when evaluated at the hot-pressing conditions (T is $\sim 2000^{\circ}K$ and assuming that $\gamma_{UO_2} = 1000$ erg/cm^2) gives a value of the pore radius of $r_i \approx 0.1$ μm. Note that this size is well below the detection limits by standard metallographic techniques. The additional restraint due to the pressing pressure only serve to further reduce the calculated size of the bubbles at this stage in the development of the cermet microstructure.

(c) End-Point Heat Treated Condition

Heat treatment of the fuel structure described above--i. e., minute unobservable bubbles distributed throughout the fuel--is expected to result in agglomeration of the gas through diffusional processes, either by atomistic diffusion or migration and collisional coalescence of the bubbles as entities. The bubbles will become pinned on grain boundaries with subsequent release of the trapped gas by diffusion along the grain boundaries or by two dimensional diffusion of the bubbles along the grain boundaries, or by more or less complete deterioration of the grain boundaries by link-up of adjacent bubbles. Thus, the expected equilibrium end-point condition is reached when all of the gas is released from the fuel particles to the fuel particle-tungsten shell gap or interface. Because of the much larger radius of curvature of the bubble when the gas occupies the fuel particle-tungsten matrix gap--i. e., ~200 μm diameter--the external pressure restraint forces cannot be neglected in determining the equilibrium volume occupied by the released gas. Thus, in this case, the gas pressure P_W in the tungsten shell when the gas is completely released to the gap is given by:

$$P_W = \frac{2\gamma_W}{r_W} + P_H, \tag{31}$$

where γ_W is the surface energy of the tungsten (assumed to be approximately 1000 erg/cm^2 as before),

r_W is the equilibrium inside radius of the tungsten shell, and

P_H is the external pressure acting on the tungsten shell.

Again assuming ideal behavior of the gas and that the fuel behaves as a spherical "pea-in-a-pod", the following relationship is obtained:

$$r_W^4 + \frac{2\gamma_W r_W^3}{P_H} - \left(r_F^3 + \frac{3nT_p RT}{4\pi P_H} \right) r_W - \frac{2\gamma_W r_F^3}{P_H} = 0, \qquad (32)$$

where r_F is the radius of the fully dense fuel particle, and

n_{T_p} is the total number of moles of gas trapped in the tungsten shell as before.

Note that the radius of the fully dense fuel particle, r_F, is determined from the initial fuel particle density, ρ_f, and its initial radius, r_o, by the relationship:

$$r_F = (\rho_f r_o^3)^{1/3}. \qquad (33)$$

Substituting the proper values in equations 32 and 33, assuming an initial fuel particle radius of 100 μm and an initial fuel density of 70% of theoretical, the equilibrium inside radius of the tungsten shell surrounding the fuel particle when the external pressure on the system is 1 atmosphere at 1900°K (approximately the thermal cycling maximum temperature) is r_W = 103.3 μm. Thus, at the final end-point configuration with all of the gas in the fuel particle-matrix gap and with the UO_2 completely densified, we expect a linear dimensional increase of 3.3% or 33 mils per inch at 1900°K. Note that this is considerably (~X2) in excess of the dimensional change observed after 50 cycles to 1600°C (~1900°K). It appears that all of the dimensional changes occurring in the cermets during heat treatment and thermal cycling could be accounted for by the redistribution of the gas trapped in the porous UO_2 particles during the deposition of the tungsten coating. If this is indeed a large contribution to the dimensional instability of the cermets as the microstructures indicate, only by eliminating the incorporation of gas can the dimensional stability be improved. A technique for coating the particles that does not inherently trap gas in the porous fuel particles as by powder

metallurgy, or a technique for making the porosity unavailable to the gas by forming an impervious skin on the UO_2 particles as by dropping them through a plasma should thus be possible routes to improved dimensional stability in the cermet concept developed here.

CONCLUSIONS

Based on the results of this study, the following conclusions have been drawn.

FABRICATION OF CERMETS

Uniform cermet pellets were fabricated by loading nominally 200 μm tungsten-coated porous UO_2 particles in a graphite die, followed by filling of the interstices between the 200 μm particles with similar particles with a nominal diameter of 20 μm. The as-loaded packing density in the graphite dies was approximately 80%. The pellets were compacted to 90 and 95% of theoretical density by hot pressing in the graphite dies at 1700°C with 4000 and 6000 psi applied pressure. The fully dense UO_2 loading of the cermets was 53 volume percent.

THERMAL EXPANSION

The thermal expansion behavior of the cermets is given by the following relations:

(a) For the 95% dense cermets:

$$\frac{\% \Delta L}{L} = (3.424 \pm 0.291) \times 10^{-4} (T-25) + (1.865 \pm 0.139) \times 10^{-7} (T-25)^2$$

(b) For the 90% dense cermets:

$$\frac{\% \Delta L}{L} = (4.227 \pm 0.301) \times 10^{-4} (T-25) + (1.313 \pm 0.282) \times 10^{-7} (T-25)^2$$

Heat treatment of the cermets for 24 hours in the range of 1700 to 2000°C did not significantly alter the thermal expansion behavior of the cermets based on the few specimens tested. This measured expansion is significantly below that for conventional cermets made from

single-size, coated particles of approximately the same composition and below that calculated for this structure assuming elastic interaction of the dispersed UO_2 phase in the tungsten matrix. These observations indicate that some mechanical decoupling of the UO_2 and the tungsten was achieved through incorporation of sufficient void volume to accommodate excess thermal expansion of the UO_2 over that of the tungsten matrix.

THERMAL CYCLING BEHAVIOR

Thermal cycling of the cermets from 150 to 1600°C produced monotonic and isotropic growth in the cermets at a rate of 0.30 to 0.39 mils per inch per cycle. This measured growth is approximately twice as great as that observed on cermets of a similar composition formed of monodisperse, tungsten-coated, dense UO_2 particles. The microstructure of the fuel particles and the tungsten indicate an agglomeration of trapped impurity gases in the porous UO_2 particles and in the thermochemically deposited tungsten. Analysis of the amount of growth to be expected from the gas trapped in the porous UO_2 during the thermochemical deposition of the tungsten coating showed that all of the growth of the cermets could be accounted for by the volume change accompanying the agglomeration of the gas.

APPENDIX A

THEORETICAL DENSITY OF CERMETS

The overall weight fraction of tungsten in the cermets is the weight fraction of tungsten in the small particles times their weight fractions in the cermet blend plus the weight fraction of tungsten in the large particles times their weight fraction in the cermet blend--i. e. ,

$$F_W = (f_{W_s})(F_s) + (f_{W_L})(F_L) , \qquad (A1)$$

where F_W is the overall weight fraction tungsten in the cermet body, F_s is the weight fraction of small particles in the cermet, F_L is the weight fraction of large particles in the cermet, f_{W_s} is the weight fraction of tungsten in the small particles, and f_{W_L} is the weight fraction of tungsten in the large particles.

The theoretical density of the cermet bodies is achieved when both the tungsten and UO_2 are fully dense and no porosity remains in the structure. Under those conditions, the specific volume of the tungsten and UO_2 are:

V_W = specific volume of W = 1/19. 3 = 0. 05181 cm^3/gm, and
V_{UO_2} = specific volume of UO_2 = 1/10. 96 = 0. 09124 cm^3/gm.

The volume per unit mass occupied by the tungsten or the UO_2 in the theoretically dense cermet is the weight fraction of the particular component times its specific volume and, thus, the specific volume of the cermet, V_C, is given by:

$$V_C = (F_W)(V_W) + (1-F_W)(V_{UO_2}) \qquad (A2)$$

and the theoretical density of the cermet ρ_{Th} is the reciprocal of the specific volume--i. e. ,

$$\rho_{Th} = 1/V_C = \frac{1}{(F_W)(V_W) + (1-F_W)(V_{UO_2})} . \qquad (A3)$$

Substituting the weight fractions of tungsten for the small and large particles obtained by chemical analysis (Table 1) and the predetermined weight fractions of the two particles (23.6 weight percent of the small, 76.4 weight percent of the large) and the stated values for the specific volumes of the tungsten and UO_2 in the above relation gives a value of 14.9174 gm/cm^3 for the theoretical density of the cermets fabricated in this study.

The volume fraction of fuel in the theoretically dense cermet, $F_{V_{UO_2}}$, is given by the ratio of the volume occupied by the UO_2 to the total volume per unit mass--i.e.,

$$F_{V_{UO_2}} = \frac{(1-F_W)V_{UO_2}}{(F_W V_W) + (1-F_W)V_{UO_2}} . \qquad (A4)$$

With the above mentioned values, equation (A4) gives 0.526 for the volume fraction of UO_2 in the fuel if it is theoretically dense.

Assuming that all of the porosity in a cermet that is less than fully dense is associated with the UO_2--i.e., its density is Y(10.96) and the overall cermet density is $X(\rho_{Th})$, where X and Y are the fractional densities of the cermet and the UO_2, respectively--the relation between the cermet fractional density and the fractional density of the UO_2 is, from equation (A3), as follows:

$$X(\rho_{Th}) = \frac{1}{(F_W V_W) + (1-F_W)(1/Y)(V_{UO_2})} ; \qquad (A5)$$

or solving for Y, the fractional density of the porous UO_2 is,

$$Y = \frac{(1-F_W)V_{UO_2}}{\left(\frac{1}{X\rho_{Th}} - F_W V_W\right)} . \qquad (A6)$$

This relationship is shown in Figure (A1) for the conditions stated above.

Another interpretation of the relationship shown in Figure A1 (equation A6) for the case of a fuel-particle, matrix-shell gap is that Y is the fraction of the volume in the tungsten shells that is filled with fully dense UO_2. Thus, for a 95% dense cermet with the porosity removed from the interstices between the particles, the UO_2 would be 91% dense if the porosity was uniformly distributed, or it would occupy only 91% of the available volume in the surrounding spherical shell of tungsten if the UO_2 were fully dense.

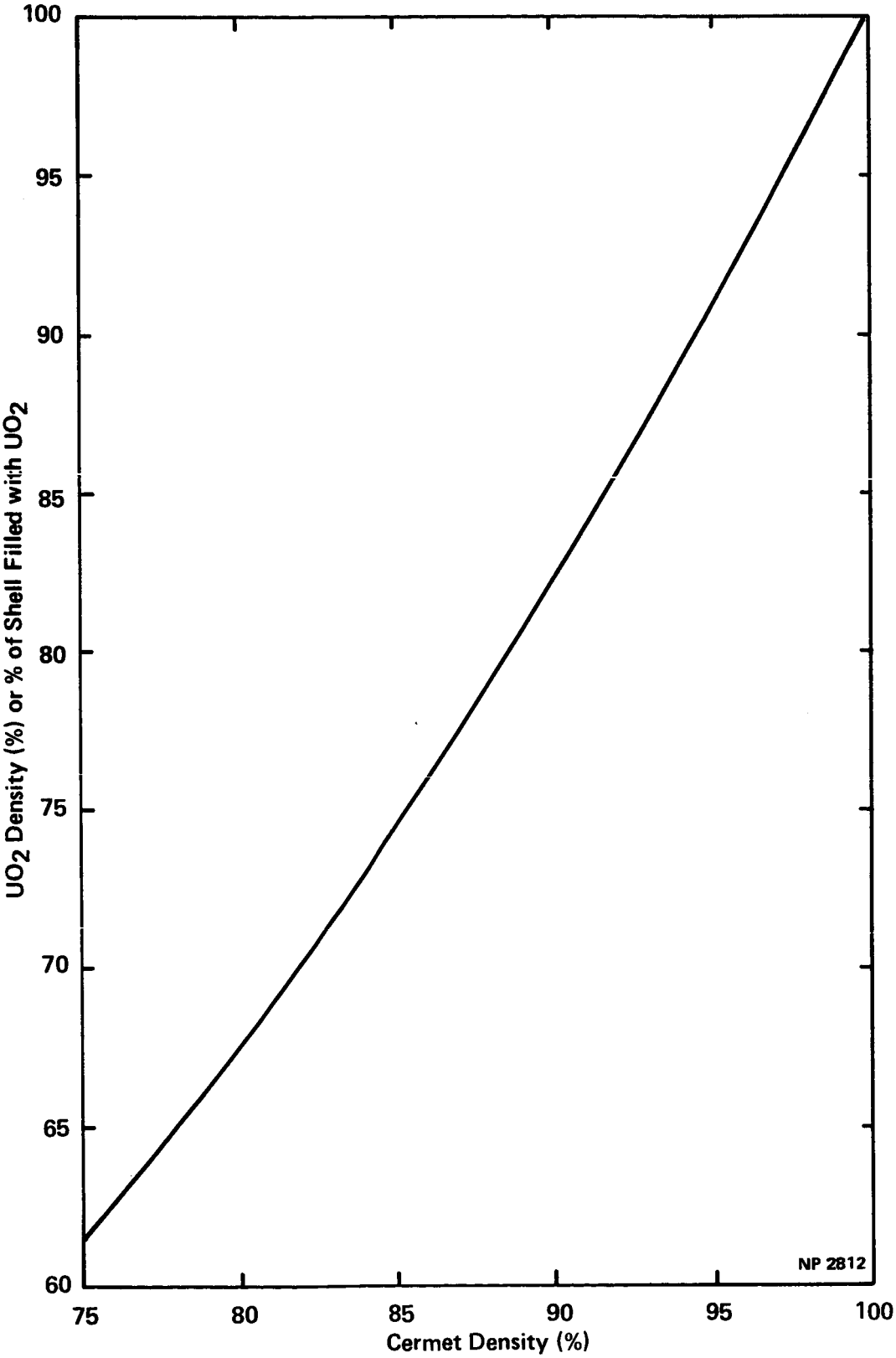

FIGURE A1. RELATIONSHIP OF UO_2 AND CERMET DENSITIES

APPENDIX B

ACCURACY OF PERMANENT DIMENSIONAL CHANGE MEASUREMENTS

The permanent dimensional changes per unit length, Δ, were calculated as follows:

$$\Delta = \frac{L_2 - L_1}{L_1} \tag{B1}$$

where L_1 and L_2 are the measured values of the dimension of interest before and after the treatment being considered, respectively. Since Δ is a function of L_1 and L_2 only, differentiating (1) we have:

$$d\Delta = \left(\frac{\partial \Delta}{\partial L_1}\right) dL_1 + \left(\frac{\partial \Delta}{\partial L_2}\right) dL_2 \tag{B2}$$

Considering the differentials as the random errors, ϵi, gives:

$$\epsilon_\Delta^2 = \left(\frac{\partial \Delta}{\partial L_1}\right)^2 \epsilon_{L_1}^2 + \left(\frac{\partial \Delta}{\partial L_2}\right)^2 \epsilon_{L_2}^2 \tag{B3}$$

Substituting the appropriate partial derivatives from equation (1) and dividing through by Δ^2 to a place on a fractional basis gives:

$$\frac{\epsilon \Delta}{\Delta} = \sqrt{\frac{L_2^2 \epsilon_{L_1}^2 + L_1^2 \epsilon_{L_2}^2}{L_1^2 (L_2 - L_1)^2}} \tag{B4}$$

and since $\epsilon_{L_1} = \epsilon_{L_2} = \epsilon_L$ (≥ 0.0001 inch), and $L_1 \simeq L_2$ for small dimensional changes, we can make the approximation:

$$\frac{\epsilon_\Delta}{\Delta} = \sqrt{\frac{2\epsilon_L^2}{(L_2 - L_1)^2}} \quad , \text{ or} \tag{B5}$$

$$\epsilon_\Delta = \frac{(L_2 - L_1)}{L_1} \frac{\sqrt{2\epsilon_L^2}}{(L_2 - L_1)} = \frac{\sqrt{2\epsilon_L^2}}{L_1} \tag{B6}$$

For cermet specimens with lengths of ~0.9 inch and diameters of ~0.4 inch, this gives:

$$\epsilon_{\text{Length}} = \frac{\sqrt{2 \times (10^{-4})^2}}{0.9} = \sim 0.00016 \text{ inch or } \sim 0.2 \text{ mil/inch}$$

$$\epsilon_{\text{Diameter}} = \frac{\sqrt{2 \times (10^{-4})^2}}{0.4} \simeq 0.00035 \text{ inch or } \sim 0.4 \text{ mil/inch.}$$

Thus, the maximum expected accuracy of permanent length changes is $\pm$ 0.2 mils/inch and for diameter changes is $\pm$ 0.4 mils/inch.

It is important that these probable error bands on the dimensional changes be considered, especially when comparing one specimen's performance or behavior with that of another.

REFERENCES

(1) Marlowe, M. O., Ekvall, R. A., and Kaznoff, A. I., "Development and Evaluation of UO_2-W Cermet Fuel for Nuclear Thermionic Emitters," NASA/LeRC by General Electric Company, July 15, 1967 (NASA CR-72274, GEST 2102), Confidential.

(2) Amato, I., Colombo, R. L., and Polin, F., "The Dependence on Microstructure of the High Temperature Properties of Uranium Oxide, Molybdenum and Uranium Oxide, Tungsten Cermets," Rev. Hautes Temper. et Refract. 3, 289-296.

(3) Ogawa, S. Y., "Irradiation Performance Test of UO_2-Cermet Fuel," General Electric Company, March 1964, (GEAP-4435).

(4) Chapman, Alan T., Clark, G. W., and Hendrix, D. E., "UO_2-W Cermets Produced by Unidirectional Solidification," presented at American Ceramic Society Annual Meeting, May 1969, Washington, D. C.

(5) Conway, J. B., Fincel, R. M. Jr., and Hein, R. A., "The Thermal Expansion and Heat Capacity of UO_2 to 2200°C," presented at American Nuclear Society Meeting, June 1963, Salt Lake City, Utah.

(6) Conway, J. B., "High-Temperature Materials Program Progress Report No. 63," General Electric Company, December 30, 1966 (GEMP-63).

(7) Yario, W. R., "Dimensional Stability of Refractory Metal Fuel Elements Under Thermal Cycling Conditions," General Electric Company, 1966 (GE-TM66-4-17) (Confidential).

(8) Smith, R. A., Speidel, E. O., and Kizer, D. E., "Factors Controlling the Growth of Cermets During Thermal Cycling," Battelle Memorial Institute, February 19, 1968 (BMI-1824).

(9) "Development of a Nuclear Thermionic Fuel Element," General Electric Company, 1966 (GE-SR-2079).

(10) "Development of a Nuclear Thermionic Fuel Element," General Electric Company, 1966 (GE-SR-2089).

(11) Smith, R. A., Kizer, D. E., Speidel, E. O., and Keller, D. E., "Phase Equilibria in the Uranium-Tungsten-Oxygen System," Battelle Memorial Institute, January 1966, (BMI-1755).

(12) Dallavalle, J. M., Micromeritics, Pitman Publishing Corp., New York, New York, 1943.

(13) Gray, W. A., The Packing of Solid Particles, Chapman and Hall, Ltd., London, United Kingdom, 1968.

(14) Ayer, J. E., and Soppet, F. E., "Vibratory Compaction: I. Compaction of Spherical Shapes," J. Am. Cer. Soc. 48, 180-183, 1965.

(15) Hein, R. A., Feith, A. D., and Flagella, P. N., "Linear Thermal Expansion Measurement for W-53 UO_2 (Vol. %) Cermet from 800 to 1750°C," General Electric Company, March 1969, (TM 69-4-2).

(16) Lundin, S. T., Studies on Triaxial Whiteware Bodies, Almquist and Wiksell, Stockholm, Sweden, 1959.

(17) Warshaw, S. I., and Seider, R., "Comparison of Strength of Triaxial Porcelains Containing Alumina and Silica," J. Am. Cer. Society, 50, 337-343, 1967.

(18) Kerner, E. H., "Elastic and Thermoelastic Properties of Composite Media," Proc. Phys. Soc. (London), B69, 808-813, 1956.

(19) Marlowe, M. O., and Kaznoff, A. I., "Elastic Behavior of Uranium Dioxide in Ceramic Nuclear Fuels," Proceedings of the International Symposium of American Ceramic Socity, Washington, D. C., May 3-8, 1969.

(20) Marlowe, M. O., "High Temperature Isothermal Elastic Moduli of UO_2," J. Nucl. Mat'ls., 33, 242-244, 1969.

(21) Brown, H. L., and Armstrong, P. E., "Young's Modulus Measurements Above 2000°C," Rev. Sci. Inst. 34, 636-639, 1963.

(22) Filipczynski, L., Pawlowski, Z., and Wehr, J., Ultrasonic Methods of Testing Materials, Butterworths, London, 1966.

(23) Wachtman, J. B. Jr., "Elastic Deformation of Ceramics and Other Refractory Materials," in Mechanical and Thermal Properties of Ceramics, Proceedings of a Symposium, Proceedings of a Symposium, April 1-2, 1968, Gaithersburg, Maryland, National Bureau of Standards Special Publication 303, 1969.

(24) Orr, C. J., Particulate Technology, Macmillan Company, New York, 1966.

DISTRIBUTION LIST

National Aeronautics and Space Administration
Manned Spacecraft Center
Houston, Texas 77058
Attention: B.J. Bragg

National Aeronautics and Space Administration
400 Maryland, S.W.
Washington, D.C. 20546
Attention: James J. Lynch, Code RNP
Fred Schulman, Code RNP

National Aeronautics and Space Administration
Lewis Research Center
21000 Brookpark Road
Cleveland, Ohio 44135
Attention: Roger Mather, MS 302–1
Report Control, MS 5–5
Technology Utilization Office, MS 3–19
T.A. Moss, MS 500–201
Library, MS 3–7
Neal Saunders, MS 105–1
John W.R. Creagh, MS 49–2
Dr. Bernard Lubarsky, MS 3–3
John E. Dilley, MS 500–309
Roland Breitwieser, MS 302–1
Robert Migra, MS 49–2
James Ward, MS 309–1
Ralph Forman, MS 302–1
Vince Hlavin, MS 3–14 (Final Only)

National Aeronautics and Space Administration
Electronics Research Center
Cambridge, Massachusetts 02139
Attention: F.C. Schwarz, Code CP

Battelle Memorial Institute
505 King Avenue
Columbus, Ohio 43201
Attention: Don Kizer
Don Keller

Battelle Memorial Institute
Pacific Northwest Laboratories
1112 Lee Boulevard
P.O. Box 999
Richland, Washington 99352
Attention: Library

The Boeing Company
P.O. Box 3707
Seattle, Washington 98101
Attention: Library

Naval Ship Systems Command
Department of the Navy
Washington, D.C. 20360
Attention: B.B. Rosenbaum, Code 03422
E.P. Lewis, Code 08

McDonnell Douglas Corporation
Missile and Space Engineering
Nuclear Research (A2–260)
3000 Ocean Park Boulevard
Santa Monica, California 90405
Attention: Library

Electro–Optical Systems, Inc.
300 North Halstead Street
Pasadena, California 91107
Attention: A. Jensen

General Electric Company
Missile and Space Division
P.O. Box 8555
Philadelphia, Pennsylvania 19101
Attention: ANSE

General Electric Company
Knolls Atomic Power Laboratory
Schenectady, New York 12300
Attention: R. Ehrlich

North American Rockwell Corporation
S&ID Division
12214 Lakewood Boulevard
Downey, California 90241
Attention: C.L. Gould

Oak Ridge National Laboratory
Oak Ridge, Tennessee 37831
Attention: Library

DISTRIBUTION LIST (Cont'd.)

Office of Naval Research
Power Branch
Department of the Navy
Washington, D.C. 20325
Attention: Cmdr. Ollie J. Loper

Energy Reserach Corp.
15 Durant Avenue
Bethel, Connecticut 06801
Attention: Security Officer

United Aircraft Corporation
Pratt & Whitney Aircraft Division
East Hartford, Connecticut 06108
Attention: Library

Radiation Effects Information Center
Battelle Memorial Institute
505 King Avenue
Columbus, Ohio 43201
Attention: R.E. Bowman

Radio Corporation of America
New Holland Avenue
P.O. Box 1140
Lancaster, Pennsylvania 17601
Attention: Fred Block

Radio Corporation of America
David Sarnoff Research Center
Princeton, New Jersye 08640
Attention: Paul Rappaport

The Rand Corporation
1700 Main Street
Santa Monica, California 90401
Attention: Ben Pinkel

Fairchild–Hiller
Republic Aviation Division
Farmingdale, L.I., New York 11735
Attention: Alfred Schock
B. Wolk

General Electric Company
Electronic Components Division
One River Road
Schenectady, New York 12306
Attention: Dr. D.A. Wilbur,
Manager–Tube Research

General Electric Company
Nuclear Systems Programs
P.O. Box 132
Evendale, Ohio 45215
Attention: J.A. McGurty

General Electric Company
Research Laboratory
Schenectady, New York 12300
Attention: Volney C. Wilson

Aerojet General Nucleonics
San Ramon, California 94583
Attention: Library

Aerospace Corporation
P.O. Box 95085
Los Angeles, California 90045
Attention: Library

Air Force Weapons Laboratory
Kirtland Air Force Base
New Mexico 87117
Attention: Library

Flight Vehicle Power Branch
Air Force Propulsion Laboratory
Wright–Patterson AFB, Ohio 45433
Attention: A.E. Wallis

Space Systems Division (SSTRE)
AF Unit Post Office
Los Angeles, California 90045
Attention: Major W. Iller

North American Rockwell Corporation
Atomics International Division
P.O. Box 309
Canoga Park, California 91305
Attention: Robert C. Allen
Charles E. Smith

DISTRIBUTION LIST (Cont'd.)

Babcock & Wilcox Company
1201 Kemper Street
Lynchburg, Virginia 24501
Attention: Library

General Motors Corporation
Research Laboratories
12 Mile and Mound Roads
Warren, Michigan 48092
Attention: F.E. Jamerson

Institute for Defense Analysis
400 Army Navy Drive
Arlington, Virginia 48092
Attention: R.C. Hamilton

Jet Propulsion Laboratory
California Institute of Technology
4800 Oak Grove Drive
Pasadena, California 91103
Attention: Peter Rouklove
Jerry Davis

Los Alamos Scientific Laboratory
P.O. Box 1663
Los Alamos, New Mexico 87544
Attention: G.M. Grover
E. Salmi

Marquardt Corporation
Astro Division
16555 Saticoy Street
Van Nuys, California 91406
Attention: A.N. Thomas

Lockheed Missile and Space Division
Lockheed Aircraft Corporation
Sunnyvale, California 94086
Attention: H.H. Greenfield

TRW Inc.
TRW Systems Group
One Space Park
Redondo Beach, California 90278
Attention: Library

U.S. Army Erdl
For Monmouth, New Jersey 07703
Attention: Emil Kittl

U.S. Atomic Energy Commission
Germantown, Maryland 20767
Attention: Donald Beard
Patrick O'Riordan

U.S. Atomic Energy Commission
Technical Reports Library
Washington, D.C. 20525
Attention: J.M. O'Leary (3 copies)

Gulf General Atomic, Inc.
P.O. Box 608
San Diego, California 92112
Attention: L. Perry
L. Yang
J.W. Holland

National Aeronautics and Space Administration
Marshall Space Flight Center
Huntsville, Alabama 35812
Attention: Library

National Aeronautics and Space Administration
Scientific and Technical Information Facility
P.O. Box 33
College Park, Maryland 20740
Attention: NASA Representative (2 + repro.)

Air Force Cambridge Research Laboratories
L.G. Hanscom Field
Bedford, Massachusetts 01731
Attention: CRZAP

U.S. Atomic Energy Commission
Division of Technical Information Extension
P.O. Box 62
Oak Ridge, Tennessee 37831 (3 copies)

Varian Associates
611 Hansen Way
Palo Alto, California 94304
Attention: Ira Weismann

DISTRIBUTION LIST (Cont'd.)

Westinghouse Electric Corporation
Astronuclear Laboratory
P.O. Box 10864
Pittsburgh, Pennsylvania 15236

Thermo Electron Corporation
85 First Avenue
Waltham, Massachusetts 02154
Attention: George Hatsopoulous
Robert Howard

National Aeronautics and Space Administration
Ames Research Center
Moffett Field, California 94035
Attention: Library

National Aeronautics and Space Administration
Goddard Space Flight Center
Greenbelt, Maryland 20771
Attention: Library
Joseph Epstein

National Aeronautics and Space Administration
Langley Research Center
Langley Field, Virginia 23365
Attention: Library